Chapter 6: Steady state operation

2007 Nucl. Fusion 47 S285

(http://iopscience.iop.org/0029-5515/47/6/S06)

Nucl. Fusion **47** (2007) S285–S336 doi:10.1088/0029-5515/47/6/S06

Chapter 6: Steady state operation

C. Gormezano[1], A.C.C. Sips[2,a], T.C. Luce[3], S. Ide[4], A. Becoulet[5], X. Litaudon[5], A. Isayama[4], J. Hobirk[2], M.R. Wade[3], T. Oikawa[4], R. Prater[3], A. Zvonkov[6], B. Lloyd[7], T. Suzuki[4], E. Barbato[1], P. Bonoli[8], C.K. Phillips[9], V. Vdovin[6], E. Joffrin[7], T. Casper[10], J. Ferron[3], D. Mazon[5], D. Moreau[5], R. Bundy[9], C. Kessel[9], A. Fukuyama[11], N. Hayashi[4], F. Imbeaux[5], M. Murakami[12], A.R. Polevoi[13] and H.E. St John[3]

[1] ENEA Frascati Energy Research Centre, Frascati, Italy
[2] Max-Planck-Institut für Plasmaphysik, Boltzmannstrasse 2, D-85748, Garching, Germany
[3] General Atomics, San Diego, USA
[4] Japan Atomic Energy Agency, 801-1 Mukouyama, Naka-shi, Ibaraki-ken, 311-0193, Japan
[5] Association EURATOM-CEA Cadarache, St Paul lez Durance, France
[6] Nuclear Fusion Institute, RRC 'Kurchatov Institute', 123128 Moscow, Russia
[7] UKAEA-EURATOM Association, Culham Science Centre, Abingdon, OX14 3DB, UK
[8] Plasma Science and Fusion Center, MIT, Cambridge, MA 02139, USA
[9] Plasma Physics Laboratory, Princeton University, Princeton, USA
[10] Lawrence Livermore National Laboratory, Livermore, California, USA
[11] Kyoto University, Kyoto 606-8317, Japan
[12] Oak Ridge National Laboratory, Oak Ridge, Tennessee, 37831, USA
[13] IT, ITER Naka JWS, Naka, Japan

E-mail: ccs@ipp.mpg.de

Received 24 February 2006, accepted for publication 24 January 2007
Published 1 June 2007
Online at stacks.iop.org/NF/47/S285

Abstract
Significant progress has been made in the area of advanced modes of operation that are candidates for achieving steady state conditions in a fusion reactor. The corresponding parameters, domain of operation, scenarios and integration issues of advanced scenarios are discussed in this chapter. A review of the presently developed scenarios, including discussions on operational space, is given. Significant progress has been made in the domain of heating and current drive in recent years, especially in the domain of off-axis current drive, which is essential for the achievement of the required current profile. The actuators for heating and current drive that are necessary to produce and control the advanced tokamak discharges are discussed, including modelling and predictions for ITER. The specific control issues for steady state operation are discussed, including the already existing experimental results as well as the various strategies and needs ($q\psi$ profile control and temperature gradients). Achievable parameters for the ITER steady state and hybrid scenarios with foreseen heating and current drive systems are discussed using modelling including actuators, allowing an assessment of achievable current profiles. Finally, a summary is given in the last section including outstanding issues and recommendations for further research and development.

PACS numbers: 28.52.−s, 52.50.Gj, 52.50.Sw, 52.65.−y

(Some figures in this article are in colour only in the electronic version)

Contents

[a] Author to whom any correspondence should be addressed.

1. Introduction

It has always been an important goal of ITER to demonstrate reactor scale steady state operation for the tokamak. Provisions have been made to have sufficient flexibility in terms of control and of additional heating and current drive systems to investigate such operational regimes [1]. At the time when the ITER Physics Basis (IPB) was written, plasmas with improved confinement were achieved in various modes, i.e. ELM-free H-mode and plasmas with internal transport barriers (ITBs), but mainly in a transient way. The first indications of scenarios with some prospects for long pulse operation and possibly steady state operation were high β_P plasmas in JT-60U [2], optimized shear plasmas with double barrier in JET [3] and further developments in JT-60U, summarized in [4]. However, a proper experimental support for steady state operation was far from available in the same way as for the reference H-mode.

The parameters needed for steady state operation were already rather well established: lower current operation to minimize the need for non-inductive drive, high confinement to maximize the fusion production and high beta operation to maximize the bootstrap current fraction [5]. Accordingly, target parameters for steady state operation were selected in the IPB: assuming a current density profile with reversed magnetic shear, operating at a plasma current $I_p = 12\,\mathrm{MA}$, a bootstrap current fraction, $f_{BS} \cong 0.8$, normalized beta $\beta_N = 3.8$ ($\beta_N = \langle\beta\rangle a B_T / I_p$, with $\langle\beta\rangle$, the volume averaged normalized pressure (p) in the tokamak, a is the plasma minor radius, B_T the toroidal field), poloidal beta $\beta_P = 2.3$, $T_{e_0} = 26\,\mathrm{keV}$, $n_e/n_G = 1.4$ ($n_G = 10^{20} I_p\,[\mathrm{MA}]/\pi a\,[\mathrm{m}]^2$ [6]), a fusion

gain $Q = 15$ could be achieved. It was recognized that such plasmas would require a nearby conductive wall to attain MHD stability at high beta, therefore requiring specific control to be developed for ITER steady state operation. Subsequently, the goals have been revised for ITER-FEAT, taking into account the smaller size of the machine and the already achieved experimental results in the domain. The magnetic shear of the proposed scenario is less reversed with $q(0)$ just above 2 and $q_{\min}$ between 1.5 and 2, the plasma current is down to 9 MA and the steady state Q is set at 5.

In effect, since the publication of the IPB, advanced scenarios have been extensively studied in all tokamaks with or without divertors. Substantial progress has been made so that some schemes are considered potential candidates for a steady state scenario on ITER, while other schemes still need some more developments. One of the main parameters in the present development of advanced scenarios is the plasma current profile. Most of the experimental scenarios use a substantial amount of heating and/or current drive in the current ramp-up phase, when the beta of the plasma is still low, in order to freeze the current profile. A very large variety of current profiles, from deep reversed shear to low positive shear, have been generated and sustained using either these operational tools or some MHD effects such as fishbones.

In configurations with strong shear reversal, long, steady high performance discharges with almost no current at the centre (JT-60U [7]) have been achieved. However, problems are likely to appear for steady state operation (low beta limits due to the high value of $q_{\min}$ and impurity accumulation due to the density peaking), the main problem being linked to the low confinement of alphas and other energetic particles, leading to power deposition outside the ITB, as well as an increased diffusion due to collective modes if $q(0) > 3$. So far the best use of such configurations is foreseen for scenario development, in particular, to make use of the low power required to produce an ITB when the magnetic shear is strongly reversed.

Quasi-steady state plasmas have been achieved in several experiments with weak shear reversal and $q_{\min}$ around 2, showing some of the features required for steady state operation: a high bootstrap fraction, high beta limits and densities at a substantial level of the Greenwald limit. In JET, a full non-inductive current drive discharge has been achieved at 2 MA/3.4 T for 7 s, about $23\tau_E$, $I_{\mathrm{BS}} = 1$ MA, $f_{\mathrm{BS}} = 0.5$ [8, 9], but with the current density profile still showing some evolution as the non-inductive current profiles are not aligned to the initial (starting) current density profile. For these discharges in JET, the volume-averaged resistive diffusion time, $\tau_{\mathrm{R}} = \langle \mu_0 \sigma(\rho) \rho^2 \rangle$, evaluated with the neoclassical conductivity profile $\sigma(\rho)$, is about 12 s. The pulse duration including the LHCD preheating phase is 11 s. In JT-60U, full current drive discharges have been achieved at 1.8 MA/4.1 T, $q_{95} = 4.1$ ($6\,\tau_E$) with $H_{98}(y, 2) = 1.2$, $\beta_{\mathrm{N}} = 2.4$, $\beta_{\mathrm{P}} = 1.7$ and $f_{\mathrm{BS}} = 0.5$ [10]. For the definition of $H_{98}(y, 2)$ or H_{89} see [1] and references therein. The use of negative neutral beam injection (N-NBI) should be noted. In DIII-D up to 98% non-inductive current fraction with off-axis ECCD was maintained for $7\,\tau_E$ at the no-wall beta limit with $\beta_{\mathrm{N}} = 3$, $\beta = 3.3\%$ and $H_{89} = 2.4$ [11]. In these discharges the bootstrap current fraction is 59%, the neutral beam driven current 31% and the current driven by ECCD 8% of the total current. Moreover, the q-profiles in these discharges are compatible with good alpha confinement and mild collective modes.

One of the interesting developments of the recent years is the achievement of stationary H-modes with zero magnetic shear and $q(0)$ around 1. In ASDEX Upgrade [12], plasmas with $\beta_{\mathrm{N}} = 3.6$, $H_{98}(y, 2) = 1.3$, $n_{\mathrm{e}}/n_{\mathrm{G}} \cong 0.85$ and $f_{\mathrm{BS}} \cong 0.4$ have been achieved at $q_{95} = 3.6$, with the current profiles clamped by fishbones. In DIII-D [13], similar steady pulses ($35\,\tau_E$, more than three times the current relaxation time) were achieved with $q(0) = 1.04$ at $q_{95} = 4.3$. Current clamping is attributed to the presence of a mild 3/2 tearing mode. Similar discharges have also been achieved in JET [14].

For ITER, the advanced scenarios proposed have been defined through their respective objectives. The steady state scenario aims at producing discharges where the current is driven fully non-inductively with $Q = 5$ at $I_{\mathrm{p}} = 9$ MA ($q_{95} \sim 5$). Candidates for this type of operation in ITER are the discharges from present-day experiments with a moderately reversed q-profile, given above. A hybrid scenario in which the plasma current is driven by a combination of inductive and non-inductive currents is intended to provide operation with a long burn time (>1000 s), high fluence/shot and $Q > 5$ with a high reliability for engineering tests. To achieve this goal, the plasma current in this scenario is lower (12–14 MA) than the reference H-mode scenario but higher than steady state scenarios. Only a moderate assumption on confinement and beta ($H_{98}(y, 2) = 1$ and $\beta_{\mathrm{N}} \sim 2$) is required. An advanced hybrid scenario is a hybrid scenario, aiming at producing high fusion yield and features a higher beta limit with an optimized current profile, a lower current and a lower loop voltage, which would allow operating with a high fusion gain ($Q \sim 10$) for long pulse duration. Examples for this type of operation from ASDEX Upgrade [12] and DIII-D [13] using zero magnetic shear in the centre achieving β_{N} near 3 were given. The advanced hybrid scenarios are often simply called hybrid scenarios.

However, it should be noted that these presently developed advanced scenarios have not yet provided fully integrated scenarios and several issues remain to be solved, such as edge compatibility with the divertor, fuelling and impurity accumulation. Nevertheless, they do constitute a very good basis for further development and progress is steady.

The corresponding parameters, domain of operation, scenarios and integration issues of advanced scenarios are discussed in section 2. A review of the presently developed scenarios, including discussions on operational space, is given in section 3. Significant progress has been made in the domain of heating and current drive in recent years, especially in the domain of off-axis current drive, which is essential for the achievement of the required current profile. The actuators for heating and current drive that are necessary to produce and control the advanced tokamak discharges are discussed in section 4, including modelling and predictions for ITER. The specific control issues for steady state operation are discussed in section 5, including the already existing experimental results as well as the various strategies and needs (q-profile control and temperature gradients). Achievable parameters for the ITER steady state and hybrid scenarios with foreseen heating and current drive systems are discussed in section 6 using

modelling including actuators, allowing an assessment of achievable current profiles. Finally, a summary (section 7) is given in the last section including outstanding issues and recommendations for further research and development.

2. Integrated scenarios

As discussed in the introduction, advanced tokamak scenarios have two key roles in burning plasma devices. The first role is to access true steady state operation. Steady state operation requires profiles stationary on the current evolution time scale with no inductive flux (on average) to sustain the plasma. The ultimate goal of steady state operation is energy production, so high fusion gain of the core is essential. The constraints on high gain fusion discharges implicit in the physics of fully non-inductive discharges are discussed in section 2.2. The second role of advanced tokamak scenarios is to deliver the maximum neutron fluence. Due to limitation in the cooling system in ITER, this may also be obtained using pulsed discharges (not steady state) that have a high reliability. Since the same non-inductive current sources required for true steady state operation could be applied to the extension of the duration of inductive discharges, the term 'hybrid' operation has been coined to describe this type of operation. High fusion gain is not an absolute requirement, but is highly desirable, both to reduce operating costs and to provide a benchmark for the potential of the pulsed tokamak for energy production. The trade-offs for hybrid operation are discussed in section 2.3, with particular attention to the ITER design.

2.1. Figures of merit for evaluating advanced scenarios

Comparison of steady state, hybrid and conventional discharges in a burning plasma device is straightforward. The fusion power, energy production and gain can be compared by direct measurement. The principal challenge now is to find the means to compare discharges in present-day machines and to estimate how well those discharges will perform in burning plasma devices.

For steady state operation, the two key elements are non-inductive operation and high fusion gain. The evaluation of the inductive flux consumption seems rather obvious. When the current profile has stopped evolving, the poloidal flux enclosed by the smallest major radius of the plasma must not be changing. However, the position control of the plasma by feedback and repetitive instabilities of the plasma such as sawteeth and ELMs (see chapter 3 of this issue [15]) make this ideal non-inductive situation unrealistic. The poloidal flux in the central region will undoubtedly change, but the requirement is that there be no long time average change in flux. The appropriate time scale for this average is the resistive relaxation time scale for the plasma current density profile at constant current $\tau_{R,I}$ (if the central solenoid is used) or at constant voltage $\tau_{R,V}$ (if there is no solenoid or the central solenoid current is clamped to a fixed value). This time scale is obtained from solutions to the combination of Faraday's law, Ampere's law and Ohm's law [16]. The characteristic times are given by $\tau_{R,j} = \tau_0/k_j^2$, where $j = I, V$ for constant current or voltage, respectively, and $k_I = 3.8317$ and $k_V = 2.4048$ in the circular cylinder approximation. The parameter τ_0 is given by $2.51\,R/\Re$, where R is the major radius in m and $\Re$ is the plasma resistance in $\mu\Omega$.

A secondary figure of merit for non-inductive operation is the fraction of the plasma current I_p generated by the bootstrap current ($f_{BS} = I_{BS}/I_p$). The bootstrap current arises from finite excursions of the particles from the flux surfaces in the presence of density and temperature gradients (see chapter 2 of this issue [17]). The bootstrap current comes at no additional cost in power to the auxiliary heating systems required to maintain the desired fusion performance. Therefore, f_{BS} gives a qualitative indication of the ease with which a given plasma can be maintained in steady state.

Projecting present-day discharges to burning plasmas is a difficult task (see chapter 2 of this issue [17] for confinement projections). The approach taken here for evaluation of advanced scenarios is to derive a dimensionless ratio of global quantities which is related to fusion gain. This dimensionless parameter captures the scalings of the most significant limits for tokamak operation. Comparing scenarios in present-day devices gives some indication of the relative values of fusion gain, if these scenarios were performed on a single tokamak. Given a burning plasma design such as ITER, a benchmark value of the dimensionless parameter can be derived to give an indication of the absolute value of gain expected for a present-day scenario in that design. To begin, the fusion gain can be shown to have the following relation with the fusion triple product [18]:

$$nT\tau \propto Q/(Q+5), \tag{1}$$

where the electron and ion temperatures are assumed to be equal and the plasma is assumed to be a pure 50–50 mixture of deuterium and tritium. Corrections can be made for these assumptions, but they do not affect the leading-order term of the dimensionless parameter. The triple product can be recast in terms of the pressure limit scaling and the confinement scaling as follows:

$$nT\tau \propto (\beta B^2)(H\tau_{scale}) = (\beta_N I B/a)(H\tau_{scale}). \tag{2}$$

For all confinement scalings in routine use, τ_{scale} is nearly proportional to I. There is a limit to increasing current which is related to the safety factor $q_{95} \propto a^2 B/RI$; the practical limit on reliable operation lies in the range $q_{95} = 2.5$–3.0, depending on the plasma shape and the details of the discharge history. Replacing current with the safety factor q_{95}, the triple product then becomes

$$nT\tau \propto \beta_N H/q_{95}^2 f(a, B, P_{fus}, \ldots). \tag{3}$$

This dimensionless parameter $\beta_N H/q_{95}^2$ contains the key physics scalings that will affect the fusion gain within a given machine: the pressure limit, the confinement scaling and the limit to increasing plasma current. The dimensionless parameter is used with different confinement scaling multipliers: $H_{98}(y, 2)$ or more typically H_{89} [1].

2.2. Physics issues for steady state operation

Operation of a tokamak in steady state requires that the poloidal flux and the pressure gradients be maintained against losses without the use of induction. To be an energy producing facility, these constraints must be satisfied at high fusion gain. Examination of the global scalings for a device of fixed size and geometry illustrates the direction in which the steady state

requirement pushes tokamak operation [18]. First, the global current balance can be written as

$$f_{\rm ind} = (1 - f_{\rm BS} - f_{\rm CD})I = 0, \tag{4}$$

where the last equality holds in steady state. The bootstrap current fraction is given by

$$f_{\rm BS} \propto \beta_{\rm p} \propto \beta_{\rm N} B/I \equiv C_{\rm BS}\beta_{\rm N} q_{95}. \tag{5}$$

The auxiliary current drive fraction is determined by evaluating the dimensionless efficiency:

$$\zeta \propto n I_{\rm CD}/P_{\rm CD}T. \tag{6}$$

The efficiency used here is most applicable to current drive schemes where the velocity of the current carriers scales with the thermal velocity. The fraction of current driven directly by non-inductive means is then

$$f_{\rm CD} \propto I_{\rm CD}/I \propto \zeta P_{\rm CD}T/nI \propto \zeta P_{\rm CD}\beta B^2/n^2 I \equiv C_{\rm CD} P_{\rm CD}\beta_{\rm N} B/n^2. \tag{7}$$

The current balance equation implies

$$1 - C_{\rm BS}\beta_{\rm N} q_{95} - C_{\rm CD} P_{\rm CD}\beta_{\rm N} B/n^2 = 0. \tag{8}$$

Turning now to the fusion gain, the fusion power can be estimated as

$$P_{\rm fus} \propto p^2 \propto \beta^2 B^4 \propto \beta_{\rm N}^2 I^2 B^2. \tag{9}$$

If there is no additional auxiliary power beyond that required to drive the non-inductive current, the fusion gain is

$$Q \equiv P_{\rm fus}/P_{\rm CD} \propto \beta_{\rm N}^2 I^2 B^2 (1/(1 - C_{\rm BS}\beta_{\rm N} q_{95}))C_{\rm CD}\beta_{\rm N} B/n^2 \propto C_{\rm CD}\beta_{\rm N}^3 I^2 B^3/n^2(1 - C_{\rm BS}\beta_{\rm N} q_{95}). \tag{10}$$

Now note that the density can be recast as a fraction of the Greenwald density limit $f_{\rm G} = n_{\rm e}/n_{\rm G}$ (see chapter 2 of this issue [17]). Then the fusion gain becomes

$$Q \propto C_{\rm CD}\beta_{\rm N}^3 B^3/f_{\rm G}^2(1 - C_{\rm BS}\beta_{\rm N} q_{95}). \tag{11}$$

This implies that the fusion gain of a steady state burning plasma maximizes at the highest field the machine can run and at the minimum allowable density possible near the pressure limit. The quantity in the denominator is just $1 - f_{\rm BS}$, which is positive in all present discharges. Quantitative evaluation of this formula for typical burning plasma parameters indicates $C_{\rm CD}$ and the constant of proportionality are too small to get high fusion gain, unless $1 - f_{\rm BS}$ is quite small. Again, to make this factor small, it is important to maximize β, but also advantageous to increase q_{95}.

It is somewhat surprising that the confinement quality factor H does not appear in the formula for fusion gain in steady state (equation (11)). The absence of H can be understood by comparison of the power required to maintain constant pressure against radial transport losses with the minimum total power to maintain both the pressure against transport losses and the plasma current against collisional losses. The power required to maintain the pressure in equilibrium against transport losses is given by

$$P_{\rm L} \equiv W/\tau \propto \beta B^2/HIf_{\rm scale} \propto \beta_{\rm N} B/H. \tag{12}$$

In the case of inductive scenarios, the power required to maintain the parallel current by induction is usually negligible compared with the power needed to balance radial transport losses, so the total power balance and the power required to maintain the pressure are in that case equivalent. In the case of steady state operation (without induction), the minimum power required to maintain both the pressure and current in equilibrium is determined by the point where the sum of the α-heating power and the current drive power is equal to the transport loss power (as assumed in writing equation (10)). Combining equations (8), (9) and (12) this implies

$$P_{\rm L} \equiv P_\alpha + P_{\rm CD} = C_{\rm fus}\beta_{\rm N}^2 I^2 B^2 + (1 - C_{\rm BS}\beta_{\rm N} q_{95})n^2/C_{\rm CD}\beta_{\rm N} B \propto \beta_{\rm N} B/H. \tag{13}$$

This indicates that the current and pressure equilibrium can only be satisfied simultaneously by a specific value of H in the optimal case where the minimum auxiliary power is applied. If the confinement quality factor is larger than this value of H, then there is no steady state solution at the chosen operating conditions—either the current will decay or the stored energy will increase. If H is smaller than this optimal value, then $P_{\rm CD}$ can be replaced in equation (10) by $P_{\rm CD} + P_{\rm aux}$. This reduces the fusion gain as expected. It is unlikely that a fusion device can be operated exactly at the optimal point, but the scaling derived at this point indicates how the plasma and tokamak parameters can be optimized for high gain steady state operation.

The main conclusion from this exercise is that the key plasma physics quantity to maximize for high gain steady state fusion energy production is β. Maximizing the confinement quality may lead to a situation where no steady state solution is possible. The only exception to this rule is the unlikely where $f_{\rm BS} = 1$, which would leave only the pressure balance to be satisfied. On the other hand, the reduction of confinement with increasing q_{95} is what limits the fusion gain when q_{95} is increased to more easily satisfy the current balance.

Since the β limit plays such a key role in steady state operation, a brief summary of the β limit physics of these advanced scenarios can be found in chapter 3 [15] of this special issue and results from present-day experiments are found in section 3.

The most promising results that point towards steady state operation in present-day machines have been obtained using flat or slightly reversed q-profiles with elevated $q_{\rm min}$ [13, 19]. The highest performing discharges have $\beta > \beta_{\text{no-wall}}$, the value at which the $n = 1$ mode would be unstable in the absence of a conducting wall and rely on rotation to stabilize the resistive wall mode (RWM) [20]. A more detailed description of the mode and stabilization criteria can be found in chapter 3 of this issue [15]. Values of normalized β up to twice the baseline scenario value have been sustained for about a resistive relaxation time [13]. Details of these results are presented in section 3. Since the fusion gain maximizes at high $\beta_{\rm N}$, operation in proximity to the β limit is desirable. The ability to control the plasma reliable near the β limit is essential to these scenarios. An extensive discussion of control will be given in section 5. The amount of installed power in excess of that needed to supply the equilibrium current profile is correlated with the proximity to β limits that can be run safely.

There are indications from present-day experiments that operation in steady state at constant voltage will be quite difficult. Experiments on the DIII-D tokamak indicate that the fixed points of the fluid equations may not be stable to perturbations [21]. One example of this is the formation and collapse of internal transport barriers (ITBs), which may affect the current balance strongly. Operation at constant current rather than constant voltage appears to dampen these effects. This implies that to maintain fully non-inductive operation on the long time scale, the capability of overdriving the plasma current non-inductively is required. This is discussed more extensively in section 3.

The shape of the q-profile also strongly influences the stability of the plasma of the modes driven by energetic particles such as α particles from the fusion reactions or fast ions from neutral beam injection or ion cyclotron resonance heating. The value of q and the shape of the profile determine the radial mode structure of Alfvén eigenmodes and coupling to damping mechanisms. The stability of burning plasmas of these modes cannot be simulated directly in present-day experiments. Instead, numerical models that are validated, where possible, in present-day experiments, evaluate designs. A detailed discussion of this is given in chapter 5 of this issue [22].

The fusion gain in steady state (equation (11)) also maximizes at low density for constant β_N. The limitation on reducing the density in next-generation tokamaks is set by the impact on the divertor. The present solution for handling the heat load on the divertor in ITER is to radiate a significant amount of power in the plasma edge and divertor to minimize the power flow directly to the divertor tiles. In addition, detachment of the plasma from the divertor plates is envisioned. Both these effects require high density at the plasma edge. The present scaling of the upper limit in density for stable operation is proportional to I_p, which is opposite to the direction that the current should change to maximize the bootstrap current. The increase in q_{95} may offset some of the problems at low density, due to the increase in the length of the scrape-off layer along the field line. The impact of ELMs is also uncertain, both on the divertor and the scenario. The pedestal height may be smaller at higher q_{95}, which would likely be favourable to the divertor, but may adversely impact the confinement (see chapter 2 of this issue [17]). Clearly, safe divertor operation sets a fundamental limit on the minimum density for steady state operation. Unfortunately, these two physics elements cannot be simultaneously tested in present-day tokamaks. An additional consideration is that the divertor, the scrape-off layer and the edge plasma must still effectively shield the core plasma from impurities. These steady state scenarios have confinement at least as good as the conventional scenario; therefore, impurity accumulation is a concern.

One final operational boundary needs to be discussed in the context of steady state operation. All high fusion gain scenarios require H-mode levels of confinement. This means the loss power must be significantly in excess of the L–H transition power at the parameters of the operating point. For present-day tokamaks, this is not a very stringent constraint, but the size and toroidal field scaling of the transition power cause it to increase faster than the loss power with increasing device size and magnetic field strength. In addition, present-day machines use the L–H transition timing as part of the scheme to generate the appropriate current and pressure profiles. This capability may be needed in the formation phase of these burning plasma scenarios.

Finally, the large conductivity of burning plasma requires that some care be taken in the formation of the desired current profile in the current ramp-up phase. Instability thresholds discussed above may be encountered in experiment; therefore, special attention should be paid to determine the operational space of advanced scenarios. This emphasizes the important role played by realistic simulations of the plasma and the control system in designing the scenarios. Progress in this area is detailed in section 6.

2.3. *Physics issues for hybrid operation*

As discussed in section 1, the goal of hybrid operation is to maximize the neutron fluence in each pulse in order to facilitate a limited mission of nuclear testing in ITER. Obviously, a true steady state scenario as discussed in the previous section would maximize the fluence since the pulse could be arbitrarily long. In the absence of such a scenario, however, it is of interest to see how the inductive performance to achieve maximum fluence per pulse is optimized. The fluence can be characterized as the fusion energy released in a pulse. This is given simply by

$$W_{fus} = P_{fus} t_{dur}. \tag{14}$$

The fusion power, as discussed above, can be approximated using the volume-averaged pressure p:

$$P_{fus} \propto p^2 V \propto \beta^2 B^4 a^3. \tag{15}$$

The inductive duration t_{dur} is more difficult to characterize. Taking the total flux capability of the central solenoid to be ψ_{CS} and the flux used to reach the current flattop as ψ_I, then the duration is given by

$$t_{dur} = (\psi_{CS} - \psi_I)/(\partial\psi/\partial t) = (\psi_{CS} - \psi_I)/\mathrm{I}_{ind}\Re, \tag{16}$$

where the inductive voltage has been replaced by $I_{ind}\Re$ for stationary discharges, taking the plasma resistance as $\Re$. The plasma resistance is inversely proportional to $T^{3/2}$, and the inductive current can be written as the total current less the bootstrap and driven currents (equation (4)). Combining these, the duration becomes

$$t_{dur} = (\psi_{CS} - \psi_I)(\beta B^2/n)^{3/2}/I(1 - f_{BS} - f_{CD}), \tag{17}$$

where the temperature has been replaced by (p/n). The fluence then becomes

$$\begin{aligned} W_{fus} &\propto \beta^2 B^4 a^3 (\psi_{CS} - \psi_I)(\beta B^2/n)^{3/2}/I(1 - f_{BS} - f_{CD}) \\ &\propto (\beta_N^7 B^7 a^5/f_G^3)^{1/2} I(\psi_{CS} - \psi_I)/(1 - f_{BS} - f_{CD}). \end{aligned} \tag{18}$$

This relation implies that fluence is maximized by operation with β as high as possible, while minimizing the density at that β. This conclusion follows directly from the factor in front, but the same considerations also minimize the inductive current fraction in the denominator. It might appear that the fluence is maximized at high current, but the flux consumed in the current build-up (ψ_I) is also proportional to I. Projections based on DIII-D discharges (discussed in

section 4) indicate that the fluence per pulse is significantly larger for $q_{95} \sim 4$ discharges than for those with $q_{95} \sim 3$, because ψ_I is smaller, β_N is larger and the inductive current fraction is smaller. Note that confinement does not enter the equation unless the achievable β is limited by the confinement instead of a stability limit. The projections from the DIII-D discharges indicate that the ITER scenarios are not limited by the available power except in the case of L-mode scaling. The fluence is also maximized at the highest possible value of B.

As mentioned above, the β_N obtained has a strong influence on the fluence. For the reference baseline scenario (see chapter 3 of this issue [15]), β_N is limited to ~2 in order to avoid confinement degradation due to tearing modes. Discharges in ASDEX Upgrade [23], DIII-D [24], JET [25] and JT-60U [26] have obtained stationary ELMy H-mode discharges with β_N well in excess of 2. The key element of these discharges (discussed more fully in section 3.4) seems to be the access to a current profile that is stable to $n = 1$ tearing modes at high β_N by a careful control of the pressure and the current in the current build-up phase. The limiting β_N depends on whether sawteeth are present in the stationary phase. In discharges without sawteeth, operation up to $\beta_{\text{no-wall}}$ is possible. Discharges with sawteeth are stable up to about 85% of this limit. Experiments indicate that the sawteeth can be avoided only when $q_{95} \geqslant 3.8$–4.0 [23, 24]. The fusion gain still maximizes at the lowest q_{95}, even with this variation in the β limit; however, the fluence maximizes at the lowest q_{95} where sawteeth can be avoided.

As in the steady state scenario, the reduction in density presents a concern with respect to divertor operation. The effect of the pedestal height variation with current and density on the divertor and the confinement is uncertain at present, as discussed in the previous section. This is a topic of ongoing research. Impurity accumulation is also a concern. Preliminary measurements in DIII-D of the carbon inventory indicate no preferential accumulation of carbon in the core plasma [27]. This is consistent with the presence of rapid ELMs in the present discharges.

3. Review of presently developed experimental scenarios

3.1. Operational space

The standard ITER scenario with an edge transport barrier (H-mode) has an extensive experimental database and is attractive for reaching high fusion power. However, it does not allow reaching conditions where the plasma current is completely non-inductively driven and a significant Q is achieved. In the past ten years, much effort has been made to develop regimes that could lead to the fully non-inductive operation of a tokamak at high fusion yield, utilizing the self-generated (pressure driven) bootstrap effect. A key to the development of these scenarios is the tailoring and control of the current density profile, with the aim of improving core confinement and stability of the plasma. In the standard inductive operation mode of ITER, the safety factor (q-profile) increases monotonically with radius and q on-axis ($q(0)$) is below unity. The safety factor at the edge (q_{95}) is near 3, determined by safe operation at maximum plasma current. Experimental results obtained on different tokamaks in advanced scenarios with improved confinement and performance can be categorized according to the q-profile used for the regime, for instance as shown in figure 1. It is, of course, possible to imagine a continuum of regimes between the reference non-inductive and inductive scenarios in which the current profile is modified externally but not completely driven by non-inductive means. In the following, the experimental scenarios that are presently developed have been subdivided into three categories:

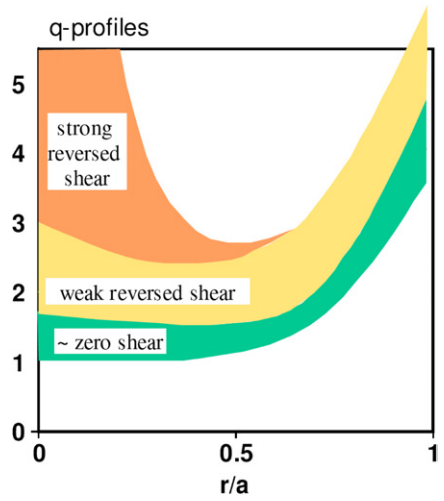

Figure 1. Classification of advanced scenarios according to the q-profile used.

(i) The first one includes scenarios with moderate reversed shear, i.e. with the difference between the minimum of the q-profile ($q_{\min}$) and $q(0)$ of less than ~2. Also included are configurations with a flat current profile and very low shear, with $q(0)$ between 1.5 and 2.5. These discharges typically have internal transport barriers in the core and operate at reduced plasma current with q_{95} near 5, to maximize the bootstrap current fraction at high performance. These types of plasmas are considered to be good candidates for steady state operation in ITER, with $f_{BS} = 0.5$ and the rest of the plasma current driven by external sources. These discharges are reviewed in section 3.2, together with a discussion on some of the issues that still have to be resolved (the control requirements are given in section 5).

(ii) The second category deals with high bootstrap fraction plasmas including strongly reversed shear plasmas (section 3.3). These plasmas provide interesting insights into steady state operation, in particular, for reactor type plasmas where a bootstrap fraction significantly higher than 0.5 will be required. Typically this regime is obtained in discharges with strongly reversed shear, where the current density in the centre is very low and in some cases even zero (discharges with a 'current hole'). However, some important issues such as MHD stability, confinement of fast particles in the core and operation at higher current (lower q_{95}) have to be resolved in order to make these scenarios attractive for steady state operation in ITER.

(iii) The third category refers to advanced scenarios with zero or low magnetic shear in the centre with $q(0)$ near 1. This

represents an intermediate step between monotonic and reversed shear operation and is often called a 'hybrid' scenario. These plasmas typically have no internal transport barriers, operate with $q_{95} \sim 4$ and could be used for long pulse operation at high fusion yield (hybrid operation of ITER). The status and recent progress of the development of this hybrid scenario for ITER are given in section 3.4.

3.2. Steady state experimental scenarios with weak reversed shear or low magnetic shear

In order to satisfy the objectives in ITER of sustaining $Q \geqslant 5$ in steady state operation, several conditions have to be satisfied simultaneously. In particular, a full current drive has to be achieved with the use of external current drive techniques and the 'natural' bootstrap current. Lower hybrid current drive (LHCD), with the highest current drive efficiency, negative-ion based neutral beam injection (N-NBI) and electron cyclotron current drive (ECCD) are used in today's experiments (see section 4). In order to achieve a full non-inductive current drive within an affordable external current drive power, the bootstrap current fraction ($f_{\rm BS}$) should be high enough: $f_{\rm BS} = 0.5$ or higher. Since the bootstrap current is the consequence of local pressure gradients and is proportional to $\beta_{\rm p}$, most experiments tend to operate at low current and with internal transport barriers. The bootstrap current created by the edge pedestal also plays an important role. However, operation at a too high q_{95} (>6) requires too high values of beta and confinement enhancement over the H-mode scaling to achieve significant Q in ITER. Consequently, it is probably not relevant extrapolating these scenarios to ITER. A compromise has to be found between having a large enough poloidal magnetic field in the core region (low $q(0)$), to achieve a sufficient fusion gain ($Q \geqslant 5$), and maximizing the bootstrap current fraction. In addition, the formation of internal transport barriers with too steep pressure gradients has to be avoided to achieve high $\beta_{\rm N}$ and to avoid impurity accumulation. It is estimated that $\beta_{\rm N}$ of around 2.5 or higher would be required to keep $\beta_{\rm p}$ high enough to attain large enough $f_{\rm BS}$ in the expected range of q_{95} ~4–5. A study of these issues in plasmas with full non-inductive current drive is required for assessing the steady state operation in ITER.

The number of experiments that have succeeded in demonstrating steady state, full non-inductive current drive is limited. Not all experiments are equipped with external current drive techniques or not all experimental conditions are well suited to allow enough current drive. Matching the requirements for forming and sustaining ITBs by operating at high enough $\beta_{\rm N}$ gives a rather restricted operational space. Two main approaches follow: (i) the use of a combination of off-axis current drive and moderate reversed shear (RS) configurations and (ii) the so-called high beta poloidal ($\beta_{\rm p}$) mode (JT-60U [4]) with low magnetic shear. RS operation can be beneficial as clear ITBs contribute to improving confinement and to raising $f_{\rm BS}$. However, ITBs can also be triggered near rationale q surfaces in low shear configurations (see chapter 2 of this issue [17]); hence, both configurations are used for operation in steady state conditions.

To obtain fully non-inductive conditions, current drive by means of LHCD has been extensively used, since LHCD has the highest current drive efficiency in the current experiments. In JT-60U, sustainment of ITBs in $n_{\rm e}$, $T_{\rm e}$ and $T_{\rm i}$ profiles with LHCD in full-CD condition was demonstrated. The combination of off-axis LH driven current and bootstrap current ($f_{\rm BS} = 0.23$) sustained the reversed shear configuration in quasi steady state in JT-60U [10]. Also in JET, sustainment of $n_{\rm e}$, $T_{\rm e}$ and $T_{\rm i}$ ITBs in ~90% non-inductive current drive has been obtained under quasi steady state conditions (figure 2) [9] with $\beta_{\rm N} = 1.7$, $H_{98}(y, 2) = 0.95$ ($I_{\rm p} = 2$ MA, $q_{95} = 5.5$). In the discharge the non-inductive current was driven with the bootstrap current ($f_{\rm BS} \sim 0.5$) and externally by LHCD ($f_{\rm LHCD} \sim 0.35$) and NBCD ($f_{\rm NBCD} \sim 0.15$). A small collapse, observed for a short period of time, is attributed to impurity accumulation. However, the reversed shear configuration remains and the performance is restored rapidly as the additional heating is maintained. This indicates that the magnetic configuration is the dominant element allowing performance to be sustained. Such an impurity accumulation was subsequently avoided in discharges with lower ITB pressure gradients. Furthermore, expansion of the ITB radius was demonstrated with LHCD in JT-60U in full-CD condition with $f_{\rm BS} = 0.63$, $\beta_{\rm N} \leqslant 2.2$ and $H_{98}(y, 2) = 1.4$ at $f_{\rm G} = 0.82$ but at higher $q_{95} = 6.9$ [28].

In DIII-D, a series of discharges demonstrated full non-inductive current drive with $f_{\rm BS} \sim 0.5$ [11]. In these discharges, a flat q-profile with $q(0) > 1.5$ was obtained. Central NBCD together with off-axis ECCD and bootstrap current creates such a q-profile. Moderately peaked pressure profiles (weak ITBs) prevent the bootstrap current from peaking off-axis and the magnetic shear from reversing too strongly. In order to sustain the bootstrap current fraction, maintaining a weak ITB while flattening the shear is important. An example is shown in figure 3 from DIII-D [29]. With high NBI power (~16 MW), 100% non-inductive current drive has been achieved for a duration longer than 0.5 s with $\beta_{\rm N} \sim 3.5$ that exceeds the no-wall limit ($4 \times l_{\rm i}$) at $V_{\rm loop} = 0$. It should be noted that the loop voltage profile is not fully relaxed, i.e. the net Ohmic current is zero, but the local Ohmic current is not zero everywhere. In these series of experiments in DIII-D, neoclassical tearing modes with $m/n = 3/2$ do not occur as long as $q_{\rm min}$ is maintained above 1.5. However, $m/n = 5/3$ modes can occur to terminate the high performance phase. As mentioned in the beginning, it would be desirable to maintain $q_{\rm min}$ higher than 2 to avoid the $m/n = 5/3$ mode that can terminate the high performance phase and to avoid the $m/n = 2/1$ modes that can cause the discharges to disrupt. However, it is found that the attainable no-wall $\beta_{\rm N}$ limit can fall with the increase in $q_{\rm min}$ [13] as shown in figure 4. A further assessment of this trend is important for ITER steady state scenarios.

It has been observed that ITBs can also be formed in plasmas with very low magnetic shear. The so-called high $\beta_{\rm p}$ plasmas in JT-60U belong to this category. A series of full non-inductive current drive experiments at high performance have been achieved in this way. In high $\beta_{\rm p}$ plasmas, magnetic shear is low or even positive and q-profiles can vary from those with $q(0)$ slightly higher than unity to those with $q(0)$ around 2. An example of a steady state demonstration scenario is shown in figure 5. In this case, the q-profile is steady with $q(0)$ below 1.5 [30, 31]. On-axis N-NB was a key feature of achieving

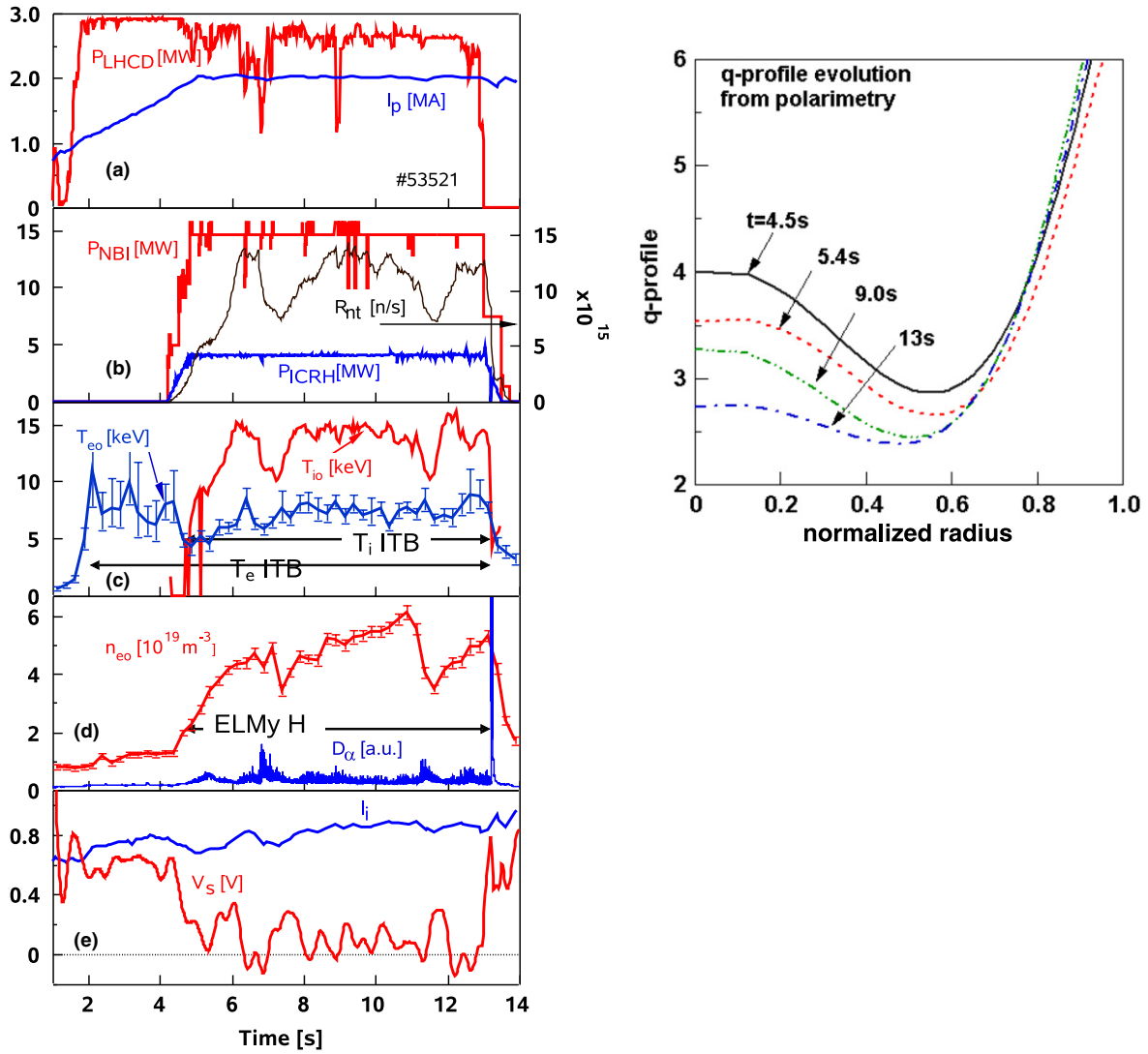

Figure 2. JET reversed shear discharge: $f_{BS} \sim 0.5$ with off-axis LHCD to maintain shear reversal. Given are (*a*) plasma current (I_p) and LHCD power, (*b*) neutral beam power (P_{NBI}), ICRH power (P_{ICRH}) and DD reaction rate (R_{nt}), (*c*) electron temperature in the centre (T_{e0}) and ion temperature in the centre (T_{i0}), (*d*) the central electron density (n_{e0}) and D_α measurements in the divertor, (*e*) the plasma inductance (l_i) and surface loop voltage (V_s). (*f*) Typical waveforms and evolution of the q-profile are shown [9].

full-CD conditions, or even slightly over driven conditions, maintained for 1.2 s, limited by the N-NB injection duration. Although $q(0)$ was low, the bootstrap current fraction in the discharge was evaluated to be 51% of the total current. In addition, no fatal resistive mode was observed at a normalized beta of 2.5, $H_{98}(y, 2) = 1.4$ and $q_{95} = 4.75$. Other examples of discharges at JT-60U approaching these conditions include the following.

(i) A full-CD discharge with $f_{BS} = 0.5$, $\beta_N = 2.5$ and $H_{98}(y, 2) = 1.2$ at higher $I_p/B_t = 1.8\,\mathrm{MA}/4.1\,T$ ($q_{95} = 4.1$) was maintained for a shorter time due to a mini-collapse [26].

(ii) A high β_p discharge at ~90% non-inductive current drive ($I_p/B_t = 1\,\mathrm{MA}/2.4\,\mathrm{T}$) with $q(0) \sim 2$ and $q_{min} \sim 1.5$ achieving $\beta_N = 2.4$ and $H_{98}(y, 2) = 1.0$ at $q_{95} = 4.5$ was sustained for 5.8 s with $f_{BS} \sim 0.45$ and the rest of the non-inductive current was driven by negative ion based neutral beam injection (N-NBCD) and positive ion based neutral beam injection (P-NBCD) [32]. Also other high β_p discharges with $q(0) \sim 2$ and an almost saturated inductive current profile have been achieved with $f_{BS} = 0.5$, $\beta_N = 2.8$ and $H_{98}(y, 2) = 1.5$ at $q_{95} = 4.0$ [19].

Thus, potential candidates for ITER steady state operation have been demonstrated. It is encouraging that $f_{BS} \sim 0.5$ has been obtained over a wide range of $q(0)$, although it is still difficult to assess what would be the preferred q-profile for use in ITER steady state operation. However, most steady state discharges have been achieved so far with a weak (positive or negative) magnetic shear configuration and q_{min} around 2 (± 0.5), with the notable exception of some high β_p regimes in JT-60U. It is important to obtain such high β_p regimes in machines other than JT-60U allowing similarity experiments to be conducted. On the other hand, further investigation should be continued on other issues. For example, in the reversed shear approach, careful attention should be paid to the control of the ITB evolution, as the ITBs tend to be too strong and make the shear reversal too deep or reach disruptive limits in JT-60U, JET and other tokamaks. In weak shear and positive

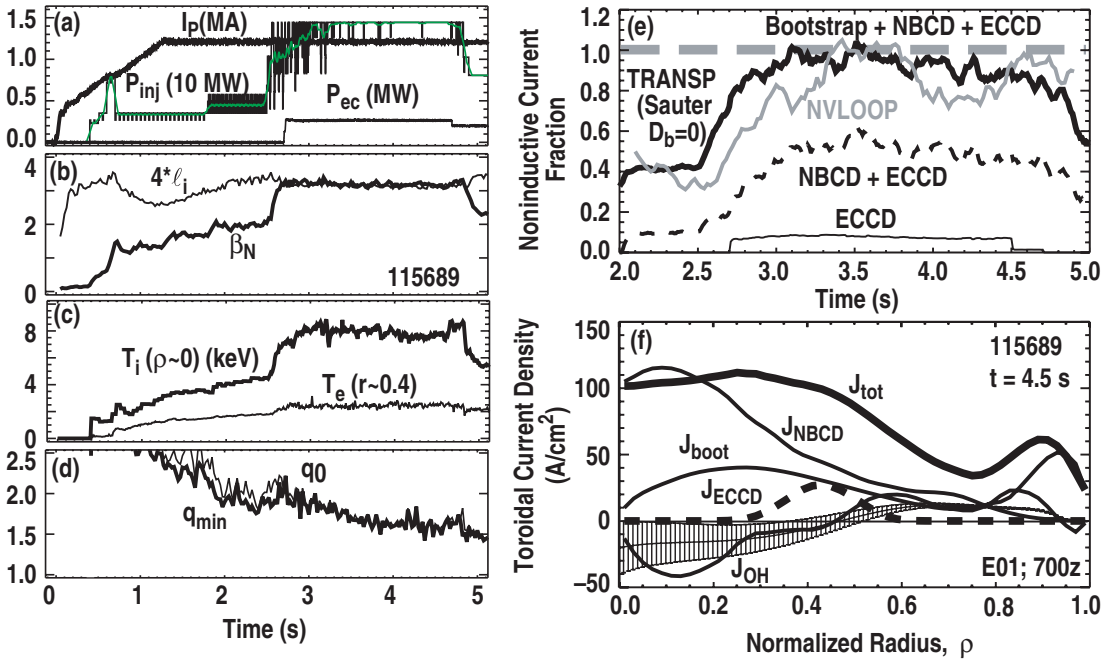

Figure 3. DIII-D full current drive discharge with $q(0) \sim 1.5$. Typical waveforms, evolution of non-inductive currents and break-up of the current profiles are shown. (*a*) Plasma current (I_p), neutral beam power (P_{inj}) and ECCD power (P_{EC}), (*b*) four times the plasma inductance (l_i) and normalized beta (β_N), (*c*) electron temperature at $r/a \sim 0.4 (T_e(\rho \sim 0.4))$ and ion temperature in the centre ($T_i(\rho = 0)$), (*d*) the central q-value (q_0) and minimum q-value (q_{min}), (*e*) various non-inductive current contributions and (*f*) profiles of the current density contributions at $t = 4.5$. Adapted from [11].

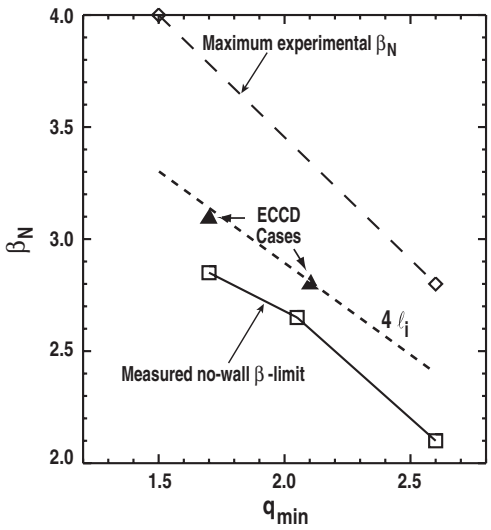

Figure 4. Dependence of the measured no-wall β_N limit and maximum attainable β_N on q_{min}. Electron cyclotron current drive (ECCD) cases are also shown as the solid triangles. The dotted line is $4l_i$ which has been shown to be consistent with the no-wall β_N limit in a variety of AT discharges in DIII-D [13].

shear discharges the impact on confinement and the evolution of the current density profile by NTMs should be investigated further. The mapping of the operation space with respect to the achievable β_N for the various different q-profiles should be investigated as suggested by results from DIII-D [29]. Furthermore, it is important to extend these DIII-D results in duration under full non-inductive current drive conditions and to reproduce them in other experiments.

3.3. Strong reversed shear and high bootstrap current scenarios

Strongly reversed shear configurations have been studied in view of ITER steady state operation. Recent experimental results in many tokamaks have shown that the formation of strong internal transport barriers (ITBs) can significantly enhance both particle and energy confinement. Consequently, the bootstrap current fraction is also very high. As discussed in chapter 2 of this issue [17], typical ITBs in RS configurations are found to be located in the vicinity of the q_{min} position (ρ_{q-min}). Once such strong ITBs are formed near ρ_{q-min}, the bootstrap current is driven locally at the ITB location, and the shear reversal becomes larger. In an extreme case, the central current density can drop to ~0, creating a central current hole in these scenarios. Within the β_N limit that is achieved in the current experiments, $f_{BS} \sim 0.5$ is expected in this scenario, although some improvement may still be required. Since f_{BS} is not very high and the shear reversal needs to be maintained, a certain amount of off-axis current drive is necessary in this scenario.

In a steady state tokamak reactor, a high fraction of the bootstrap current ($f_{BS} > 0.7$) is required for economical operation. Under these conditions the total plasma current profile is dominated by the bootstrap current profile. Once ITBs are formed in a reversed shear-based reactor plasma, the shear reversal can be quite strong according to the above-mentioned interplay between the reversed shear configuration and the bootstrap current generated at the ITB. As the bootstrap current fraction increases, the necessity of off-axis external current drive becomes lower. On the other hand, the self-generating bootstrap current needs to be consistent with the

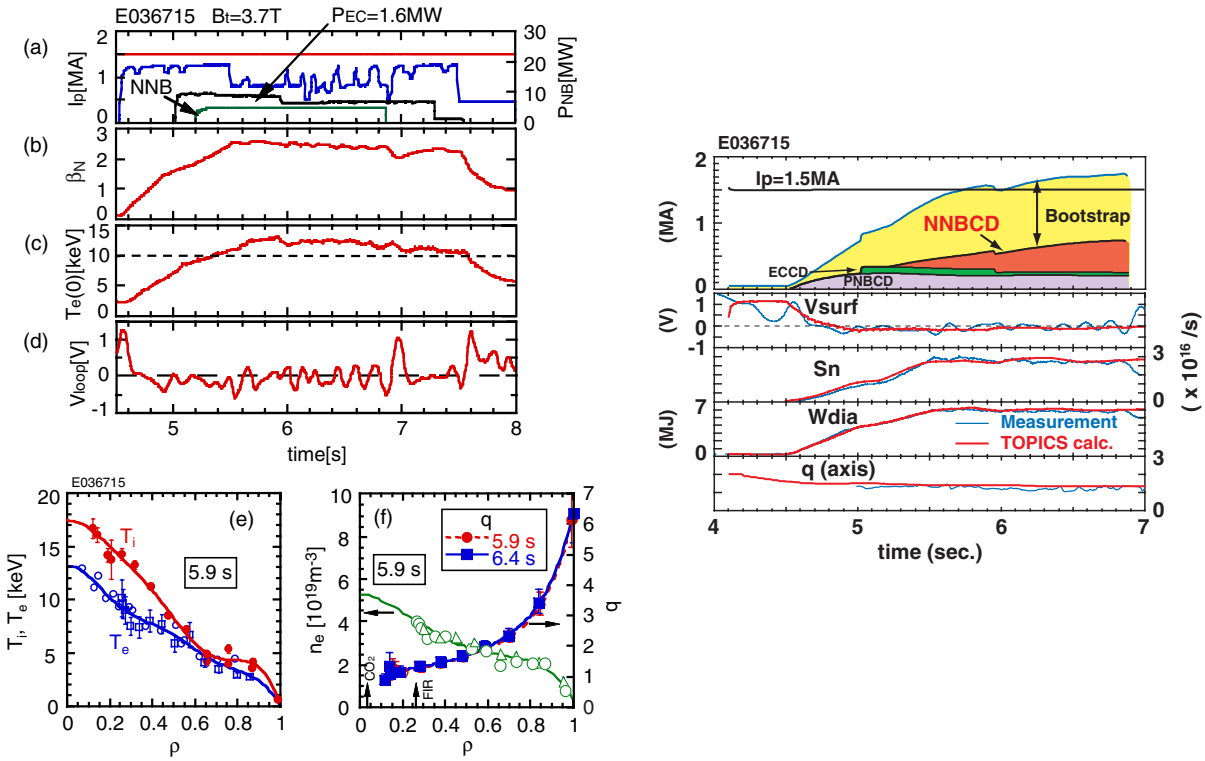

Figure 5. JT-60U high β_p discharge of full current drive with $f_{BS} = 0.5$, $\beta_N = 2.5$ and $H_{98}(y, 2) = 1.4$ at $q_{95} = 4.75$. Typical waveforms and T_e, T_i, n_e and q-profiles (left figures) are shown together with the evolution of non-inductive currents (right figure) [30, 31].

current density profile required to sustain the ITB. In JT-60U, RS plasma with $f_{BS} > 0.8$ has been maintained under full non-inductive current drive conditions (figure 6) [7]. ITBs in T_e, T_i and n_e were formed during the I_p ramp-up phase. Due to the formation of ITBs at an early stage, the q-profile is already strongly reversed. Since the pressure profile in an RS plasma, especially when $q(0)$ is high, tends to be flatter in the core region, the bootstrap current profile tends to be localized at the ITB where the pressure gradient is higher. As shown in figure 6, the total current profile measured by the MSE diagnostic is almost completely determined by the bootstrap current profile that can be evaluated with the ACCOME code [33]. As shown, the total current profile agrees quite well with the bootstrap current profile, only a small amount of externally driven current was required, driven by off-axis NBCD. Although the duration of the full-CD period is not very long, the current profile is almost unchanged due to the current ramp-down that helped to sustain a steady state equilibrium. Much longer sustainment of RS plasmas (7.4 s) with nearly full non-inductive current drive and f_{BS} near 0.75 was also demonstrated in JT-60U [32].

Also in DIII-D, plasmas with a high bootstrap fraction, $f_{BS} \sim 0.7$, have been maintained at $q(0) \sim 3$ and $q_{min} \sim 2$ with fixed Ohmic coil current (no flux being delivered from the Ohmic coil). In this discharge, NBCD and ECCD are estimated to contribute 20% and 4% of the total current, respectively, with 6% of the Ohmic current remaining [34]. In JT-60U, $f_{BS} \sim 0.9$ has been obtained in a central-solenoid-less plasma [35]. The plasma has high confinement characteristics ($H_{98}(y, 2) \sim 1.6$) but has rather low β_N. In the TCV tokamak, full non-inductive current drive with $f_{BS} > 0.7$ is obtained using ECRF only. The bootstrap current profile peaks off-axis and the total current profile indicates that the magnetic shear is reversed. Both bootstrap current and total current profile are calculated (not measured). The off-axis bootstrap current comes from strong T_e ITB with intense ECRF heating, which is the only external heating source in TCV. The ECRF power supplies current drive to achieve full-CD conditions [36].

Strongly reversed shear plasmas as well as plasmas with a high bootstrap fraction present interesting features for steady state operation. However, several issues need to be resolved. 'Strong' ITBs contribute to the enhancement of off-axis bootstrap current fraction, but their steep pressure gradient tends to reduce the MHD limit in those RS plasmas. Softening the ITB strength together with overall pressure broadening by H-mode edge formation is the key to producing the $f_{BS} \sim 0.8$ discharge in JT-60U even though β_N was <2.2 in such discharges. Due to a lower β_N limit, the high bootstrap current fraction experiments were performed at a rather high q_{95} regime, for example, $q_{95} \sim 9$ in the JT-60U case, in order to attain high enough β_p (<3.1). Although theoretical calculations have shown that β_N can be ~4–5, experimental demonstration is clearly required. On the other hand, in the lower f_{BS} (~0.5) regime similar to that expected in the ITER steady state scenario, the experimentally achieved β_N limit 2–2.5 is not far from the values anticipated in steady state operation in ITER. The above-mentioned reversed shear discharges in JET sustained with LHCD with f_{BS} up to 0.5 was obtained at $q_{95} \sim 5.5$ and $\beta_N = 1.7$. But in this regime the off-axis current drive used to prevent the shear reversal from vanishing or the RS region from shrinking is one of the key issues. Furthermore, the control of the ITB strength is a key to maintaining appropriate confinement and bootstrap current

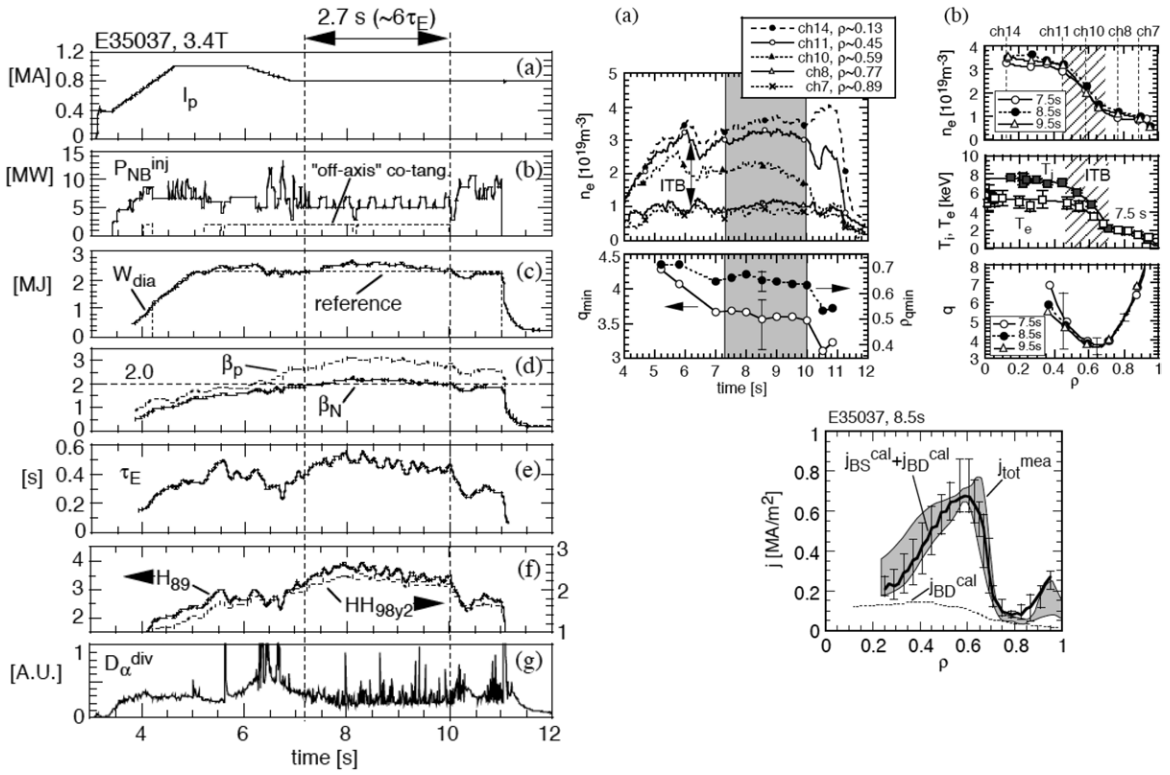

Figure 6. JT-60U reversed shear discharge of $f_{BS} > 0.8$ showing typical waveforms. From top to bottom of the left-hand figure: plasma current (I_p), neutral beam power (P_{inj}) including the off axis tangential contribution, the stored energy (W_{dia}) and the reference waveform used for feedback (dotted line), poloidal beta (β_p) and normalized beta (β_N) again with the reference waveform for β_N as dotted line, the energy confinement time (τ_E), the confinement enhancement factors H_{89} and $H_{98}(y, 2)$ and the D_α measurements in the divertor. (*a*) The evolution of the density at various locations, the time evolution of q_{min} and its location (ρ_{q-min}) are shown. (*b*) Profiles of density, temperature and q indicate that the plasma is in an almost saturated phase. Below (*a*) + (*b*): current profile at 8.5 s; the total current is consistent with the calculation and dominated by the bootstrap current [7].

fraction/profile within MHD limits. This is discussed in more details in section 5.

As shown in high performance RS experiments in JET, JT-60U, an ITB is formed in the n_e profile as well due to strong central fuelling by the NBI. This n_e ITB contributes significantly to increasing the bootstrap current. Neoclassical impurity accumulation in the core region can be kept under control under these conditions [37]. Electron heating experiments, such as the one in TCV mentioned above or LHCD in JET, ECH in DIII-D and JT-60U, have shown the formation of T_e ITB but with a less peaked or even flat n_e profile. Extension of these results towards ITER or reactor relevant parameters would shed light on this issue of density ITB formation.

For strongly reversed shear plasmas (particularly those with a current hole), confinement of fusion alphas and high energy beam particles can be an issue. The orbits of these energetic particles can be too large to be confined in the core region. However, since the orbit becomes smaller once an energetic particle escapes from the high q or current hole region, it can be confined if certain conditions are satisfied (large ITB radius, not so high q_{min}, and so on) and the confined region should not necessarily be too central as long as the pressure profile is flat inside ITB as indicated from many present RS experiments. Excitation of collective modes that can expel energetic particles out of the high-pressure region is also an issue. This is discussed in chapter 5 of this issue [22].

3.4. Hybrid scenarios with low shear and $q(0) \sim 1$

Fully non-inductive advanced scenarios, as presented in sections 3.2 and 3.3, rely upon careful tailoring of the current density profile by the external heating and current drive methods, aiming at triggering of internal transport barriers and alignment between the bootstrap current and the total current. Sufficient bootstrap current may be provided in this way to satisfy ITER's second major goal of reaching $Q = 5$ under fully non-inductive conditions. However, the stringent control requirements for scenarios with internal transport barriers (see section 5) have prompted research in advanced regimes, which are inherently stationary with respect to the current relaxation time scale, requiring only minimum control by external actuators. It was originally envisioned [38] that discharges with extended burn at lower plasma current would be intermediate between the inductive burn (baseline) scenario and the fully non-inductive (advanced steady state) scenario; therefore, this type of discharge was known as the ITER 'hybrid' scenario. Projection studies show that the requirement of such a scenario on beta and confinement is modest: $\beta_N \sim 1.9$ and $H_{98}(y, 2) = 1$ for a fusion power of 400 MW and a pulse length >1000 s. Therefore, this scenario would allow the tokamak to operate in a mode with high reliability, high neutron fluence and long pulse length for the purpose of testing various components although at relatively low Q (~5).

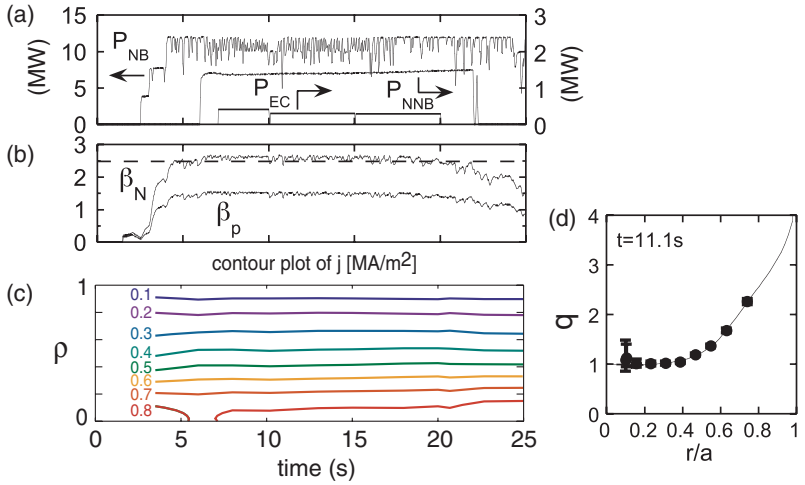

Figure 7. Hybrid discharge in JT-60U with very long pulse duration. Shown are: (*a*) the neutral beam power (P_{NB}), ECRH power (P_{EC}) and power from the negative ion based neutral beam injection system (P_{NNB}). (*b*) Poloidal beta (β_p) and normalized beta (β_N). (*c*) The evolution of the current density at various locations. No change in the current density profile is observed as long as full power is applied; an example of the q-profile at $t = 11.1$ s is given in (*d*).

Most recently it was found that discharges with $q_{95} = 3.6$–4.2, $q(0) \sim 1$ and weak central shear can have an improved energy confinement compared with H-mode confinement scaling [12]. Discharges of this type if realized in ITER would allow a high fusion power, long pulse length and $Q \sim 10$ to be obtained [39]. In particular, these discharges are nowadays referred to as hybrid scenarios. The different q-profile of the hybrid scenario, compared with the standard inductive H-mode scenario, prevents sawtoothing $m = 1/n = 1$ MHD activity in the core and the triggering of large $m = 3/n = 2$ or $m = 2/n = 1$ neoclassical tearing modes. These MHD events generally lead to significant reduction in confinement and limit the plasma performance as observed in the standard H-mode regime for ITER operation at $q_{95} \sim 3$. By operating at lower plasma current compared with the ITER reference scenario, the hybrid scenario reduces the electromagnetic load in the case of disruptions and lengthens the possible discharge duration through a reduced flux consumption (although not steady state). Hence, the rapid progress made recently, and described below, implies that the hybrid scenario is now considered as an advanced reactor relevant scenario. Future developments of such a scenario might even lead to the concept of 'quasi steady state' reactor.

In JT-60U, a high β_p mode with H-mode edge (high β_p H-mode) has been optimized in view of steady state operation and high β capability since 1994 [4]. A high β_p H-mode is characterized with improved core confinement owing to the formation of internal transport barriers in n_e, T_i and often T_e with a good H-mode pedestal, which can support higher β_N. Formation of ITBs contributes not only to confinement improvement but also to higher bootstrap current fraction ($f_{BS} > 0.5$). A discharge without sawteeth was sustained at $\beta_N = 2.3$ for 2.6 s with $q_{95} \sim 3.4$ [26]. More recently, discharges have been obtained with β_N at about 2.3 for 22.3 s (0.9 MA/1.6 T, $q_{95} = 3.1$–3.2) and $H_{89}\beta_N/q_{95}^2 = 0.40$ for about $120\,\tau_E$. Under these conditions, the current density profile was stationary for the duration of the high power-heating phase [40], with a wide low shear volume and $q(0)$ just below 1. Higher beta ($\beta_N = 3$) was sustained with higher power although for a shorter time (6 s) (see figure 7). These recent experiments confirm the potential of the hybrid scenario for obtaining improved confinement and stability over standard H-modes under stationary conditions.

Several experiments [2, 41, 42] have developed stationary H-modes with high confinement, $H_{98}(y, 2) > 1$ and good stability $\beta_N = 2$–3. An example from ASDEX Upgrade is given in (figure 8), where this mode of operation is called the 'Improved H-mode'. Optimization of this regime in recent years in JT-60U [4, 40], ASDEX Upgrade [12, 43] and DIII-D [44, 27] is now known under the common name 'Hybrid scenario'. Key to reaching the hybrid regime is to obtain different stationary current density profiles compared with standard H-modes. Experiments in ASDEX Upgrade and DIII-D show that this is obtained by heating during the current rise phase of the discharge, at moderate neutral beam power (2.5–5 MW). In the subsequent main heating phase, beta can be increased, with either fishbone activity in the core (ASDEX Upgrade) or a small 3/2 neoclassical tearing mode (DIII-D) creating a central q-profile with very low magnetic shear and $q(0)$ near 1. Operating at q_{95} near 4, without sawteeth allows conditions where beta can be further increased to $\beta_N \sim 3$. These discharges have no sawteeth and peaked density profiles with $H_{98}(y, 2)$ up to 1.4, for the duration of the heating phase. Detailed transport analyses show that in such a regime the temperature profiles remain in the so-called stiff regime; the temperature gradients do not exceed a critical gradient length set by the turbulence in the plasmas [45]. In ASDEX Upgrade this demonstrated the operation of this regime at 80–90% of the Greenwald density limit, in discharges with $\delta = 0.43$, and only a small reduction in confinement ($H_{98}(y, 2) = 1.1$–1.2), while sustaining $\beta_N = 3.5$ and peaked density profiles, typical for this scenario (see figure 9, [23]). Discharges in DIII-D on the other hand achieve even higher performance (with $\beta_N H_{89} \sim 9$) operating for ~1 s near the estimated no-wall β limit. Furthermore, long pulse experiments in DIII-D maintain the particle balance by active pumping rather than by transient wall conditioning (figure 10 [13]).

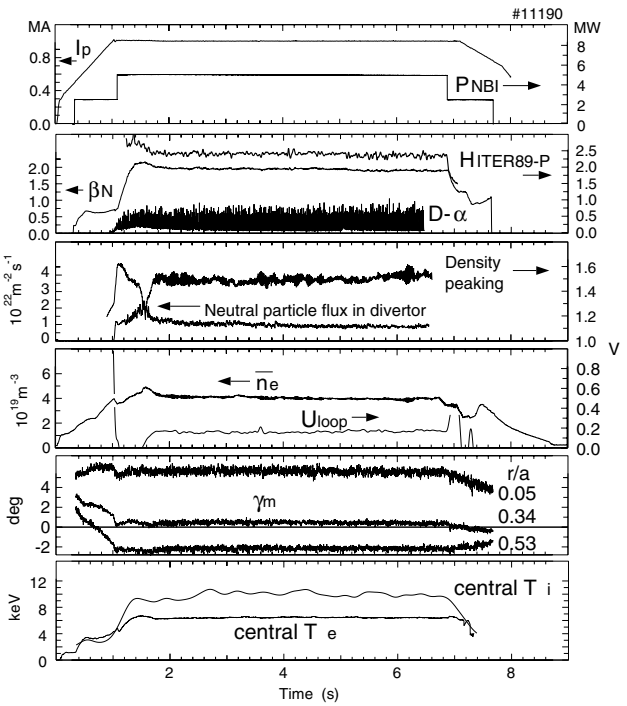

Figure 8. One of the earliest reported improved H-mode discharges in ASDEX Upgrade [41] at low triangularity ($\delta = 0.17$), stationary for 40 timescales of the energy confinement time. From top to bottom: plasma current (I_p) and neutral beam power (P_{NBI}). The confinement enhancement factor H_{89}, normalized beta (β_N) and D_α measurements in the divertor. Density peaking factor and neutral particle flux in the divertor. The line averaged density (n_e) and loop voltage (U_{loop}). The polarization angles of the MSE diagnostic, representing the local poloidal magnetic field values, are constant in time, reflecting the stationarity of the q-profile. The central electron (T_e) and ion temperatures (T_i).

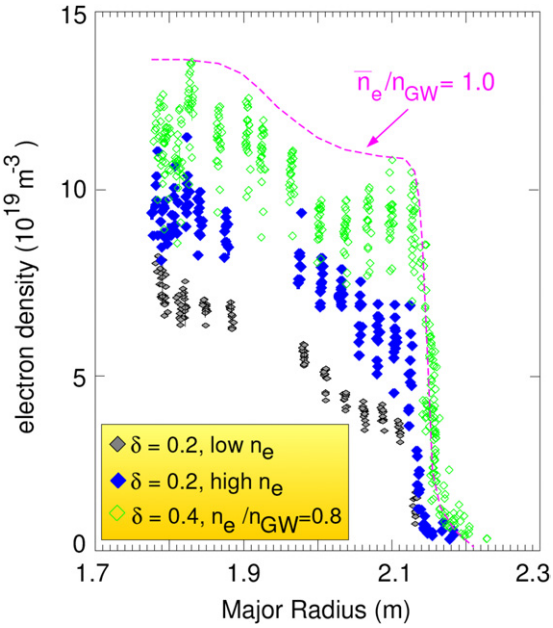

Figure 9. Increase of the density in improved H-mode scenarios. The lowest density is obtained for an improved H-mode at low triangularity ($\delta = 0.17$) with NBI fuelling only. The closed diamonds show the increase in the density at the same triangularity with additional gas fuelling up to 65% of the Greenwald density limit. At the same NBI power and gas flow rate the open diamonds show the density profile at a triangularity of $\delta = 0.43$. The electron density is measured with Thomson scattering; for each case two identical discharges are taken, combining measurements at the edge and core.

JT-60U, ASDEX Upgrade and DIII-D established this regime independently, in a search for stationary conditions at high performance. Typically, these discharges achieve values for the figure of merit ($H_{89}\beta_N/q_{95}^2$) near 0.40, or higher, extrapolating to $Q = 10$ in ITER [39]. Moreover, non-inductive current fractions of $f_{NBCD} \sim 0.5$ in combination with benign MHD modes in the core (fishbones and NTMs) maintain a stationary q-profile without active control. Building on the demonstration of the hybrid regime, discussions within the steady state operation topical group and the transport physics topical group of the ITPA (International Tokamak Physics Agreement) led to proposals for establishing the regime in more devices (such as JET) within the frame of an increased level of international collaboration between fusion experiments. Experiments in JET started with the aims: (i) of establishing the conditions for the hybrid scenario at 1.4 MA/1.7 T ($q_{95} = 3.9$), with similar non-dimensional parameters (e.g. ρ^* and q-profiles) compared with ASDEX Upgrade, (ii) of producing stationary discharges for the duration of the heating phase and (iii) of documenting the differences (if any) when going to lower ρ^*, at 2.8 MA/3.4 T [14]. The results of these experiments show that the hybrid scenario can be obtained at JET at 1.4 MA/1.7 T by matching the plasma shape, q-profile and ρ^* of ASDEX Upgrade (see figure 11). Stationary conditions are achieved with small NTM and fishbone activity in the core at similar β_N, H-factor, MHD and profiles as in ASDEX Upgrade or DIII-D. The figure of merit for fusion gain, $H_{89}\beta_N/q_{95}^2$, reaches values up to 0.42 in JET at $q_{95} = 3.9$, in line with the results from ASDEX Upgrade and DIII-D at similar q_{95}.

Experiments optimizing the regime at lower ρ^* in JET and JT-60U and documentation of the hybrid scenario at ASDEX Upgrade and DIII-D are ongoing. In particular, the documentation of the operational domain at various different values for q_{95} is almost completed (DIII-D, ASDEX Upgrade and partly JET), showing that the highest β_N is achieved for q_{95} of about 4. However, operation at lower $q_{95} \sim 3.2$ with $\beta_N \sim 3$ is achievable leading to a possible extrapolation to $Q \geqslant 10$ in ITER. Mapping of the operational domain with density has started in DIII-D and in ASDEX Upgrade. RF-dominated hybrid scenarios have been achieved in JET at low ρ^*, although more optimization is needed to optimize their performance [46]. 'Soft' MHD events typical of a hybrid discharge have been observed. However, beta limits were not tested since a much larger amount of additional power (ICRH and NBI) is required (see figure 12). Hybrid regimes have been achieved with ITER-relevant T_e/T_i and they are compatible with very low edge activity and low-pressure pedestal [46]. A large volume of low magnetic shear with $q(0)$ close to 1 seems to be the key to achieving 'hybrid' scenarios. However, it is important to understand the role of and the type of MHD modes observed in the current profile evolution and the need for active control in ITER. It is also important to assess further the operational space for high beta operation and for ITER-relevant ρ^* and ν^*. More experiments are therefore

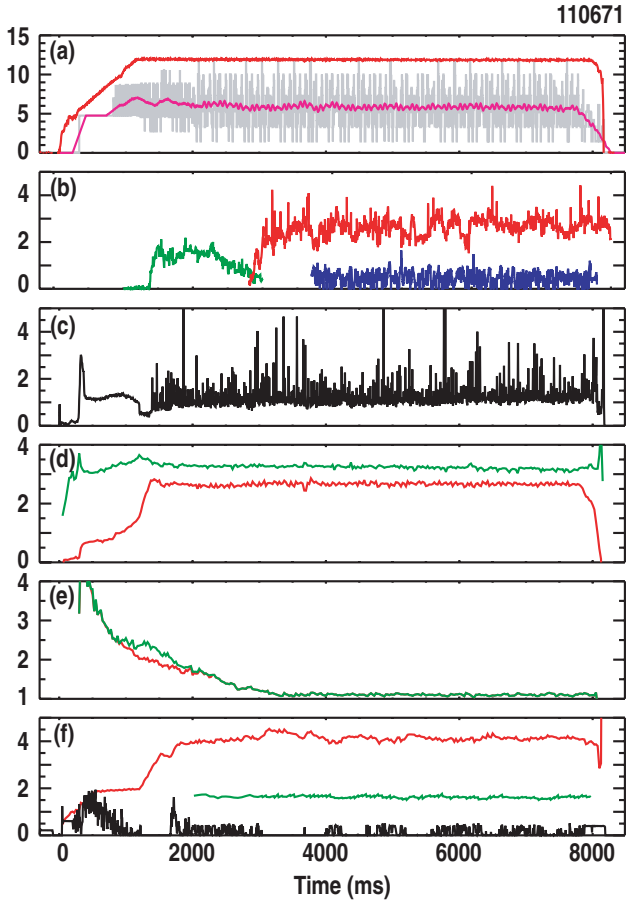

Figure 10. Time histories of various plasma parameters for a typical long-pulse stationary discharge ($B_T = 1.7$ T) in DIII-D. (*a*) 10× plasma current I_p (MA), neutral beam power P_{NB} (MW), P_{NB} with a 200 ms moving average (MW), (*b*) magnetic perturbations measured at the vacuum vessel (G), (*c*) D_α emission from the upper divertor (10^{15} photons cm^{-2} s^{-1}), (*d*) normalized beta (β_N) and 4× internal inductance (l_i), (*e*) q_{min} and $q(0)$, (*f*) line averaged density n_e (10^{19} m^{-3}), Z_{eff} from carbon, gas flow $\phi_D/100$ (not including neutral beam sources) (torr l s^{-1}).

needed to confirm the present very promising perspectives to use 'hybrid' scenarios in ITER.

3.5. A comparison between the different advanced scenarios

In order to evaluate the experimental results from different experiments, an international database has been set up. The construction of an international database for advanced tokamak discharges is an activity coordinated under the International Tokamak Physics Activity (ITPA) [47]. Data from ASDEX Upgrade, DIII-D, FTU, JET, JT-60U, RTP, T-10, TCV, TFTR and Tore Supra experiments have been collected in recent years. The dataset now contains a comprehensive set of scalar data. A limited set of profile data has been used for detailed transport analysis and will not be discussed here (see chapter 2 of this issue [17]). The database documents an encouraging progress in the development of advanced scenarios for ITER, concentrating on the operation space of advanced scenarios achieved so far. It is to be noted that some of the parameters in this database are sought to better define the spatial location and occurrence, in time, of the internal transport barrier [48]. The discharges have also been assessed in terms of their fusion performance and capability for eventually reaching steady state [49]. The results of the analysis show that hybrid scenarios have a moderate improvement in overall confinement and can operate close to the no-wall beta limit [27]. Reversed shear discharges typically have higher confinement, but the corresponding fusion performance tends to decrease with increasing pulse duration and plasma density [50]. As discussed in section 2, $H_{89}\beta_N/q_{95}^2$ is used as a figure of merit for the performance. In figure 13 this figure of merit is plotted versus $\varepsilon^{0.5}\beta_p$, which is a measure for the fraction of self-generated bootstrap current for similar q-profiles (ITER aims at $H_{89}\beta_N/q_{95}^2 \sim 0.35$–$0.45$ and $\varepsilon^{0.5}\beta_p \sim 0.8$–$1.0$). The results for the two regimes are plotted showing substantial differences between stationary (duration of the high performance phase $>10\,\tau_E$) and transient (duration of the high performance phase $<10\,\tau_E$) results from reversed shear discharges.

These results emphasize that high β_N operation in the range of 3 has only been achieved with broad pressure profiles. Statistical analysis indicates that the width of the improved core confinement region should be large enough to avoid the development of a narrow domain with a too localized and very steep pressure gradient. Finally, ITER plasmas will be in a somewhat different domain of dimensionless plasma parameters compared with regimes of present-day tokamaks as it will require operating plasmas with lower values of the normalized Larmor radius (ρ^*), collisionality (ν^*) and ratio of the central ion and electron temperatures T_{i0}/T_{e0}. Hence, collaborative experiments are being promoted aiming at a more comprehensive dataset of advanced scenarios to establish a basis for more robust extrapolation of present-day experiments to ITER.

4. Actuators for steady state operation

4.1. Introduction

External heating systems heat the plasma to a burning state and also control the safety factor profile. On ITER several auxiliary heating and current drive systems are planned: negative ion neutral beams with neutral beam energies of 1 MeV, electron cyclotron heating in a frequency range near 170 GHz, lower hybrid wave injection at 5 GHz and ion cyclotron heating at 40–55 MHz. Each has technological and physics-based strengths and weaknesses. For example, 1 MeV sources of neutral beam are challenging to construct, while the coupling to the plasma is straightforward. Similar advantages and disadvantages are found for electron cyclotron heating, with an added benefit of a highly localized and controllable deposition profile. Lower hybrid current drive offers highly efficient current drive in the periphery of the plasma (where it is likely to be needed), with a more complicated coupling structure and less precise deposition control (than ECCD). The role of ion cyclotron heating is primarily to heat the plasma to a burning condition, but it may also be used for current profile control in certain situations.

The degree to which current profile control will be possible is ultimately limited by the constraints imposed by the physical processes of the particular auxiliary system. In this section, progress in characterizing the power deposition

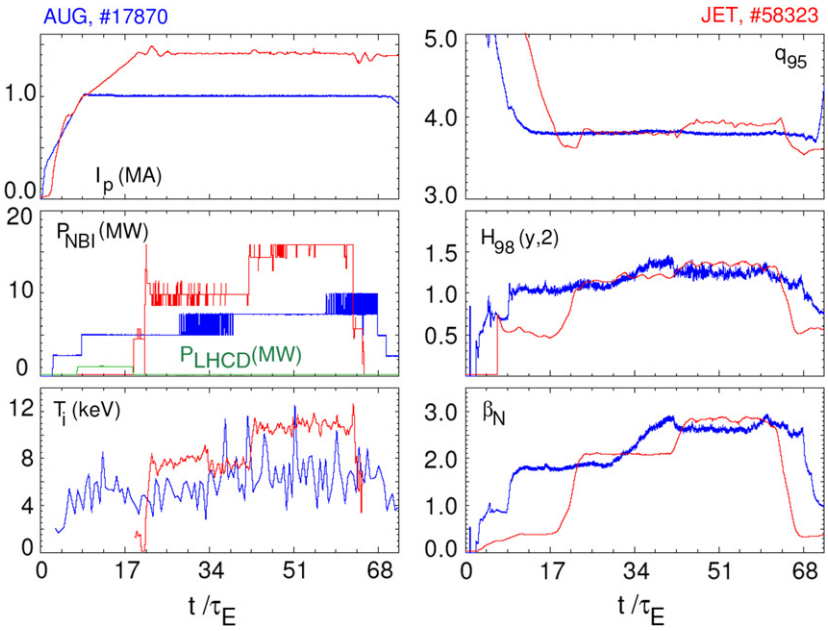

Figure 11. Matched hybrid scenario discharges in ASDEX Upgrade (dark traces) and JET. For the x-axis the time duration is normalized to the energy confinement time during the high beta phase of the discharges (115 ms for ASDEX Upgrade and 210 ms for JET). Shown are plasma current (I_p), neutral beam power (P_{NBI}) and LHCD power (for JET in green), central ion temperatures (T_i), edge safety factor (q_{95}), the confinement enhancement factor $H_{98}(y, 2)$ and normalized beta (β_N).

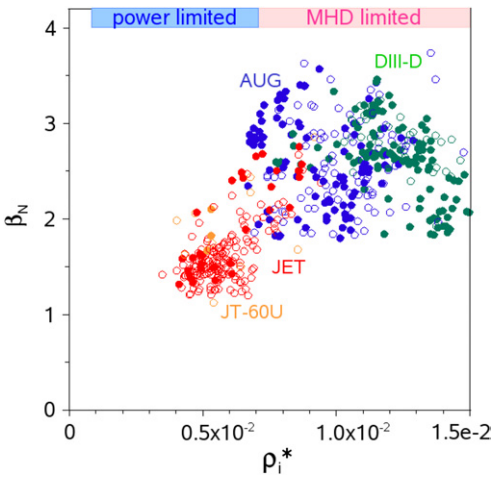

Figure 12. Database for β_N versus ρ^*. Closed circles refer to stationary hybrid discharges. Open symbols are from transient discharges (duration less than 10 energy confinement times). Discharges from JET and JT-60U limited by the total heating power available are labelled 'power limited'. ASDEX Upgrade and DIII-D reach the beta limit in hybrid discharges; this region of the figure is labelled 'MHD limited'.

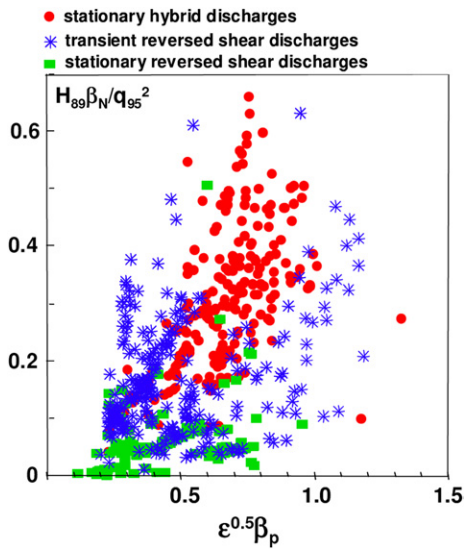

Figure 13. $H_{89}\beta_N/q_{95}^2$ versus $\varepsilon^{0.5}\beta_p$ for two different regimes: hybrid scenarios and reversed shear, non-inductive scenarios. For reversed shear discharges both transient and stationary results are given.

and measuring the driven current from the planned auxiliary heating and current drive systems is described. Progress has been made since the IPB in experimentally testing the validity of theoretical models and in establishing their predictive capability. The predictive capability of the models has been tested by first developing techniques for measuring both the power deposition profile and the driven current profile and then by comparing these measured radial profiles with predictions from theory.

In what follows, each of the auxiliary systems is briefly described, along with progress on the technology that has occurred during the last five years. For each system, there has been an attempt to review the state of the theoretical tools used for modelling heating and deposition, and then progress on comparisons between theory and experiment is presented. To the extent possible, we have focused here on tests of the radial deposition profiles and the resultant driven current density. A brief summary of applications of these actuators in providing new tokamak physics is given.

4.2. Current drive by negative ion based neutral beams

Neutral beams of deuterium and tritium have the potential to heat and drive current in the core of burning plasmas. In order to penetrate the dense, hot plasmas of ITER, neutral beam energies in the range of several hundred keV to 1 MeV are required, energies much higher than typical of most neutral beam injectors used in present-day tokamaks. Efficient production of high energy hydrogen atoms requires the use of negative ion based neutral beams, which can deliver power deeply into the core of the plasma, but most present-day systems use injectors that are based on the acceleration of positive ions. The higher energies possible with negative ions can potentially penetrate the core of burning plasmas, providing central power deposition as well as an efficient current drive source. The present ITER plan is to use such a heating system. H^- ion beams of 1 MeV and 140 mA level have been generated with a substantial beam current density (100 Am^{-2}) [51]. The feasibility of such systems at several hundreds of keV has been demonstrated on JT-60U [52, 53]. The N-NBI system at JT-60U (at present, the only tokamak with an N-NBI system) has reached an injection power of 5.8 MW at 400 keV and a continuous injection of 2.6 MW at 355 keV. The Large Helical Device (LHD) also adopted an N-NBI system for heating. The LHD system has achieved injection powers of 10.3 MW (in total) and 4.4 MW (per injector) at 180 keV [54]. This section reviews ionization processes for high energy atoms injected by N-NB, experiments at JT-60U with N-NB and the subsequent comparisons between experiment and theory, including effects of magnetohydrodynamic instabilities on the N-NB current drive. The results validate the fundamental processes of the power deposition and also demonstrate the possibility of driving current with neutral beams efficiently.

4.2.1. Ionization process of fast neutral atoms injected by N-NB. Three basic atomic processes lead to neutral beam ionization: charge exchange, ionization by ions and ionization by electrons. Two theoretical models for beam particle ionization are proposed: a single step ionization process which considers only ionization by the first impact and a multi-step ionization process [55] which considers the single step ionization process as well as an excitation process and the subsequent ionization. The multi-step ionization process can be important in neutral beams with energies greater than several hundred keV. The enhancement factor of the ionization against the single step process is theoretically predicted to increase with the beam energy E_B and the electron density n_e.

The ionization process has been studied experimentally in JT-60U by the analysis of shine-through measurements [56, 57]. The shine-through power is estimated from the temperature rise of the armour tiles facing the N-NB lines. Figure 14 shows the n_eL dependence of the measured shine-through fraction of the 350 keV N-NB injection, where n_eL is the integrated electron density along the beam path in the plasma. Both plasma and beam species are hydrogen, and the ranges of the electron temperature T_e and the effective plasma ion charge Z_{eff} are 1.8–3.7 and 1.3–2.2, respectively. The theoretical predictions for both single step and multi-step ionization processes are also shown. On comparing the

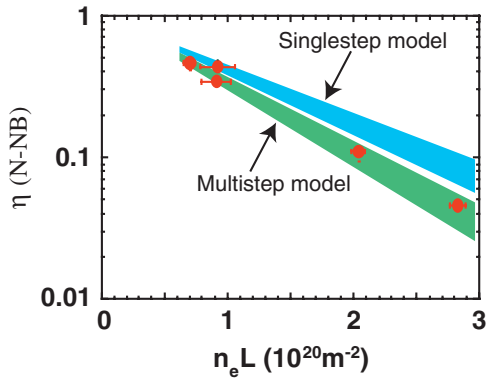

Figure 14. The n_eL dependence of the shine-through η for N-NB injection. The predictions for single step and multi-step processes are also shown. The shaded areas correspond to a 20% error in Z_{eff}. $E_B = 350$ keV, $n_e = (1–4.1) \times 10^{19}$ m^{-3}, $T_e(0) = 1.8–3.7$ keV and $Z_{eff} = 1.3–2.2$. The cases presented are for a hydrogen plasma and hydrogen beam.

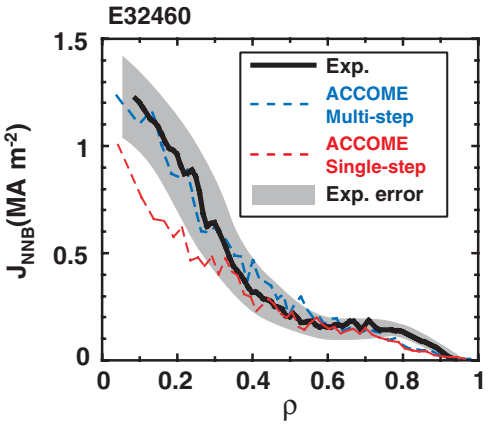

Figure 15. Measured (——) and calculated (- - - -) N-NB driven current density profiles. Error due to uncertainties in the measurements is indicated by the shaded region. Thin and thick dashed lines correspond to theoretical calculation by ACCOME using the single step and multi-step processes for ionization cross-section for injected N-NB particles, respectively.

experimental results with those of the theoretical calculation, the cross-section for electron loss due to multi-step processes has been calculated by adopting the latest reliable atomic data [57] based on the work by Janev *et al* [55]. The experimental results agree with the multi-step ionization process over a wide range of $n_eL(0.7–3.0) \times 10^{20}$ m^{-2} corresponding to $n_e = (1–4.1) \times 10^{19}$ m^{-3}) within the experimental uncertainty (mainly due to uncertainty in Z_{eff}). Thus, it has been confirmed that the multi-step ionization processes are essential for high energy neutral beams.

4.2.2. N-NB current drive capability. Profiles of the non-inductive current density driven by N-NB injection at $E_B = 360$ keV have been measured [58] in L-mode plasmas with $I_p = 1$ MA, $n_e = 0.9 \times 10^{19}$ m^{-3}, $T_e(0) = 4$ keV and N-NB injection power of 3.7 MW, using a loop voltage profile analysis made possible by the motional Stark effect (MSE) diagnostic [59]. The measured N-NB driven current density profile is compared with the calculation using the current drive code ACCOME [33] in figure 15. The ACCOME calculations

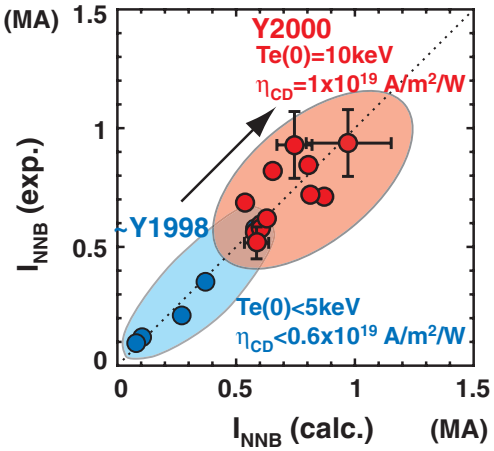

Figure 16. Comparison of the N-NB driven current I_{NNB} (exp.) with I_{NNB} (calc.) shows an agreement over a wide range from 0.1–1 MA. Y1998 and Y2000 denote data obtained in 1998 and 2000, respectively.

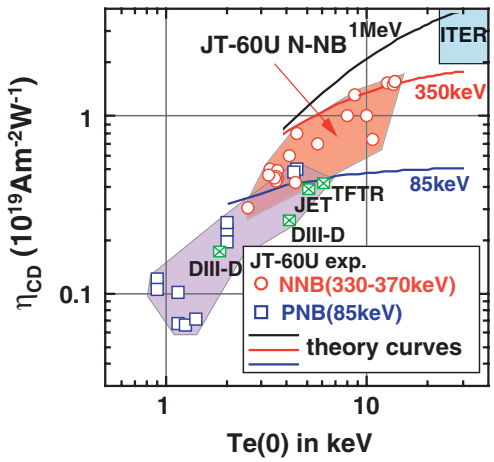

Figure 17. Electron temperature T_{e} dependence of the current drive efficiency η_{CD}. TFTR, JET and DIII-D data have been taken from [339–341].

were performed using two models of the ionization cross-section for the injected N-NB particles, i.e. the single step model and the multi-step model. The measured profile agrees well with the calculation using the multi-step model within the experimental uncertainty. The experimentally measured N-NB driven current is compared with the calculated current in the range 0.1–1 MA in figure 16 [31]. This wide range is mainly due to the electron temperature variation up to 10 keV. The measured values are the integrations of the N-NB driven current profiles determined in the same manner as in figure 15. The agreement between the measurement and theoretical prediction presented in figures 15 and figure 17 proves the validity of NB current drive theory and gives greater confidence in predicting the performance of high energy neutral beam current drive in ITER and fusion reactors.

A comparison of the measured temporal evolution of the current density profile with a discharge simulation using the time-dependent transport code [60] showed a record value of the NB current drive efficiency $\eta_{\mathrm{CD}} = 1.55 \times 10^{19}\,\mathrm{A\,m^{-2}\,W^{-1}}$. This was achieved at $T_{\mathrm{e}}(0) = 14\,\mathrm{keV}$ in a high β_{p} H-mode plasma, simultaneously with high confinement ($H_{98}(y,2) = 1.4$) and high plasma pressure ($\beta_{\mathrm{N}} = 2.5$) at $I_{\mathrm{p}} = 1.5\,\mathrm{MA}$ in a fully non-inductively driven discharge [31]. The measured dependence of η_{CD} on the electron temperature and the beam energy is shown in figure 17. Here, the current drive efficiency is defined as $\eta_{\mathrm{CD}} \equiv n_{\mathrm{e}} R I_{\mathrm{CD}} / P_{\mathrm{abs}}$, where R is the plasma major radius, I_{CD} is the total driven current and P_{abs} is the power absorbed in the plasma. The current drive efficiency was confirmed to increase with beam energy and electron temperature, at temperatures above 10 keV (approaching the ITER regime), as NB current drive theory predicts. The experimental demonstration of the N-NB current drive capability gives confidence that the required current drive performance can be achieved in ITER.

4.2.3. Effects of magnetohydrodynamic (MHD) activities and turbulence on neutral beam current drive. The results on NB current drive (NBCD) in MHD-quiescent plasmas are encouraging for ITER. However, it has been pointed out that MHD instabilities, such as toroidicity-induced Alfvén eigenmodes (TAE), sawteeth, fishbones and tearing modes, may affect NBCD performance through loss and redistribution of injected beam ions and redistribution of the fast ions in both velocity space and real space.

In JT-60U, appearance of beam-induced Alfvén eigenmodes has been observed when N-NB with $E_{\mathrm{B}} \sim 360$ keV was injected into plasmas with an appropriate density and a relatively low toroidal magnetic field. For abrupt large-amplitude events (ALEs) [61], redistribution of energetic ions has been demonstrated by using a neutron emission profile measurement [62]. An example of such energetic particle-induced MHD activities on NBCD is shown in figure 18 [31]. Synchronized with the appearance of bursting modes, the neutron emission signal saturates, and a sudden change in the toroidal electric field (time derivative of the poloidal flux) is observed near the plasma centre. Deduced profiles of N-NB driven current indicate that the N-NB driven current density near the plasma centre is reduced after an appearance of bursting modes. Reduction of the N-NB driven current due to these modes is estimated to be ~7% of the total driven current. Although the reduction in the total driven current is not large, the deformation of the local driven current profile is substantial. It is likely that the effects of energetic particle modes (EPMs) limit the obtainable current density profile [31].

Reduction of NBCD due to enhanced transport of NB injected ions in the presence of tearing modes was observed in DIII-D [63]. An explanation based on stochastic particle orbits resulting from overlapping of sideband island structures in the particle phase space was applied to the DIII-D result [64]. Evidence for enhancement of fast ion transport during tearing modes was also observed in JT-60U, where the beam energy dependence of the anomalous transport was also reported [31, 60]. While the anomalous fast ion transport associated with the magnetic island structure can explain the results, it may also be possible that other mechanisms are at play. For example, even in MHD-quiescent plasmas, the discrepancy between measured and predicted NBCD profiles has been reported. In DIII-D, the on-axis NB driven current profile for on-axis NB, determined from the loop voltage profile analysis using MSE, was observed to be broader than the prediction from the TRANSP code [65]. In ASDEX Upgrade and JT-60U,

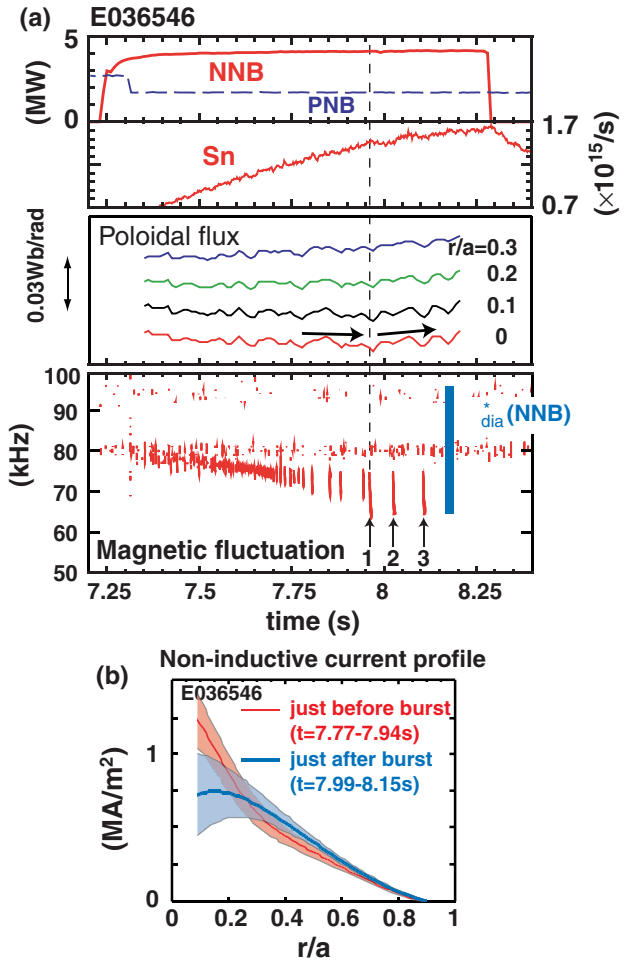

Figure 18. An example showing the effect of energetic particle induced modes on NBCD. (*a*) A bursting mode was observed during 4 MW N-NB injection. Shown are the power of the negative ion based neutral beam system (N-NB) and the positive ion based neutral beam system (PNB), the measured poloidal flux at several locations and the evolution of frequency spectra taken from fast magnetic data. (*b*) Comparison of non-inductive current profiles just before and just after the burst activity indicated by an arrow '1' in (*a*) [31]. The non-inductive current is mostly driven by N-NBCD since the bootstrap current and NBCD at lower energy are negligible.

discrepancies between time-dependent simulations (using the ASTRA transport code) of MSE signals and measured values were observed in off-axis co-directional NBCD [66]. Although a conclusive result has not been obtained presently, further research effort is required to investigate the role of turbulence on fast ion transport. Finally, a thorough benchmarking of the various NBCD models used in the simulation codes needs to be performed.

4.2.4. Summary. Advances in neutral beam injection systems and the development of the current profile measurement allow experimental validation of the neutral beam current drive in ITER-relevant conditions. The current drive capabilities of high energy neutral beams and relevant physics have been confirmed in JT-60U experiments using an N-NB operated at 300–400 keV. The ionization of the injected beam neutrals is enhanced through a multi-step ionization process. Measured N-NB driven current profiles show good agreement with theoretical predictions. The highest NB current drive efficiency of 1.55×10^{19} A m^{-2} W^{-1} was achieved in high β_p H-mode plasmas in JT-60U. These experiments demonstrate the favourable scaling of the NB current drive efficiency with beam energy and electron temperature. The results give confidence in the projections of NB current drive to ITER. On the other hand, it is observed that MHD instabilities could affect NB fast ions and degrade the current drive efficiency. The measurements indicate that energetic particle modes (EPMs) expel N-NB injected ions from the central region reducing the N-NB driven current in the centre [31]. Reliable assessment of EPM effects in ITER requires more detailed measurements and an improved theoretical basis. Recently, discrepancy between measurement and theory has also been reported in MHD-quiescent plasmas. Further research is required to assess the impact of these results on NB current drive in ITER.

4.3. Heating and current drive by electron cyclotron waves

4.3.1. Introduction. Heating (ECH) and current drive (ECCD) by means of electron cyclotron waves have become well-established approaches in tokamaks. See the reviews [67–70] and references therein or for ECRH technology see [71]. The characteristics of ECH and ECCD to deposit power or current in a localized controllable way makes these techniques applicable to many objectives not addressable by other heating or current drive approaches. ECH and ECCD have been applied to such objectives as plasma start-up and heating, the generation and maintenance of desired current profiles and stabilization of magnetohydrodynamic (MHD) instabilities. The experimental work is well supported by theory, as encapsulated in practical and well-validated computer codes. This provides a high degree of confidence in the projections for use of electron cyclotron (EC) waves in future devices such as ITER.

EC power has technical advantages as well. The EC wave propagates in vacuum and couples efficiently to the plasma at its boundary, unlike other radiofrequency techniques. This allows the wave launcher to be distant from the plasma and implies that the coupling is insensitive to the plasma parameters at the boundary. These are important advantages for a thermonuclear device such as ITER [1], where objects close to the plasma will be at risk of damage. Steering of the EC power may be done by using movable mirrors placed behind the first wall or by remote steering in which the movable parts are far removed from the vacuum vessel, as pointed out originally by Prater *et al* [72]. In addition, the peak power density can be very high at the antenna without breakdown, so the antenna can be small with corresponding benefits regarding neutron shielding, containment of tritium and mechanical support. Because of the short wavelengths involved, even a small antenna has modest diffraction so that the beam of EC power stays narrow, supporting applications that need highly localized deposition.

The predictive understanding of the physics, the experimental demonstration of applications of this physics and the development of suitable high power sources have resulted in a major experimental effort worldwide, with EC systems in the MW range being implemented on the ASDEX Upgrade

[73], DIII-D [74], FTU [75], JT-60U [76], MAST [77], T-10 [78], TCV [79], TEXTOR [80] and Tore Supra [81] tokamaks.

4.3.2. Electron cyclotron heating (ECH). Wave propagation and absorption is well understood in present-day tokamaks. To obtain predictive information on the location of the ECH power, ray tracing codes or Gaussian beam propagation codes have been developed. Ray tracing codes such as TORAY-GA [82, 83] and BANDIT-3D [84] assume geometric optics: that is, a Gaussian beam may under some conditions be simulated as an array of independently propagating rays. In the cases in which the beam converges due to a focusing element and the beam spread is not large, the geometric optics of ray tracing may be inadequate and the beam propagation approach may be needed. In this approach the trajectory of the centre of the beam is determined as in the ray tracing case, but the transverse properties of the wave are determined in a way which naturally includes the diffraction and self-interference effects. Gaussian beam codes include TORBEAM [85,86], ECWGB [87,88] and OGRAY [89].

The literature contains a very large body of work in which EC waves are used to heat a plasma; see references cited in [67–70]. Modulating the EC power and observing the transient plasma response may test the propagation and absorption. Analysis of the radial behaviour of the amplitude and the phase of the response of the electron temperature provides a sensitive measurement of the radial location of the heating. This work supports in substantial detail the validity of the calculation of wave propagation and absorption by the codes. Electron cyclotron current drive is an even more sensitive test of the theory as pointed out in [70].

4.3.3. Electron cyclotron current drive (ECCD). Electron cyclotron waves can drive current in a toroidal plasma. Since the wave absorption may be highly localized in space near the intersection of the wave with the resonance, the driven current may also be localized in a controllable manner. This localization and controllability offer the opportunity to apply ECCD to tasks such as using the driven current to interact with MHD modes localized near rational surfaces in tokamaks as well as tasks needing less localization such as the control of the current profile or sustainment of the bulk current.

The ECCD may be calculated in ray tracing codes using typically an adjoint model [90] or the full Fokker–Planck treatment. For an extensive review of relevant Fokker–Planck physics and codes see [91]. Commonly used Fokker–Planck codes include CQL3D [92], BANDIT-3D [84] and the code by Giruzzi [93, 94]. The code calculations may be compared directly with measurements of the driven current to ascertain the validity of the code. The measured current drive may be characterized by the dimensionless current drive efficiency, which includes the expected major dependences on density and temperature, written as [95, 96]

$$\zeta = \frac{e^3}{\varepsilon_0^2}\frac{n_e I_{EC} R}{P_{EC} k T_e} \approx 32.7 \frac{n_{20} I_A R_m}{P_W T_{keV}}, \qquad (19)$$

where n_{20} is the local density in units of $10^{20}\,\mathrm{m}^{-3}$, I_A is the driven current in A, R_m is the major radius in metres, P_W is the power in W and T_{keV} is the local temperature in keV. ECCD

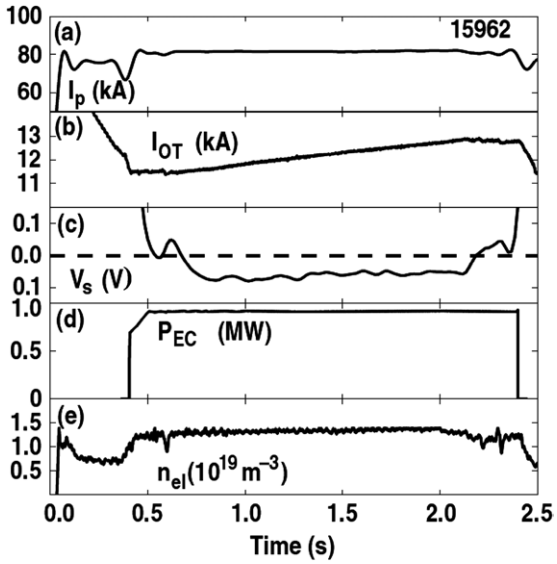

Figure 19. Recharging of the Ohmic transformer on the TCV tokamak, using 1 MW of incident power with the driven current near the plasma centre. The plasma current (I_p), the current in the Ohmic transformer (I_{OT}), the surface loop voltage (V_s), the EC power (P_{EC}) and the line averaged plasma density (n_{el}) are shown. Reprinted from [97].

in a tokamak can be estimated by comparing the loop voltage necessary to sustain the toroidal current with and without the applied EC power. This determination of the driven current is subject to a rather high degree of uncertainty, particularly if MHD activity is present, but it has been used successfully in many experiments. In recent experiments in the TCV tokamak the uncertainty was eliminated by driving a current larger than the total tokamak current for a long time compared with the time for radial relaxation of the toroidal electric field [97]. This reduces the loop voltage to a negative value, recharging the Ohmic heating transformer. When the fully relaxed loop voltage is zero then all of the current is supported by the combination of ECCD and bootstrap current. Data from an example discharge in TCV with ECCD overdrive are shown in figure 19. The loop voltage method can determine the driven current, but it cannot determine the profile of the driven current. The ability to measure the current locally came with the advent of diagnostics, which measure the local magnetic field, such as the motional Stark effect (MSE) diagnostic. The MSE information can be used to determine the width, magnitude and location of the ECCD [59, 96, 98]. An example of this method of determining the ECCD is shown in figure 20. In this discharge from DIII-D [99], the ECCD is localized between two adjacent channels of the MSE system, or about 5 cm. This illustrates the high degree to which ECCD can be localized in actual practice.

Detailed measurements of ECCD on DIII-D show excellent agreement with theory [96], as illustrated in figure 21 for a broad range of conditions of density, temperature and poloidal and radial locations of the ECCD. Figure 21(*b*) shows that the measured minor radius of the peak in the driven current profile is in excellent agreement with that calculated by the TORAY-GA ray tracing code over the entire range of conditions. In addition to the location, the magnitude of the

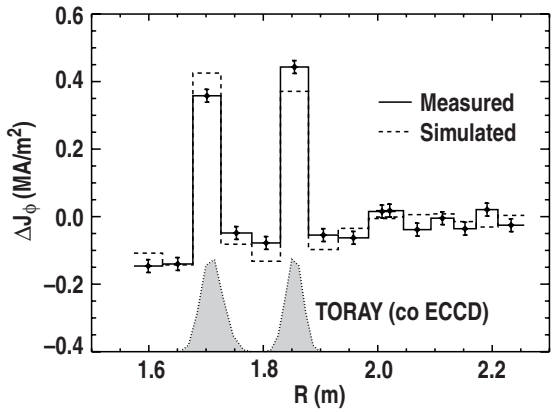

Figure 20. Change in the measured (——) and simulated (- - - -) toroidal current density as a function of major radius between a discharge with co-ECCD and one without EC power, taken from the DIII-D tokamak. Reprinted from [96].

ECCD is also in excellent agreement with the calculations using the quasi-linear CQL3D Fokker–Planck code, as shown in figure 21(*c*) [96]. The fit of the DIII-D measurements of the magnitude of driven current to the calculations of the linear ray tracing code TORAY-GA is not as good as the fit for CQL3D, yet adequate for many purposes, as shown in figure 21(*d*). The quasi-linear model differs from the linear model in that quasi-linear effects on the electron distribution are included in calculating the ECCD, the collision operator conserves momentum in electron–electron collisions and the effects of $E_{||}$ may be included. In the reactor-like plasma of ITER, only the momentum conservation effect is likely to be an important difference.

For current drive in ITER, the fundamental ordinary mode is used with electron temperature in the range 10–25 keV. Measurements of ECCD with this mode in this temperature range have been made on the JT-60U tokamak [40], resulting in a record ECCD current of 0.74 MA and validating the physics model under parameters similar to those of a burning plasma. Data from such an experiment are shown in figure 22. The central temperature reaches 23 keV when 2.3 MW of co-ECCD and 0.6 MW of ECH are applied at a normalized minor radius of 0.17. The measured profile of ECCD is in excellent agreement with that found using the CQL3D code when the effect of the parallel electric field is included [100]. The resistive diffusion time at these high temperatures greatly exceeds the duration of the experiment; so much of the driven current is cancelled by the induced back-emf. Nevertheless, this result represents the largest ECCD driven to date. The traditional figure of merit for current drive $\eta_{\mathrm{ECCD}} = \bar{n}_{\mathrm{e}} I_{\mathrm{ECCD}} R / P_{\mathrm{EC}}$ is $4.2 \times 10^{18}\,\mathrm{A\,W^{-1}\,m^{-2}}$ for this case. Transforming to the conditions of density and Z_{eff} which are expected for ITER, and for a larger parallel index of refraction $n_{||} = 0.8$, the net effect is to increase η_{ECCD} realistically to $0.2 \times 10^{20}\,\mathrm{A\,W^{-1}\,m^{-2}}$ [100]. This is very close to the calculations for ITER made using BANDIT-3D [1].

A benchmarking activity has been in place to compare the different EC codes for validating the predictive capabilities of the codes under plasma conditions which may be present in a burning plasma, using the ITER Scenario 2 equilibrium and kinetic profiles and using 170 GHz waves launched from the top launcher ($R = 6.4848$ m, $Z = 4.11$ m). Codes included to date are shown in table 1. The close agreement of the calculated absorption as a function of the normalized minor radius is shown in figure 23 for the different codes. Note that the largest consistent difference is between codes with weakly relativistic and codes with fully relativistic models of absorption. This close agreement between the fully relativistic models (which should be most accurate in a burning plasma) enhances the confidence in predictions using these codes, given that at least some of the codes have been validated against experiment in today's experimental devices. The largest uncertainty in applying the predictive codes to future experiments in burning plasmas is that the codes have not been compared with ECCD applied at normalized minor radius above 0.5. However, there is no recognized issue arising from theory that would suggest the theoretical models might be significantly modified at larger minor radius. Nevertheless, experimental validation at a large minor radius should be carried out.

4.3.4. Applications of ECH/ECCD. The predictive model and quantitative understanding of the physics can be used to optimize the application of ECH and ECCD for purposes of discharge support and improvement. The uniquely narrow heat and current drive profiles which can be generated by EC waves support some applications which cannot be addressed well by other methods. A highlight of recent work with EC power has been the application of ECH or ECCD to stabilize or otherwise control MHD modes such as sawteeth and neoclassical tearing modes as a means to improve the discharge performance. This work takes full advantage of the very narrow deposition profiles possible with EC waves. The effect of EC power on sawteeth has been extensively studied on TCV [103, 104] and compared [105] with a detailed model using the PRETOR-ST code. This work showed that the sawtooth period could be increased or decreased substantially with modest EC power, but a highly accurate placement of the EC power (within ± 0.03 in ρ) is needed. The modification of sawtooth behaviour has also been studied on the ASDEX Upgrade tokamak, partly as a means of removing the 'seed island' in order to avoid destabilizing the neoclassical tearing mode (NTM) [106].

Several experiments in tokamaks have shown that very significant improvements in plasma performance can indeed accrue from stabilization of neoclassical tearing modes by localized ECCD. Experiments on DIII-D showed that the onset of the mode with poloidal mode number $m = 3$ and toroidal mode number $n = 2$ caused the maximum supportable β to decrease by 25%, while adding ECCD to stabilize that mode allowed β to be increased to 25% above the β of the initial onset [107]. Similar results were reported from ASDEX Upgrade [108] and JT-60U [26]. The more dangerous $m = 2/n = 1$ neoclassical tearing mode, which often leads to locked modes or disruptions, was stabilized consistently in DIII-D [109] and ASDEX Upgrade [110]. The requirement that the ECCD aligns very accurately with the resonant surface for the magnetic islands in these experiments poses a challenge for control systems, since changes in the plasma equilibrium or the kinetic profiles can shift the location where the ECCD is needed. In experiments the location of the ECCD relative to the rational surface has been controlled in real time through control

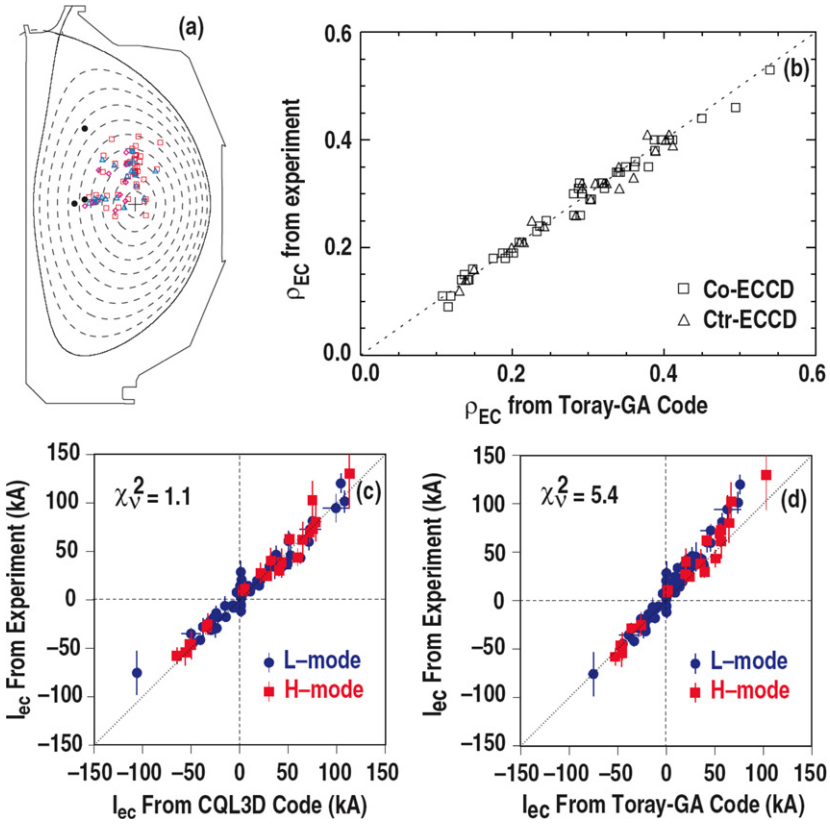

Figure 21. ECCD measurements taken from the DIII-D tokamak. (*a*) Locations of the application of EC power on a plasma cross-section. The square points are for co-ECCD, the triangles are for counter-ECCD and the diamond points are for radial ECH (no current drive). (*b*) The normalized minor radius of the peak of the measured ECCD versus that calculated by TORAY-GA, for all the points of (*a*) except those with radial ECH. (*c*) Comparison of measured ECCD versus that calculated by a quasi-linear Fokker–Planck code including the effects of $E_{||}$. (*d*) Comparison of measured ECCD versus that calculated by a linear ray tracing code. Parts (*a*) and (*b*) are reprinted from [70] and (*c*) and (*d*) are reprinted from [96].

of the toroidal field or the plasma radial position [107] or, more appropriately for a burning plasma, by varying the ECH poloidal launch angle [26]. These results strongly support the use of ECCD in a burning plasma as a means of increasing the plasma pressure to levels which would otherwise be unstable, thereby providing a major improvement in performance.

Modification and control of the current profile has demonstrated the potential to increase the confinement and stability properties in tokamaks. Experiments in DIII-D [111] have shown that off-axis ECCD near $\rho = 0.4$ can sustain high performance plasmas with volume-averaged toroidal β around 3%. The co-ECCD generates negative central magnetic shear, resulting in a weak transport barrier with resulting confinement improvement in the electron, ion and particle transport channels even in ELMy H-mode plasmas. The non-inductive current fraction reaches 90%. Work on JT-60U has shown [112, 113] the maintenance of an electron transport barrier in discharges with high electron heating by a combination of ECH and negative ion based neutral beam heating as a means of simulating the strong electron heating which takes place in a burning plasma. These discharges showed excellent global confinement with 55% of the power heating electrons and $T_e > T_i$.

4.3.5. Summary. In summary, heating and current drive by EC waves is well developed. In addition to its many technical advantages, the application of EC waves is supported by the experimental validation of predictive modelling codes developed from first principles. The development of high power sources has led to the use of EC waves in most toroidal devices, existing and planned. In addition to heating, EC waves have been shown to drive highly localized and robustly controllable currents in plasmas. Detailed measurements of ECCD in present devices show excellent agreement with theory, as embodied in the codes, for a broad range of conditions approaching those of ITER. This has led to demonstrated applications such as current profile control and suppression of MHD instabilities such as sawteeth and neoclassical tearing modes, which in turn have led to improved discharge performance in confinement and stability. The work on MHD suppression has shown that ECCD can be highly localized even in discharges with large sawteeth, ELMs and tearing modes and that even under these conditions the location of the interaction can be well predicted using the available computational tools.

4.4. Lower hybrid current drive

Lower hybrid current drive (LHCD) is an effective technique for non-inductively sustaining and for current profile modification of tokamak plasmas [1]. It has been the subject of theoretical [114], numerical [115–117] and experimental

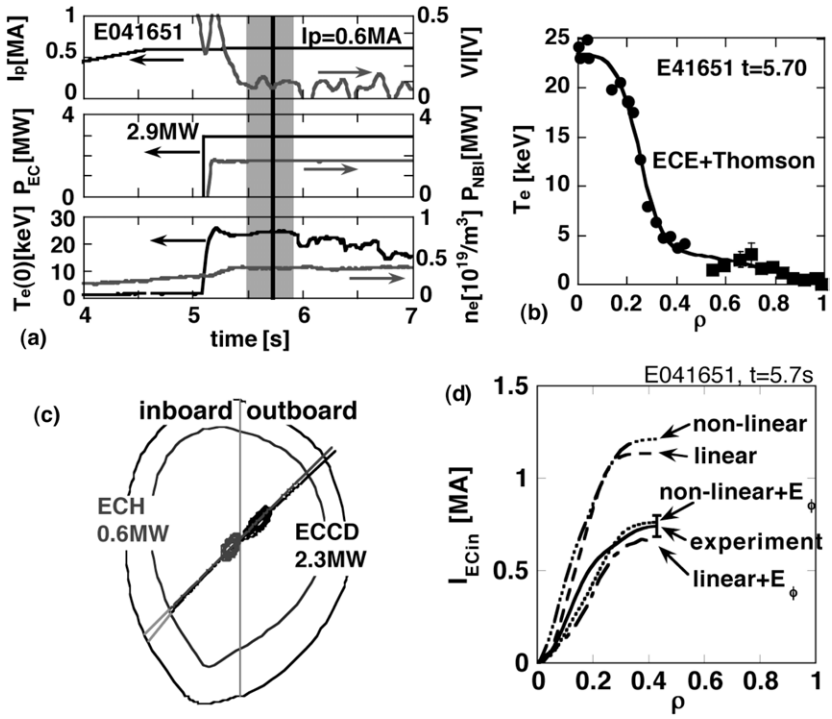

Figure 22. Discharge with 0.74 MA ECCD in JT-60U, (*a*) plasma current and edge loop voltage, ECH and neutral beam power and central electron temperature and line averaged electron density. The current drive is analysed during the time marked by the green shading where the electron temperature is nearly constant. (*b*) Electron temperature profile during the ECCD measured by ECE (circles) and Thomson scattering (squares), as a function of normalized minor radius. (*c*) Deposition location for ECH launched with no toroidal component and for co-ECCD. The vertical line is the cold resonance. (*d*) Radial profiles of EC driven current enclosed in a magnetic surface I_{ECin}. EC driven current obtained by experiment (solid curve) and by various calculations are shown; dashed curve: linear calculation without E_ϕ, dotted–dashed curve: linear calculation with E_ϕ, three-dots–dashed curve: non-linear calculation without E_ϕ, dotted curve: non-linear calculation with E_ϕ. Reprinted from [40, 100].

Table 1. Codes used in the ECH benchmarking. The codes calculate propagation as either an array of independent rays or as a Gaussian beam. The absorption models used are weakly or fully relativistic, and the Fokker–Planck codes use a fully relativistic collision operator. The electron cyclotron current drive calculation uses the models shown.

Code (references in text)	Propagation	Absorption	Current drive
BANDIT-3D	Rays	Fokker–Planck	Fokker–Planck
CQL3D	Rays	Fokker–Planck	Fokker–Planck
ECWGB	Beam	Weakly relativistic	Farina [101]
GENRAY	Rays	Fully relativistic	Cohen [90]
OGRAY	Beam	Fokker–Planck	Fokker–Planck
TORAY-GA	Rays	Fully relativistic	Lin-Liu [102]
TORAY-FOM	Rays	Weakly relativistic	Cohen [90]
TORBEAM	Beam	Weakly relativistic	Cohen [90]

[10, 28, 118,–121] investigations over the past 20 years and has been the subject of numerous reviews [114, 115, 119]. LHCD may be particularly well suited for efficiently driving current off-axis ($r/a \geqslant 0.65$) in reactor grade plasmas. Lower hybrid waves have the property of damping efficiently at high parallel (to $\boldsymbol{B}$) phase velocities ($v_\parallel$) relative to the electron thermal speed, where $v_\parallel \geqslant 2.5 v_{\mathrm{te}}$ and $v_{\mathrm{te}} = (T_{\mathrm{e}}/m_{\mathrm{e}})^{1/2}$. Consequently these waves are better suited than other techniques for driving current in the plasma periphery. Also, owing to their relatively high $v_\parallel$, deleterious effects of particle trapping and parasitic absorption on alpha particles are minimized. Finally the higher phase velocity naturally leads to higher current drive efficiency [114]. Predictions of driven LH current for reactor devices such as ITER using the most advanced ray tracing–Fokker–Planck simulation models available [115] are extremely encouraging (see figure 24). In ITER about 1.6–2.0 MA of current is predicted to be generated at $r/a \geqslant 0.6$ using 30 MW of injected LH source power, for a current drive figure of merit of $\eta_{\mathrm{LH}} = 0.24$–$0.30$ (10^{20} A W^{-1} m^{-2}).

4.4.1. Recent experimental progress. A recent review of the status and capability of RF technology in the lower hybrid range of frequencies (LHRF) can be found in [122]. Sources are typically high power klystrons/gyrotrons in the 1–10 GHz range. Reliable performance has been achieved operating these sources in large numbers. Experiments with powers in the MW range are in operation on FTU, JET, JT-60U, Tore Supra and in the near future on Alcator C-mod. It is also important to note that LHCD is the only technique to date that has experimentally investigated plasmas in nearly steady

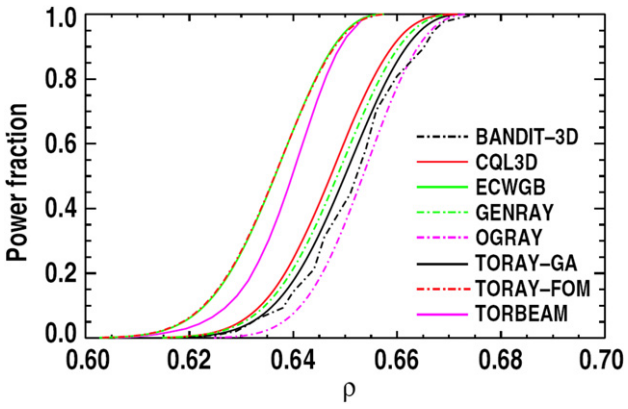

Figure 23. Fraction of incident ECH power which is absorbed, as a function of normalized minor radius for the ITER Scenario 2 equilibrium. The calculations are performed using the codes shown in table 1.

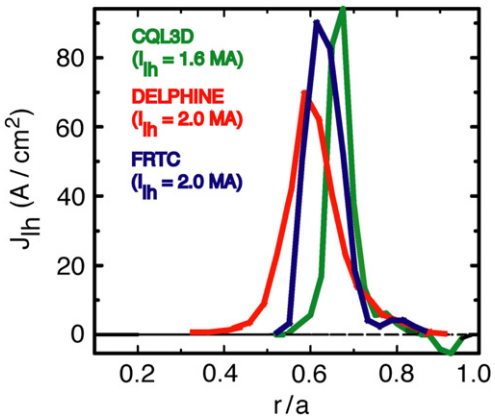

Figure 24. Predictions of LH current density in the ITER-FEAT device ($Q = 5$ Scenario #4) using the combined ray tracing and 2D Fokker–Planck models CQL3D and DELPHINE ($f = 5$ GHz, $P_{\mathrm{LH}}30$ MW). As a comparison a FRTC simulation [342] is shown.

state conditions: a 6 min plasma on Tore Supra [123] as shown in figure 33 (section 5) where a record launched energy has been achieved and a record value of the discharge duration of 5 h and 16 min in TRIAM-1 M reported in [120]. To date, the highest experimental current drive efficiencies have been achieved with LHCD. Values up to 0.34×10^{20} A W^{-1} m^{-2} have been obtained in large machines (JT-60U, JET) and also for ITER-relevant densities (1×10^{20} m^{-3} in FTU [118]).

An important issue has always been the development of techniques to couple to the plasma over the large distance from the last closed flux surface (LCFS) to the first wall ($\geqslant$12 cm) where the launcher will have to be located in ITER. Also, the rapid variations in edge density induced by ELMs could lead to sharp variations in reflected power back from the antenna to the generator. Recent experiments on JT-60U [10] and JET [124, 125] have already demonstrated effective coupling at a distance of 10 cm with encouraging results. In particular, the use of deuterium injection relatively close to the JET launcher ($\sim$0.8 m) has permitted to couple 3 MW of LHCD power during high power NBI and ICRF-heated plasmas with Type I ELMs at 10.5 cm distance between the antenna and the LCFS (figure 25), therefore under conditions very relevant to ITER. Another biggest challenge in LHRF technology

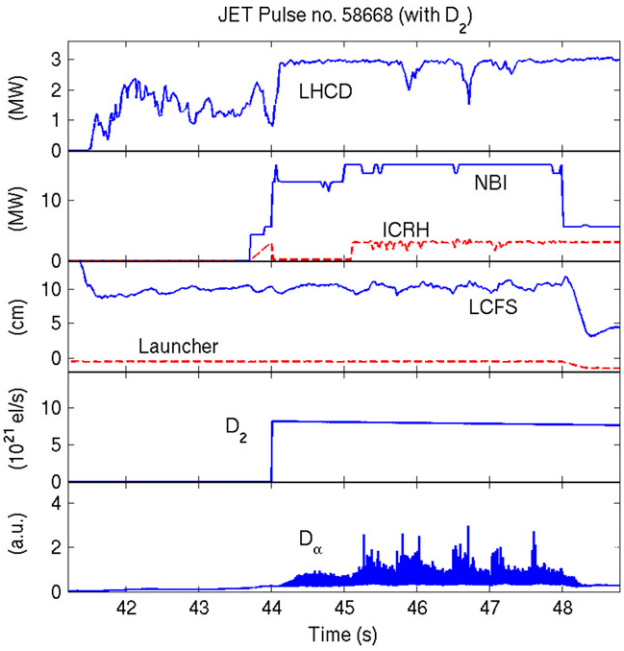

Figure 25. Long distance LH coupling in JET with ELMy plasmas using D_2 puffing during the LHCD phase. Shown are the LHCD power used (P_{LHCD}), the neutral beam power (P_{NBI}) and ICRH power (P_{ICRH}), the distance of the LCFS from the outboard limiters and the distance (negative = behind) of the LHCD launcher compared with the outboard limiters and the amount of deuterium gas fuelling and the measurements of the D_α emission in the divertor.

will be the fabrication of an LH launcher that will survive in a reactor environment. Although such a discussion is not within the scope of this paper, a few points can be mentioned. The present design of the LH wave launcher for ITER is a passive active module (PAM) antenna [126, 127]. Recently, a technological proof of the PAM antenna has been successfully given in FTU, where 250 kW were injected by such an antenna into a plasma with $n_{\mathrm{e,av}} = 0.3 \times 10^{20}$ m^{-3}. LHRF operation on ITER will require sources at 5–5.5 GHz in order to avoid parasitic absorption of LH waves on fusion generated alpha particles [128]. However, this extension in frequency represents only a modest source development effort.

4.4.2. Progress in numerical modelling. Prediction of the profiles of driven current and power deposition from LHCD is the primary goal of numerical modelling. Lower hybrid models typically combine a toroidal ray tracing module for wave propagation with a numerical solution of the Fokker–Planck equation. Ray tracing in the tokamak geometry is necessary in order to accurately predict the evolution of the parallel wave number ($k_\parallel$), which is important for LH wave accessibility, electron Landau damping and current drive. Wave propagation models differ little and are based almost exclusively on cold plasma treatment, warm plasma effects being a minor effect on propagation. Treatments of the absorption and calculations of the driven current profile rely upon solutions to the Fokker–Planck equation. The sophistication of Fokker–Plank models has been varied but has now evolved to full 3D (r, $v_\perp$, $v_\parallel$) simulations [92, 129] which self-consistently treat the pitch angle scattering, the particle trapping and the spatial diffusion in the flux surface

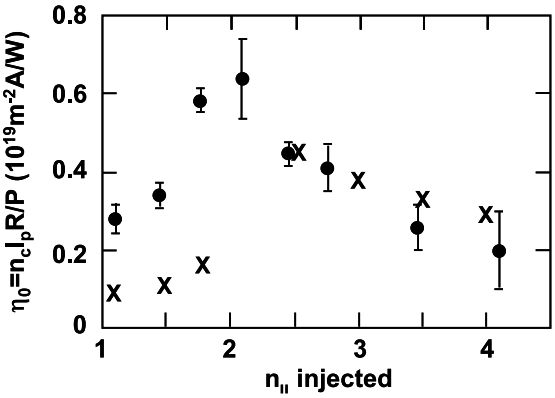

Figure 26. Comparison of experimental and simulated LHCD figure of merit versus $n_{\|\text{injected}}$ in PBX-M. Solid circles are the experimental data and crosses are the simulations. Figures of merit were computed from a combined ray tracing and 2D Fokker–Planck code [130].

geometry. The solution techniques are common to modelling for both LHCD and ECCD and are encapsulated in codes such as CQL3D [92], BANDIT [129] and DELPHINE [117]. With the advent of massively parallel architectures these Fokker–Planck simulation codes can now be run routinely within closed loop transport calculations.

The Fokker–Planck and ray tracing models have been quite successful in reproducing the macroscopic features of LHCD experiments such as the experimentally observed current drive figure of merit defined as $\eta_{\text{CD}} = \langle n_e(10^{20}\,\text{m}^{-3})\rangle I(A) R_0(m)/P_{\text{LH}}(W)$. The LHCD current is typically estimated through a measurement of the loop voltage on the plasma boundary, and then by comparing discharges with and without lower hybrid power. Such a comparison between simulation and experiment was carried out in the PBX-M device [130], the results of which are shown in figure 26. PBX-M was able to individually control the phase of each wave-guide and therefore to well control and measure the $n_\|$ spectrum. As $n_{\|\text{injected}}$ was progressively lowered, the LH waves became inaccessible to the plasma centre. The LH source frequency in these experiments was 4.6 GHz and the density range was $n_{e,\text{av}} = (0.1\text{–}0.3) \times 10^{20}\,\text{m}^{-3}$. The lower magnetic field ($B_0 = 1.53$ T) and higher densities in PBX-M resulted in a higher limit for wave accessibility ($n_{\|\text{acc}} \approx 2.0$). For the example shown in figure 26, a 2D ($p_\|$, $p_\perp$) Fokker–Planck [131] and ray tracing package were used. The agreement between experiment and simulation is good, especially as $n_\|$ is increased from about 2.1 to 4.0. The figure of merit decreases as would be expected with increasing $n_\|$ (decreasing wave phase velocity). When $n_\|$ is lowered below 2.0 however, the observed and simulated η_{CD} decrease even though the incident phase velocity is higher. This occurs because the injected waves become inaccessible to the plasma core at $n_\| < 2.0$. Consequently, the wave absorption is reduced as waves are forced to damp at lower electron temperature.

As the lower hybrid current drive is envisioned as an off-axis current profile control tool in fusion reactor applications, it is important to test our predictive understanding of physics through measurements of the driven current profile and comparisons with theory. The loop voltage method

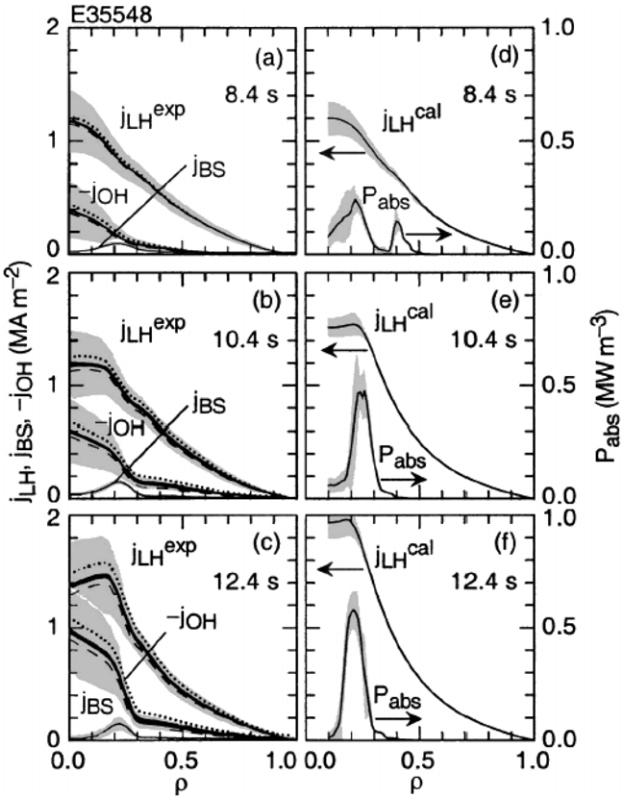

Figure 27. Comparison between LH current profiles measured in JT-60U and the combined ray tracing and Fokker–Planck calculation in ACCOME [33].

described above is only useful for estimating the total driven current; it cannot determine the profile of the driven current. One approach to estimating the driven current profile is by measuring the current profile and the loop voltage profile from sequences of equilibrium reconstructions constrained by internal measurements of the magnetic field [59]. For example, profiles of LH current density have been inferred in an LHCD dominant JT-60U plasma [132]. In this analysis, the total current (J_{TOT}) was inferred from MSE measurements; the bootstrap (J_{BS}) and NB currents (J_{NBI}) were computed numerically [130]. The dc electric field that drives the Ohmic current (J_{OH}) was evaluated from the temporal evolution of the poloidal flux that was obtained from MSE analysis. The LH current (J_{LH}) density was deduced from $J_{\text{LH}} = J_{\text{TOT}} - J_{\text{BS}} - J_{\text{NBI}} - J_{\text{OH}}$. The comparison between the evaluated LH current profile and the combined ray tracing–Fokker–Planck calculation in the ACCOME code [133] shows very good agreement as shown in figure 27.

LHCD simulation models have also been benchmarked against experiment at a more microscopic level. Fast electrons generated in LHCD experiments are characterized by energies that are typically in the range 100–300 keV. Thus, the spatial profile of driven current density is indirectly related to the profile of hard x-ray (HXR) emission from the fast current-carrying electrons. Various physical effects such as a varying q-profile on wave trajectories [117, 134, 135] and spatial diffusion of fast electrons [92, 116, 129, 136–139] can influence the measured profile of HXR emissivity. An interesting set of HXR emission measurements were made

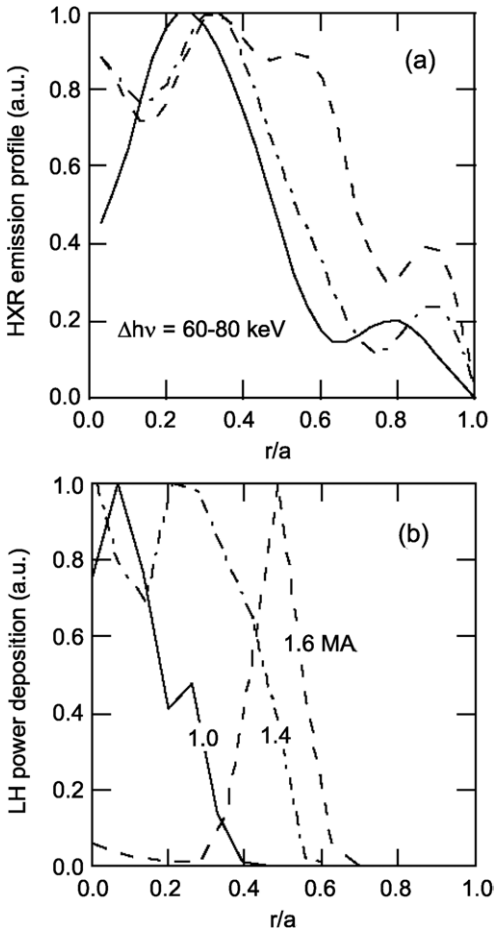

Figure 28. Tore Supra measurements of the HXR profile compared with theory for several q-profiles, showing the importance of the q-profile on the ray trajectories. (*a*) Profiles of hard x-ray emission at three different plasma currents. (*b*) Computed profiles of LH power density at the same three plasma currents.

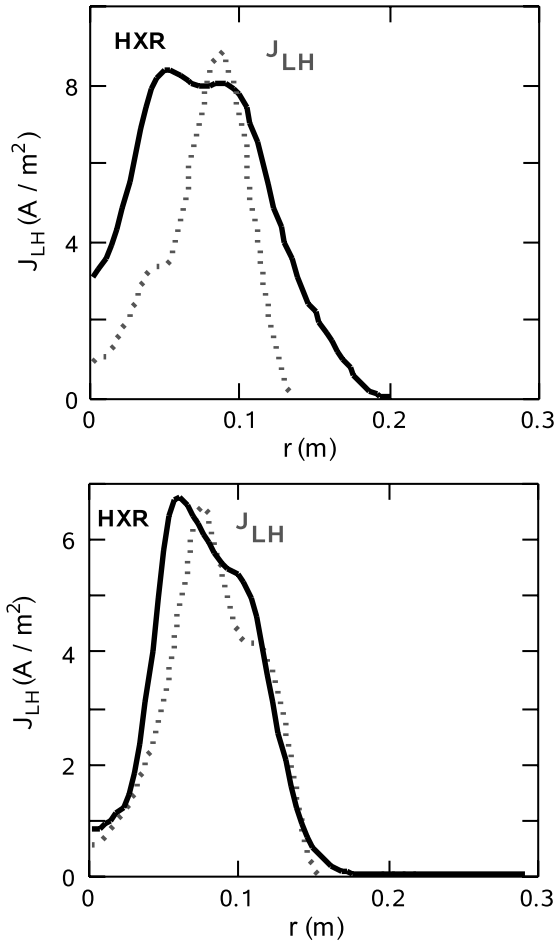

Figure 29. HXR measurement (——) and calculated J_{LH} (- - - -) (*a*) at low density, $n_e = 0.3 \times 10^{19}$ m^{-3} and (*b*) at high density $n_e = 0.6 \times 10^{19}$ m^{-3}, in FTU. Note that the computed J_{LH} assumes no spatial diffusion of the fast electrons.

in the Tore Supra device during LHCD experiments at different plasma currents. The measured emissivity profiles from these experiments and the simulated LH power deposition profiles from a combined ray tracing and 2D Fokker–Planck calculation [117, 134] are shown in figure 28. The source frequency in these experiments was 3.7 GHz with $B_0 = 3.9$ T, $n_e = (1.3\text{–}4.5) \times 10^{19}$ m^{-3} and $n_\parallel = 1.8$. Thus, wave accessibility was quite good in these experiments $n_{\parallel ACC} \approx 1.66$. Figure 28(*a*) clearly shows the HXR profile broadening as the current increases from 1.0 to 1.6 MA. The simulated LH power deposition profiles are roughly in agreement with this experimental trend; the profile peak moves radially outwards as the current increases. A closer examination of the LH ray trajectories in these cases using $(n_\parallel, r)$ phase-space plots (see figure 11 of [134]) reveals that the envelope of wave absorption moves both outwards in radius and upwards in $n_\parallel$ as I_p is increased. Recalling that for an LH wave, toroidal variations in the poloidal mode number m are converted to changes in $k_\parallel$ through the poloidal field, it can be seen that higher values of current (and therefore B_θ) will result in larger variations in $k_\parallel$. Here $k_\parallel = [(m/r)B_\theta + (n/R)B_\phi]/|B|$, where n is the toroidal mode number and B_ϕ is the toroidal component of the magnetic field. The likely consequence of the higher $k_\parallel$ is a radial outward shift in the deposition profile as seen in figure 28(*b*). One important point of disagreement between simulation and experiment is that while the simulated deposition profiles become hollow, the profiles of HXR emission only become broader, remaining flat in the plasma core ($r/a \leqslant 0.6$). This discrepancy could likely be due to the absence of fast electron diffusion effects in the computation of the rf power deposition and current density profiles, which have been shown to cause an inward diffusion of fast electrons, keeping the driven current profile monotonic [137, 138].

Attempts have been made to quantify the transport of fast electrons using numerical Fokker–Planck model treatments [92, 129, 136–138]. In one such study on JET [140], a 2D $(p_\parallel, r)$ solution of the Fokker–Planck equation was obtained using a collision operator with an empirical correction for 2-D effects, a model for $T_\perp(p_\parallel)$ due to pitch angle scattering [138] and a radial diffusion operator. The fast electron diffusivity was taken to have the form $\chi_F = \chi_0\ (p_\parallel/\gamma v_{te})$ with $\chi_0 = 0.5\,\mathrm{m^2\,s^{-1}}$. This model for χ_F assumed that the diffusion of fast electrons was determined by the stochasticity of the confining magnetic field. The simulated electron distribution function was also used to compute profiles of fast electron bremsstrahlung emission that were measured in the experiment. The best fit of the calculated to measured signals

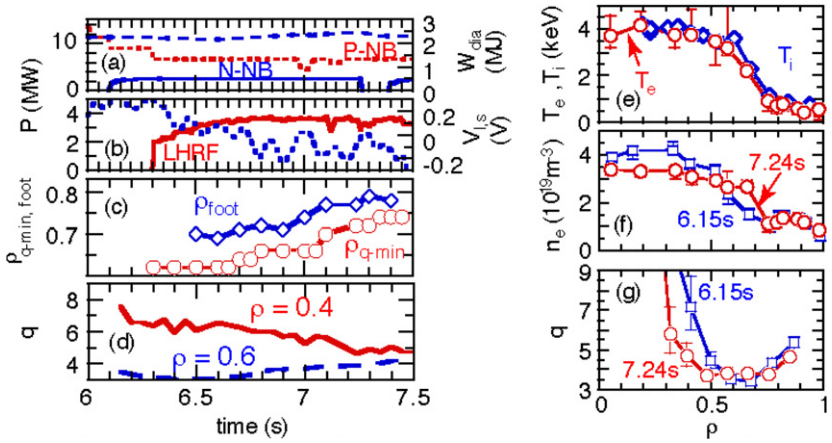

Figure 30. Waveforms of a JT-60U discharge with reversed magnetic shear in the centre and full current drive by LHCD and N-NBCD, obtaining high confinement $H_{98}(y, 2) = 1.4$ at high density (82% of the Greenwald density). (*a*) Plasma current (dashed blue line), power of the negative ion based neutral beam system (N-NB) and positive ion based neutral beam system (PNB). (*b*) The surface loop voltage (dashed blue line) and coupled LHCD power (LHRF). (*c*) The location of the foot of the internal transport barrier (ρ_{foot}) and the location of the minimum q-value (q_{min}). The value of q at $\rho = 0.4$ and $\rho = 0.6$. Changes in (*e*) temperature, (*f*) density and (*g*) safety factor profile without (6.15 s, blue curves) and with LHCD (7.24 s, red curves).

was found for $\chi_0 = 0.5\,\mathrm{m^2\,s^{-1}}$, providing evidence that fast electron diffusion physics was playing an important role in the JET LHCD experiments.

It is expected that fast electron diffusion will become less of a concern as one moves to the reactor regime for several reasons. First, when moving towards high density fast electrons tend to thermalize before they diffuse. As an example, in the LHCD experiment on FTU, the HXR emissivity profile looked broader than the modelled current density profile at low density (see figure 29(*a*)) [116], while at high density the two profiles agreed fairly well (see figure 29(*b*)), indicating that the slowing down process of fast electrons took place on a time scale faster than the radial diffusion time. Second, reduced wave accessibility at higher density requires the use of lower phase velocity waves, resulting in the production of lower energy electrons, which in turn take less time to thermalize. Finally, the fast electron confinement time τ_F should be longer in a larger device since the bulk energy confinement time is longer. Thus, in moving from the regime of present-day experiments to reactor grade plasmas, one moves from LHCD experiments where $\tau_S \approx \tau_F$ to the limit where $\tau_S \ll \tau_F$.

4.4.3. Applications of LHCD. Although LHCD is also used for NTM avoidance and stabilization [141], the main use of LHCD is in the development of advanced scenarios. As the importance of the current profile on plasma performance has been recognized, LHCD has been utilized more in high confinement/performance plasmas. In JET, internal transport barriers can be triggered at low power in plasmas where the q-profile has been optimized with LHCD [142]. In particular, the access to high performance is obtained at low additional power in ITB plasmas with negative magnetic shear. The role of LHCD may be especially significant for maintaining reversed magnetic shear plasmas, since the hollow current profile crucial for the improved confinement can be lost unless sufficient and appropriate off-axis current is supplied. In JT-60U (see figure 30), it was demonstrated that LHCD around the ITB location expanded the ITB radius to keep very high confinement ($H_{98}(y, 2) = 1.4$) and under conditions of a full non-inductive current drive [28].

A number of tokamaks have been using LHCD for access to hybrid regimes characterized by low magnetic shear and $q(0) > 1$ in the core. In Tore Supra [143] and FTU [144], q-profiles of this class have been formed with LHCD. To obtain this regime in JET, the q-profile must be shaped with LHCD before the start of the high power phase, so that it has a flat magnetic shear and $q(0)$ close to unity $q(0) \sim 1$, to avoid sawtooth activity [25]. With a careful and early avoidance of the sawteeth activity, β_N and fusion power can be raised without the detrimental effects of the NTM activity. In Tore Supra, sawtooth activity is avoided in very long pulses (up to 390 s, see figure 33 in section 5) by maintaining the q-profile above unity using LHCD.

4.4.4. Summary. Lower hybrid current drive has proven to be a versatile and highly successful method for driving non-inductive current in a tokamak plasma. The application role of LHCD has evolved over the years, being used initially for maintaining the entire plasma current with zero loop voltage in fully relaxed discharges. More recent applications have involved localized off-axis current generation for controlling sawteeth, neoclassical tearing modes and optimizing reversed shear for improved access to advanced tokamak regimes. Theory and modelling of LHCD experiments is also well developed with toroidal ray tracing being the preferred method for treating wave propagation. Direct numerical 2D ($v_\perp$, $v_\parallel$) and 3D ($v_\perp$, $v_\parallel$, r) codes as well as adjoint techniques have been used successfully to solve the Fokker–Planck equation and self-consistent simulations of LHCD using combined Fokker–Planck and ray tracing modules are routine. Present estimates for the LHCD figure of merit using the most advanced simulation models indicate that $\eta_{CD} \approx 0.24 \times 10^{20}\,\mathrm{A\,W^{-1}\,m^{-2}}$ is possible in ITER at a radial location of $r/a \approx 0.7$. Areas requiring further research include more experiments on long distance coupling, for example, using the PAM launcher

concept. More comparison is also required between measured current density profiles and predicted profiles from Fokker–Planck and ray tracing models. This will help us to validate these models and identify conditions under which spatial diffusion effects on LH driven current profiles are important. Finally, additional synthetic (simulation code generated) diagnostics for hard x-ray emission should be developed in order to diagnose the velocity space and the spatial structure of the perturbed electron distribution in LHCD experiments more accurately. Comparison of the synthetic diagnostic predictions with the experimental measurements should greatly increase the confidence in the simulation models.

4.5. Heating and current drive using ion cyclotron waves

4.5.1. Introduction. Auxiliary plasma heating in the ion cyclotron range of frequencies (ICRF) has long been considered a primary means of heating the core of magnetically confined plasmas to the burning plasma regime. By careful tailoring of the wave frequency and launched spectrum for given plasma conditions, the waves can be used to preferentially heat the bulk ions, a minority ion species or electrons. For more than 30 years, this method has been used to produce high performance plasmas in a wide range of laboratory fusion devices [1]. The culmination of these studies was the demonstration of efficient ICRF heating of deuterium–tritium plasmas in the TFTR and JET tokamaks in the late 1990s [145–147]. More recent studies [148–151] have confirmed the physics basis for ICRF-based scenarios in a wide range of plasma operational regimes that simulate those anticipated in ITER. The use of advanced diagnostics [152–156] combined with the development of sophisticated numerical models [157–163] for wave propagation and absorption has led to an unprecedented level of detailed comparisons between experimental observations and theoretical predictions.

In addition to core plasma heating, fast magnetosonic waves directly launched with ICRF systems or ion Bernstein/ion cyclotron waves excited via mode conversion within the plasma can resonantly interact with and modify the plasma dynamics in a range of potentially important ways. A number of such applications, including non-inductive current drive for control of the plasma stability, were discussed in [1]. More recent studies have indicated that ICRF may provide an effective means of NTM avoidance in standard H-mode regimes in ITER [36, 80, 148, 151, 164], as well as an effective means of central density and impurity control in advanced operational scenarios [12, 165].

The success of all these ICRF-based heating and plasma control techniques depends on the efficiency with which the high power electromagnetic waves can be coupled into the plasma from an external launching structure that is inserted into the plasma vessel. Though significant progress has been made in understanding the processes that constrain the coupled power and spectrum of launched waves [1], a number of substantial issues remain unresolved. In particular, the extent to which RF sheaths, non-linear processes and realistic geometries influence the coupling process remains an area of active research [166–175].

The ICRF systems on ITER and other future fusion reactors may provide important tools for plasma production and wall conditioning, in addition to heating and plasma control applications [1]. Recent experimental studies on JET, TEXTOR, ASDEX Upgrade and HT-7 [176–178] have indicated that ICRF discharge conditioning is more efficient at removing hydrogen isotopes from the walls of the vessel than the glow discharge cleaning techniques, currently in use, or ECRF discharge cleaning with a focused microwave beam. Further studies will be conducted to identify the optimum application of this technique for ITER operations. Excellent summaries of the physics and technology for ICRF applications in ITER can be found in [1], with a more recent review, which discusses in detail the applications of RF to burning plasmas, provided by Gormezano [179]. In the rest of this section, the most significant physics results obtained since the publication of the ITER Physics Basis [1] will be summarized.

4.5.2. Advances in the physics of ICRF heating. The physics basis for a wide range of heating scenarios in deuterium–tritium plasmas was well established with the pioneering studies on the TFTR and JET devices in the 1990s [145–147]. In particular, robust, reliable heating at the second harmonic cyclotron frequency of tritium, with an optional small concentration of co-resonant minority ^{3}He, was demonstrated in these devices, in excellent agreement with theoretical predictions. These results provide a firm basis for selecting second harmonic tritium with co-resonant minority ^{3}He scenarios for core plasma heating in ITER. A numerical 1D study of various ICRF heating and current drive scenarios with the reduced magnetic field and major radius for the latest ITER design supports this conclusion [150]. This numerical study also indicates that fundamental or second harmonic resonance deuterium heating scenarios are likely to be dominated by (parasitic) absorption by beryllium impurity ions and absorption by fusion alpha particles.

Since the end of the D–T experimental campaigns on TFTR and JET, experimental studies have been conducted primarily with either D or ^{4}He majority plasmas, with H or ^{3}He as optional resonant minority species, depending on the rf source frequency. The use of scenarios based on ^{4}He majority plasmas may be particularly relevant for avoiding machine activation during the early operating phase of ITER. Though ^{4}He majority scenarios have been utilized in the past on various machines for similar reasons, a systematic comparison of the heating efficiencies for a range of scenarios based on D or ^{4}He majority plasmas was performed on the JET tokamak [148]. These comparisons demonstrated that while the heating efficiencies are similar in D or ^{4}He majority plasmas, the L–H threshold power is about 65% higher in ^{4}He than in D majority plasmas. Other recent heating studies on a number of tokamaks have focused on the partitioning of power deposition between ions and electrons. In experiments on JET [149], the use of polychromatic—or multiple frequency—waves instead of single frequency waves resulted in less energetic, broader fast ion distributions and subsequently more bulk ion heating, in most parameter regimes. As in earlier experiments [1], direct bulk ion heating was observed to increase as the minority H or ^{3}He concentration was increased to the range of several per cent [148, 180], in agreement with theoretical expectations [181]. At higher minority concentrations, a transition to direct

electron heating via mode conversion of the fast wave to the ion Bernstein or ion cyclotron wave was observed in a number of experiments [148, 156, 182–186], again in keeping with earlier results reviewed in [1]. An important milestone in achieving 'steady state' conditions with auxiliary heating was reached on the LHD stellarator, when world record pulses in excess of 30 min were maintained primarily with ICRF heating in the ^{4}He majority—H minority regime [187], with some assistance from electron cyclotron and neutral beam injection heating. Successful fast wave heating of a high density hydrogen majority plasma at the fundamental hydrogen cyclotron frequency was achieved in LHD. However, it is not clear if the inferred ion absorption was due to the presence of energetic hydrogen ions from beam injection or due to the complicated equilibrium magnetic field geometry of the device [188]. The extent to which mode conversion processes will play a major role in the heating and control of ITER plasmas remains an open question. Previous 1D kinetic simulations along the midplane of an ITER plasma [150, 189] indicated that mode conversion from fast waves to ion Bernstein waves would be negligible, due to the high-density and large plasma size that result in strong absorption and weak tunnelling through the cut-off layer to the mode conversion region. However, for the off-midplane case, significant mode conversion to the ion cyclotron wave was predicted by Perkins, using quasi-local 1D models [190], where the poloidal field can modify the parallel wave number. The co-existence of on-midplane IBW mode conversion and off-axis ICW mode conversion was recently verified in 2D simulations obtained with the advanced full wave solvers, TORIC [156, 162] and AORSA [160], that are discussed in the following paragraph. In mode conversion experiments on Alcator C-Mod in both the D–^{3}He–H and D–H regimes, a mode converted ion cyclotron wave was observed with the new phase contrast imaging experiment [152]. Measured electron power deposition profiles, shown in this reference, obtained with a high resolution electron cyclotron emission diagnostic, are in excellent agreement with numerical simulations from the TORIC 2D full wave code for both on-axis and off-axis mode conversion [156].

A major advance in understanding ICRF heating and mode conversion processes in 2D tokamak plasmas has been achieved by explicitly resolving the mode converted ion Bernstein and ion cyclotron waves in the numerical simulation codes. One approach has been to incorporate ray tracing of the mode converted kinetic waves into the ALCYON full wave solver [191] that provides solutions for the fast waves and starting conditions for the mode converted waves. Good agreement between the measured and calculated electron power deposition profiles in Tore Supra experiments was obtained with this approach. A more general approach is to utilize massively parallel processing to include a fine enough numerical grid to explicitly resolve the short wavelength kinetic modes in the wave equation in either the TORIC code in the finite Larmor radius limit [162] or else the AORSA code in the all-orders treatment [158]. Both these codes are quantitatively consistent with the measured power deposition and mode converted field characteristics in the Alcator C-Mod experiments described above. Recently, the dielectric response models in these codes have been generalized to include the effects of gyrotropic but otherwise general particle velocity space distributions on both wave propagation and absorption [161, 162]. These models will be able to re-evaluate the possibilities for achieving sufficient ion or electron heating via mode conversion for control of the plasma current or localized flow shear in ITER burning plasmas, as will be discussed further in the next section.

In addition to the energetic alpha particles produced by fusion reactions in D–T plasmas, it has been firmly established that ICRF heating scenarios can produce sizeable populations of energetic ions [181, 192–194] that may significantly modify the stability properties of the plasma as well as the heating process itself, increasing the D–T reactivity. Measurements of the spatial profiles and velocity distributions of these fast ion populations have provided a means of verifying the validity of theoretical and numerical models for the wave–plasma interactions for many years. Recent neutral particle analyser (NPA) measurements of the fast ion distributions on JET [154] in the high energy range (0.3 MeV $< E_{\rm fast} <$ 1.5 Mev) and on Alcator C-Mod [155] in high density plasmas (5×10^{19}–8×10^{20} m^{-3}) in a lower energy range ($E_{\rm fast} <$ 20 keV) have also been found to be in agreement with numerical models based on the combined Fokker–Planck and wave heating codes. These numerical models are based on quasi-linear theory, which assumes that successive passes of resonant ions through the cyclotron resonance layers are uncorrelated. However, for sufficiently high energies, the fast ions may exhibit super adiabatic behaviour. Numerical studies with the MOKA code for minority heating scenarios in Tore Supra have shown that this effect [195] can result in a decrease in the power absorption from the waves by very high energy ions. An evaluation of the extent of this effect on alpha absorption of ICRF waves in a variety of regimes in ITER should be undertaken.

As noted in the Tokamak Physics Basis document [1], an rf-induced particle pinch of resonant trapped ions was inferred from modification to the fast-ion-driven Alfvén eigenmode activity and sawtooth dynamics in a JET discharge with H minority heating with an asymmetric toroidal mode number spectrum [196]. Direct measurements of the radial profile of the fast ions in JET during minority ^{3}He heating experiments with the gamma emission profile monitor [153, 197] have verified the existence of this pinch. With counter-current drive phasing, the radial extent of the fast ion profile was 50% wider than with co-current drive phasing. Simulations with the SELFO code [159] indicate that theoretical models for this pinch are consistent with the observations. In these simulation studies, finite orbit effects were retained in solutions of the Fokker–Planck equation for the equilibrium distribution function, but only the fast and shear Alfvén wave polarizations were retained in the corresponding full wave field solver. By controlling the profile of the rf-induced resonant fast ion distribution, it may be possible to optimize plasma stability through the concomitant changes in rf-driven currents [153].

4.5.3. Plasma control applications. The ability to modify equilibrium plasma profiles such as the plasma current, density and rotation through the application of RF waves may play a key role in achieving high performance steady state operation in ITER [1]. As discussed in the IPB [1], fast wave current drive (FWCD) may provide non-inductive control of the central current density, thereby allowing access to stable, advanced

steady state operating scenarios in ITER. According to the 1D numerical study by Van Eester *et al* [150] of various ICRF heating and current drive scenarios with the current magnetic field and major radius for ITER, the predicted FWCD current drive efficiency of approximately $0.02\,\mathrm{A\,W^{-1}}$ in the 41–58 MHz range in the 2nd harmonic T majority–^{3}He minority regime is comparable to the efficiency predicted for the 1998 design of ITER [150]. Recent modelling of the ITER reference ITER scenario #2 with the 3D full wave PSTELION code shows current drive efficiencies of $0.037\,\mathrm{A\,W^{-1}}$ at a frequency $f = 55\,\mathrm{MHz}$ [163]. However, the low frequency window for more efficient FWCD has been constrained to 20 MHz, since the reduced size and field of the current ITER design allows a tritium resonance to be present in the plasma at higher frequencies.

Though the direct electron absorption in large, dense, high temperature plasmas in ITER is predicted to be significant in some frequency regimes, leading to efficient FWCD with directed input spectra, experiments on existing tokamaks are more difficult due to the much smaller predicted direct electron absorption strength. Experiments on DIII-D [99] and JET [198, 199] explored the impact of parasitic ion absorption on FWCD efficiencies. In combined FWCD and NBI heating experiments on DIII-D [99], the measured current drive efficiency was approximately a factor of 2 higher for frequencies when the eighth harmonic deuterium cyclotron resonance was in the device, compared with lower frequencies when the fourth D harmonic was within the plasma. Detailed modelling studies of these experiments indicated that cyclotron damping by the injected energetic ions, which was much stronger at the lower harmonics, was responsible for the observed decrease in FWCD efficiency at the lower frequencies. Otherwise, the DIII-D results followed the theoretical prediction that the FWCD efficiency would increase as T_e increases, with values commensurate with previous experiments [1, 150]. Recent results using high harmonic fast wave current drive on the NSTX device are also consistent with this scaling [200]. FWCD-only experiments on JET in D plasmas with low H concentrations (1–2%) were conducted at a low magnetic field ($B_T \sim 1.7\,\mathrm{T}$) in which the $2\omega_H$ and $4\omega_D$ resonances were inside the plasma [198] for $f_{RF} = 56\,\mathrm{MHz}$. Data from the neutral particle analyser (NPA) detectors indicated that parasitic second harmonic H minority absorption was sufficient to create energetic fast H ions, but no evidence of significant harmonic D majority heating was observed. At twice the magnetic field ($B_T \sim 3.45\,\mathrm{T}$) and lower RF frequency ($f_{RF} = 37\,\mathrm{MHz}$), MSE data indicated that a difference of 300 kA in the central current was obtained between +90° and −90° phasing. However, in related experiments [199] in which pre-heating by lower hybrid waves and additional core heating by NBI resulted in the formation of an internal transport barrier plasma with central T_e of about 8 keV, the per pass absorption on electrons was nevertheless so low (∼1%) that parasitic absorption on resonant residual minority ^{3}He was significant. Less than 50% of the applied ICRF power was absorbed in the plasma, the remainder presumably dissipated in the wall or the antenna structure. Modelling with the SELFO code [199] indicated that only about 15% of the applied ICRF power was absorbed by the electrons, producing non-inductive currents that were consistent with MSE measurements. Furthermore, current diffusion, sawtooth activity and bootstrap current generation in these experiments also influenced the evolution of the central current density. In summary, the low per pass absorption rates on electrons in existing tokamaks render it difficult to conduct conclusive experiments in which significant FWCD is generated. Combined ICRF and ECRF experiments on ASDEX Upgrade and DIII-D could contribute to understanding FWCD physics by exploring the dependence of the current drive efficiency on electron temperature and beta. Additional coordinated theoretical and experimental studies are needed, particularly in some of the candidate steady state scenarios under consideration for ITER, to evaluate prospects for effective FWCD control of ITER plasmas.

While FWCD may provide a means of controlling the central current density, off-axis minority ion current drive (MICD) may provide localized control of the plasma current, thereby controlling the stability of the plasma. The capability of utilizing MICD to control the local q-profile and hence the evolution of sawteeth and other modes was noted in the IPB [1]. An important application of this principle was demonstrated in recent experiments on JET in which localized MICD was used to shorten the period of sawteeth, thereby avoiding monster sawtooth crashes and subsequent growth of neoclassical tearing modes (NTMs) [36, 80, 148, 151, 164]. Since NTMs can be destabilized at lower values of plasma beta than ideal MHD modes, the growth of these non-ideal modes can significantly limit the performance of a fusion plasma. By using localized MICD to destabilize the sawteeth, NTM formation in JET was prevented, leading to the achievement of higher plasma beta in the discharges (see figure 7 in [151]). In burning plasmas in ITER or in future reactors, the energetic alpha-particles produced by the fusion reactions may transiently stabilize sawtooth oscillations, leading to the possibility of monster sawtooth crash events and subsequent destabilization of NTMs. By utilizing localized MICD in burning plasmas for sawtooth destabilization, higher plasma performance may be achieved. Further discussions of the related effects of fast ions on plasma stability can be found in section 4 of this document.

In some enhanced confinement regimes, off-axis heating by RF waves or by NBI leads to the formation of steep density gradients and subsequent strong peaking of the electron density profile and accumulation of impurities in the plasma core. This has been observed in double transport barrier experiments on Alcator C-Mod [165] and advanced scenarios with low central magnetic shear, $q(0) \sim 1$ and $q_{95} \sim 3.3$–4.5, in ASDEX Upgrade [12]. Such density peaking can lead to loss of the enhanced confinement regime, either through violation of stability limits or through excess impurity radiation. The addition of a moderate amount of central ICRF heating in the Alcator C-Mod experiments and central ICRF or ECRF in the ASDEX Upgrade experiments suppressed the central density and impurity accumulation, leading to stable maintenance of these high performance regimes. This method for controlling the central electron and impurity densities may be valuable for exploring steady state enhanced performance scenarios in the non-activated phase ITER. However, the utility of this external density control technique in ITER plasmas with strong central heating from fusion alphas in burning plasma regimes remains to be established.

Because plasma rotation can influence plasma confinement as well as stability, the methods for externally controlling the plasma rotation profile may play a critically important role in achieving high performance steady state burning plasma discharges in ITER and future reactors. In most existing tokamak devices, direct momentum input from neutral beam injection (NBI) has proven to be an effective means of controlling the bulk toroidal rotation of the plasma discharge. However, modelling indicates that NBI will not provide significant momentum input in ITER plasmas [1]. Experiments on JET [201] and on Alcator C-Mod [202] in the late 1990s revealed that the bulk toroidal rotation was present in a number of ICRF-heated discharges, even with a balanced launched wave spectrum so the net direct momentum input was negligible. Subsequent experiments on a number of devices [164, 180, 198, 203, 208] have confirmed that changes in the bulk toroidal rotation, with velocities comparable to those achieved with NBI heating, occur when ICRF heating is applied to a variety of different plasma discharges. However, similar changes in the bulk toroidal rotation have also been observed in Ohmic H-modes [203, 208], implying that the induced rotation is not directly caused by the RF or by rf-driven fast ion effects. Detailed measurements and analysis in JET are consistent with the presence of an underlying toroidal rotation in the co-current direction, not induced by the ICRF, overlaid with co-rotation caused by a torque from rf-induced fast ion effects [164]. Though a number of theoretical models have been proposed to explain the phenomena [164, 209–215], significant discrepancies with the experimental observations have been identified [164, 205, 206, 208]. Because of the potential importance of rotation control in achieving stable, high performance plasmas in ITER, further experimental and theoretical studies will be required to understand and evaluate the potential of ICRF control of plasma rotation.

In the early 1990s, it was suggested that turbulence suppression, leading to enhanced confinement regimes, could be accomplished using externally launched RF waves [216] to drive a localized sheared poloidal flow in the plasma. Over the past 15 years, a number of experiments have explored this possibility, with some success, using directly launched IBW waves [217–221]. The possibility of using the mode converted IBW to provide the sheared flow has been attempted on TFTR [222] and JET [221], with encouraging but inconclusive results. A sheared poloidal flow was observed in TFTR with low field edge D–^{3}He mode conversion, but the available data are too limited to conclusively identify a mode converted IBW as the driver of the rotation. More recently, on JET, a sheared poloidal flow was observed and an increase in confinement time was inferred in high field edge D–^{3}He mode conversion experiments, though again the observations are not conclusive. In neither of these experiments were measurements obtained of the turbulence levels, nor was an extensive, reproducible set of discharges with these features obtained. Detailed 2D full wave studies of the ICW mode conversion process with the AORSA code [160] indicate that significant ion heating and sheared poloidal flow can be driven by the mode converted ICW near the conversion layer and related theoretical studies [223] provide a fundamental picture of the underlying processes. Nevertheless, further experimental and theoretical studies are needed to evaluate the effectiveness of this process in ITER plasmas.

4.5.4. Plasma coupling physics. The success of all of the ICRF-based heating and plasma control techniques discussed in the preceding sections depends on the efficiency with which the high power electromagnetic waves can be coupled into the plasma from an external launching structure that is inserted into the plasma vessel. Though significant progress has been made in understanding the processes that constrain the coupled power and spectrum of launched waves [1], a number of substantial issues remain unresolved. Coupling studies on JET have found that the midplane distance between the last closed flux surface and the antenna has a larger influence on the ability to couple power into the plasma efficiently than does the shape of the plasma [169]. In experiments on Alcator C-Mod, a strong correlation between the measured coupling resistance and the shape of the edge electron density profile was found, which agreed qualitatively with predictions from a relatively simple plasma slab coupling model [173]. ELM fluctuations induce large and rapid variations in the RF impedance on JET, leading to large bursts of reflected power that trip off the RF system, limiting the power that can be delivered to the plasma [168]. A fast data acquisition system has been installed on JET to study these ELM-induced rapid variations in the RF coupling characteristics [224]. Studies of the voltage standoff on the ICRF antennas on ASDEX Upgrade found that high voltage breakdown was correlated with ELM activity [166]. The maximum voltage increased with the number of shots taken, as the antenna conditioning presumably improved. RF sheath formation is believed to be a prime cause for arcing in the antenna structure and other related deleterious edge effects, such as hot spot formation or impurity production [170–172, 225]. The extent to which other non-linear processes, such as parametric decay, affect the coupling efficiency remains uncertain. Recent theoretical studies indicate that turbulent ion heating caused by RF-driven parametric processes in the plasma edge is not sufficient to create the energetic ions observed in the edge regions during some RF heating experiments [226]. However, direct ion heating from parametric decay processes may be responsible for edge ion heating observed during high harmonic fast wave heating experiments on the National Spherical Torus Experiment [227].

Though the existing numerical models for the plasma–antenna coupling processes have had some success in reproducing experimental observations [1], some aspects (non-linear processes, such as parametric decay) of the RF coupling process are not adequately incorporated into the models and are not quantitatively understood. As a result, it has been often been necessary to redesign various parts of the launchers after they have been initially tested in tokamak devices [225, 228]. Though some of the models have recently been improved to include the detailed structure of the launcher [229–231], the models still are unable to include plasma in the immediate vicinity of the launcher or on flux surfaces which can intersect material support structures. Moreover, the plasma is frequently modelled by a 1D plasma slab, connected to the coupling region via plasma surface impedance [1, 229, 232, 233]. Recently developed 3D in-port antennae codes that model the electromagnetic properties of the ITER multi loop antenna (with septum's) in more detail [174, 175] suggest that a significant gain in radiated power may be

possible by utilizing poloidal multi sectioned loop antennae. Improvements in the models, coupled with more extensive *in situ* measurements of the wave fields in the edge regions, will be required to provide more reliable modelling of the ICRF systems for ITER.

4.5.5. Summary. In summary, the physics and technology basis for ICRF heating and current drive methods have been established over 30 years of coordinated experimental and theoretical studies. The demonstration of efficient ICRF heating of deuterium–tritium plasmas in TFTR and JET, coupled with the success of the long pulse steady state ICRF heating experiments in LHD, provide confidence that core ICRF heating can be used to reach burning plasma conditions in ITER. From a technology standpoint, ICRF generators with continuous 1 MW/tube power and related hardware (transmission lines, matching elements, etc) are commercially available, and the ICRF power can be transmitted up to ∼100 m in distance with only a small loss of power. Significant progress in confirming the physics basis for a wide range of ICRF heating and current drive scenarios has been accomplished through the use of advanced diagnostics coupled with sophisticated numerical simulation of ongoing experiments. These studies have demonstrated that dominant power (up to 70%) can be delivered to the majority ions in the second harmonic tritium with co-resonant minority ^{3}He regime in ITER, thereby driving it into the burning plasma regime. The ability to preferentially heat bulk ion, minority ions or electrons by an appropriate choice of the launched frequency and spectrum is a potentially advantageous feature of ICRF heating and current drive methods. Recent studies demonstrate that ICRF may provide the means for current profile control, toroidal plasma rotation generation, and suppression of MHD instabilities that may lead to improved discharge performance in advanced regimes in ITER, but further research is required to establish the viability of these methods. Finally, while core ICRF wave–plasma interactions are well understood, a number of substantial issues remain in understanding the processes that constrain the amount of power and the wave spectra that can be successfully coupled into a tokamak plasma, particularly in the long pulse, high performance plasma anticipated in ITER. Detailed measurements of the wave fields in the plasma edge regions coupled with improved physics content in numerical simulations will be required to develop an integrated model that encompasses the wave launcher, coupling through the edge regions, and heating and current drive processes in the plasma core.

5. Specific control issues to steady state operation

5.1. Parameters to be controlled and measured in steady state

To achieve extended burn with high fusion gain Q in steady state conditions, key physics issues need to be addressed. For the relevant ITER plasma scenario [38, 234, 235], four physics issues can be identified:

- The control of confinement (or H-factor) at sufficiently high density ($n \sim 0.85\, n_G$) to produce the requisite fusion power and Q value. Depending on the scenario, this issue is closely related to the control of the safety factor and pressure profiles.
- The control of power (loss power) and particle exhaust to ensure acceptable levels of helium (or other impurities), plasma impurities and heat load on the divertor target.
- The control of global magnetohydrodynamic (MHD) instabilities (such as neo-classical tearing modes, Alfvén eigenmodes or resistive wall modes) and control techniques to mitigate the effect of disruptions.
- The control of α-particles losses via collective instabilities to enable the transfer of α-particle energy to the thermal plasma.

As a result, the active control of a plasma discharge will require the use of a wide range of real time sensor parameters and appropriate actuators [236]. All control parameters for conventional pulsed operation will also be used in steady state operation. These include the total plasma current, the plasma cross-section and shape, vertical position, the divertor geometry, impurity, core and divertor radiation. This will be essential to establish the required regime and its associated performance to produce the fusion power. Since steady state operation will, in addition, require the optimization of the bootstrap current, the pressure profile (electron and ion density and temperature profiles) has to be actively controlled. As a consequence, the current profile will have to be dynamically controlled, at some particular locations in the plasma, to maintain an internal transport barrier or to avoid possible MHD instabilities (like neoclassical tearing mode or toroidal Alfvén eigenmodes).

In a steady state fusion reactor, all the various physical plasma parameters discussed above will be feedback controlled in a concurrent way (figure 31). The simultaneous control of energy and particle confinement time and exhaust, current density and pressure profiles, heat exhaust and plasma instabilities, all of which having different characteristic delay times of the corresponding actuators. In a tokamak, the characteristic timescales can be ordered as follows:

(i) Instability, micro-instability and disruption growth time.
(ii) Plasma shape and divertor geometry control time.
(iii) Energy and particle confinement time.
(iv) Current profile modification and relaxation time.
(v) Divertor and first wall thermal equilibrium and outgassing time.

The setting up of a real time control networks requires the complete chain of sensors, actuators, communication network and the central controller to relate the plasma parameters to the actuators. Essential for the preparation of the scenarios and for the design and preliminary test of the controller are the simulations of real time control experiments using suitable transport codes like JETTO [237], CRONOS [238] or ASTRA [239].

In the first instance to implement a feedback loop, it is essential to measure or calculate the control parameters directly. Several tokamaks have now developed comprehensive real time measurement networks capable of issuing most of the data required for the control of a steady state discharge. JET [240], Tore Supra [241], JT-60U [242] and DIII-D [243] in particular have built in an integrated way real time data acquisition and processing from diagnostics using fast communication network. The reliability of magnetic measurements has already attracted considerable attention.

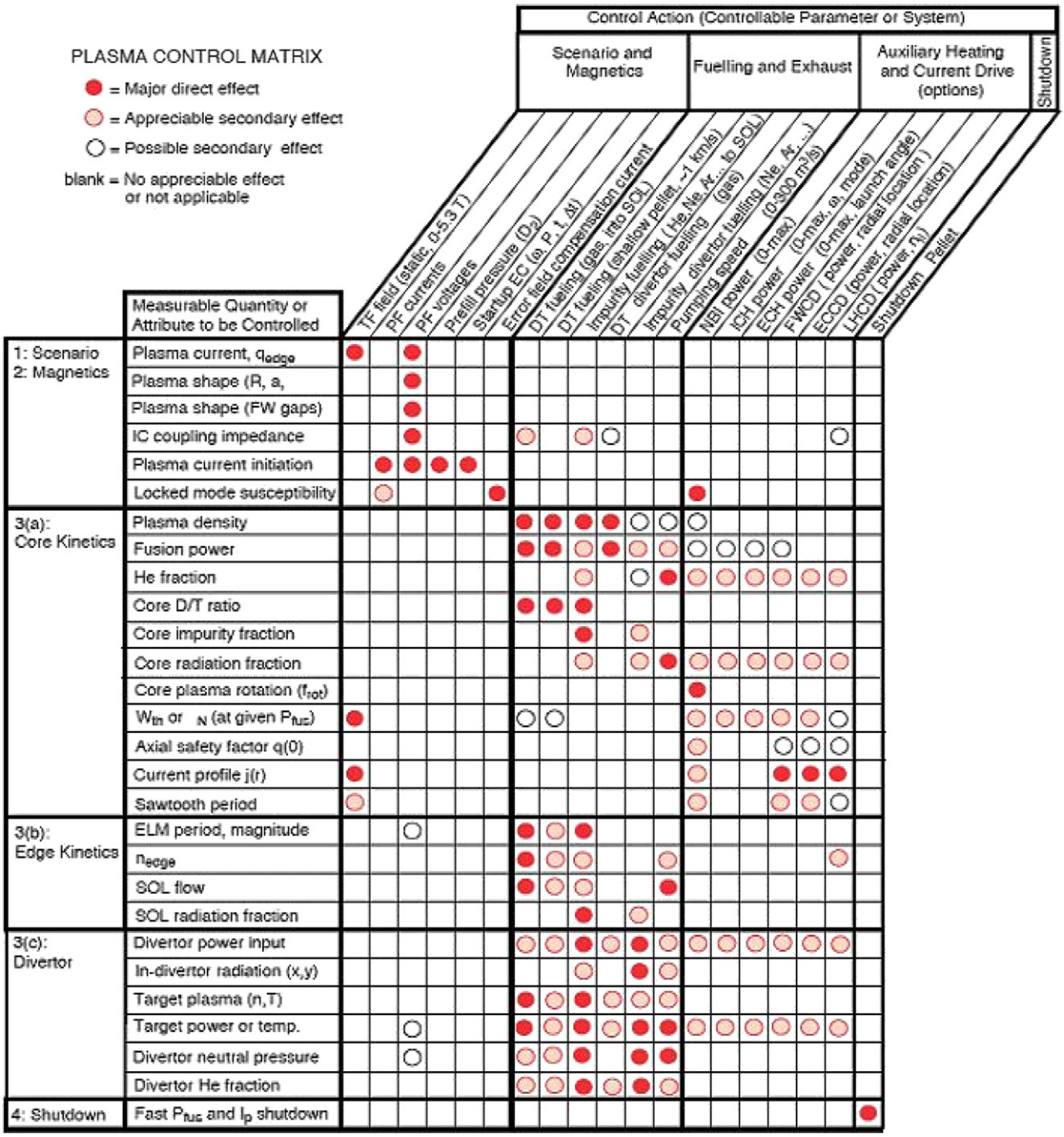

Figure 31. Schematic diagram indicating the range of plasma parameters to be controlled in a fusion reactor and their degree of coupling.

More recently, diagnostic like charge exchange [244] and motional stark effect [245] have produced the ion temperature and toroidal plasma velocity profiles, the pitch angles and the electron temperature profile in real time in several devices. The ECE diagnostic [246] is producing real time temperature profiles on a routine basis in DIII-D, JET and Tore Supra. In these last two devices real time infrared polarimetry is used efficiently in feedback control experiment of the q-profile [247]. Other relevant data such as MHD magnetic signals, neutron signals, heavy impurity lines from x-ray and visible spectroscopy and radiated power from bolometry are complementing this list in most devices. In a steady state reactor, the effects of neutrons or gamma rays may affect electronic equipments, calibrations and detectors. Diagnostic redundancy will be required to avoid the failure of the active control loops. But a major step has now been reached in the architecture of an integrated real time control for the operation of steady state scenarios in present devices.

In addition to real time measurements coming directly from diagnostics, other plasma parameters are also calculated online by dedicated codes because of their relevance to steady state control. For the computation of the current and q-profiles, DIII-D and JET have for example developed real time equilibrium codes EFIT [248] and EQUINOX

[249] capable of integrating internal flux measurement from infrared polarimetry or MSE measurements. The inferred magnetic flux map can also be used to map the kinetic profiles to get the pressure profile. JET has also developed an internal barrier criterion using the data from the ECE diagnostics to calculate the quantity ρ^*_{Te} that should be in excess of 0.014 to detect an ITB [250]. The parameter $\rho^*_{\mathrm{Te}} = \rho_{\mathrm{i}}/L_{\mathrm{Te}}$ (where L_{Te} is the electron temperature gradient length) is inferred from the diamagnetic part of the power balance equation and characterizes the ITB strength using the temperature data. This parameter is now used successfully on other devices such as FTU [144] and TCV [251], and a similar parameter, $\rho_{\mathrm{i}}/L_{\mathrm{p}}$, based on the pressure gradient length, L_{p}, characterizes ITBs on Alcator C-mod [252].

Central controller units are also being upgraded to facilitate the routine use of so-called multi-input multi-output (MIMO) control schemes, which are required for simultaneous current and pressure profile feedback control [253]. The recent improvements in diagnostic reliability and the rapidly growing capabilities of computers and communication networks have recently enhanced the prospect for multi-variable control and the combination of different plasma parameters in control schemes.

All these efforts are ultimately aiming at combining the feedback control of kinetic quantities with the equilibrium shape and position control, which is intimately, related to the core plasma confinement and divertor functions.

5.2. Feedback control of steady state scenario performance using global parameters

Application of single variable control in steady state scenarios. Initially real time control systems were used to control one plasma parameter with one actuator only (see also chapter 8 of this issue [254]). This has been achieved in several ways in a large number of devices for the purpose of maintaining plasma performances during a scenario with an ITB in JET and JT-60. In JT-60 (figure 32), high β_{p} regimes have been sustained for 8 s using the feedback control of the stored energy with the NBI power as actuator [255]. The neutron production rate has been used in JET as an indicator of the core plasma pressure to avoid internal pressure driven kink to trigger a disruption [256]. Numerous examples now exist in DIII-D [243], JT-60U [257] and JET [240] where the control of the plasma performance (stored energy or β_{N}) is realized through the modulation of the additional power.

The effectiveness of feedback control for the purposes of steady state operation has been demonstrated in Tore Supra [241] where long pulse operation used two proportional feedback loops. The first loop controlled the flux on the plasma boundary through the variation of the voltage on the Ohmic power supply while the second loop was controlling the total current by lower hybrid power modulation [258]. Tore Supra experiments have focused on maintaining non-inductive plasma discharges for up to 2 min in the original machine configuration and then up to 6 min in the new CIEL configuration (project CIEL: 'pour Composants Internes Et Limiteur') [259] with 1 GJ of injected energy (figure 33). In each case, the control of the external flux to a constant value

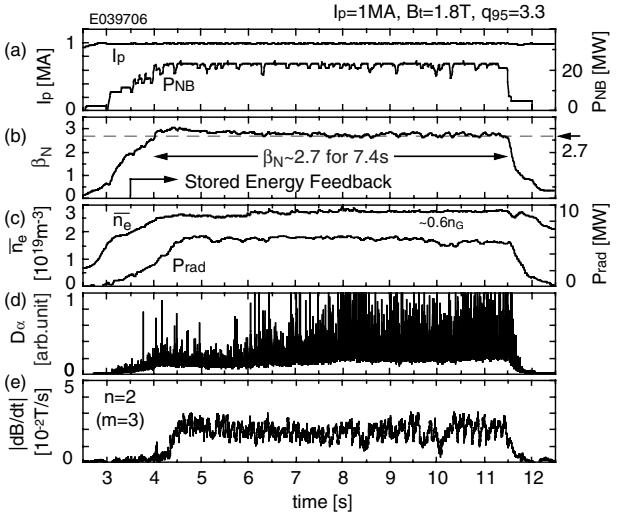

Figure 32. Typical waveforms of a long pulse high β_{p} steady state ELMy H-mode discharge in JT-60U. In this example the stored energy is feedback controlled by using modulation of the neutral beam injection. Shown are plasma current (I_{p}) and neutral beam power (P_{NB}), the normalized beta (β_{N}), reference value used for control, the line averaged electron density (n_{e}) and radiated power (P_{rad}), the D_α emission in the divertor and the strength of the $n = 2$, $m = 3$ activity during the pulse.

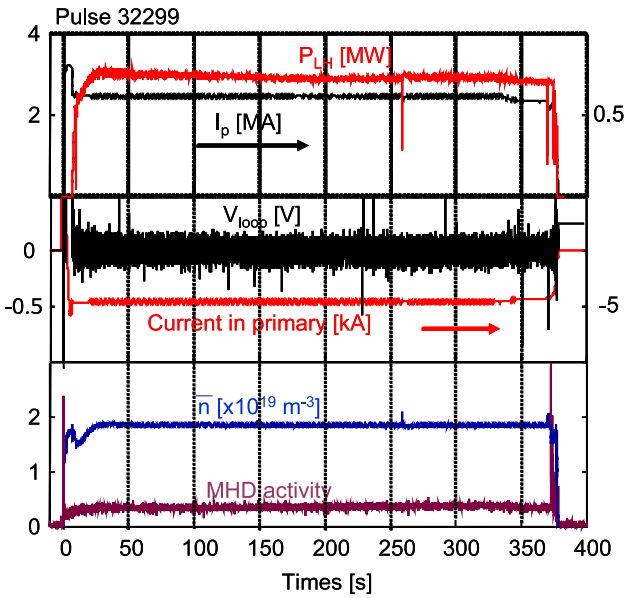

Figure 33. Long steady state discharge (of more than 6 min) achieved in Tore Supra. In this discharge, the plasma current (I_{p}) was controlled by setting the power level of LHCD (P_{LH}). The loop voltage (V_{loop}), the current in the ohmic transformer, line averaged electron density and the level of MHD activity are shown.

has been an essential asset in extending the discharge to long durations. In the last case, the extraction of the energy has been managed by the new toroidal limiter installed in Tore Supra in 2000 and no indication of wall saturation have been observed during this 6 min discharge.

Application of multi-variable control in steady state scenarios. The relationship between a given actuator and a particular parameter we wish to control is seldom straightforward. All

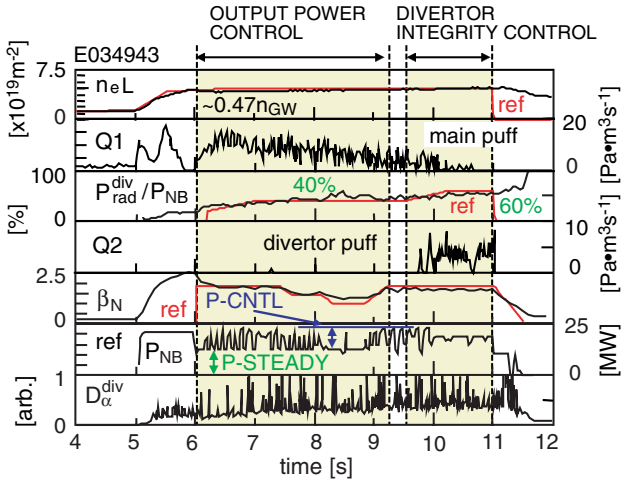

Figure 34. An example from JT-60U of an ELMy H-mode plasma in steady state with simultaneous control of core and divertor plasmas. Shown are the line density (n_{eL}), gas puff rate from main chamber ($Q1$), radiation fraction in the divertor (normalized to the neutral beam power (P_{NB})), gas puffing rate from the divertor ($Q2$), normalized beta (β_N) (feedback controlled), neutral beam power (P_{NB}) and the D_α emission from the divertor.

parameters and actuators are most of the time coupled with each other. For that reason experiments have started using the simultaneous feedback control of multi-variables, also referred to as multi-input multi-output (MIMO) control as defined in chapter 8 of this issue [254].

In JT-60U for example, three major control parameters associated with the fusion reactor instrumentation have been chosen: the operating density, the neutron rate and the divertor radiation power [257]. These parameters are controlled by the gas puffing near the top of the vessel, gas puffing in the divertor region and the NBI power (figure 34). The control algorithm is using a proportional-derivative expression and the matrices are deduced from three different time slices of a single discharge. This scheme has worked successfully for ITER relevant ELMy H-mode plasmas and the contribution of each actuator has been examined in detail.

Following single variable feedback control of radiation in TEXTOR [260] and JT-60U [261], the simultaneous control of the confinement and radiation level has been first achieved in JET on time scales exceeding 6 s [262]. Argon and deuterium puffing have been used as actuator in a dual feedback control of both the enhancement factor $H_{98}(y, 2)$ and the radiation level in high triangularity discharges. The actuators of the feedback control are the deuterium puff rate and the argon-seeding rate. This leads to the highest possible density for a given confinement quality. The feedback scheme uses a 2×2 control matrix, which is calculated from open-loop shots with pre-programmed D and argon puffing and remains valid around a chosen operational condition. This has now resulted in ELMy H-Mode discharges with high performance with the real time feedback controlled quantities ($H_{98}(y, 2) = 1.1$ and $P_{rad}/P_{tot} = 0.63$) being stationary for the whole control phase, $n/n_G \approx 1.1$, $\beta_N > 1.8$ and a constant neutron output. A similar scheme has also been used in DIII-D, where both bolometer measurements and the spectrometer signal for an impurity line have been used as the diagnostic and the puff rate of an impurity gas and divertor cryogenic-pumping of the particle exhaust were used as actuators [263].

Demonstration of intelligent control in steady state scenarios. In the above examples, the feedback controller used is a classic proportional integral derivative (PID) controller in which coefficients are often inferred from a large number of experimental attempts and trial and error. The possibility of adaptive feedback control during which the model of the system is permanently refined and the controller continually adapted to be at a prescribed optimum could be more suitable for the control of steady state discharge than reference set-up points subject to undesired and unpredicted drift of parameters or measurements important for the control process.

The first example of an expert intelligent control in an existing tokamak scenario has been provided on ASDEX Upgrade [264]. In this scheme, the plasma control system has been given the ability to recognize the current operating mode (H-mode or L-mode). In case the H-mode is lost a corrective action is provoked via a modification to the radiation power fraction.

Other techniques such as the so-called 'fuzzy' algorithms [265] are also assessed in steady state scenario simulations.

5.3. Feedback experiments of advanced tokamak scenario using profile control

The control of so-called 'advanced tokamak' regimes for steady state high performance tokamak is regarded as a challenge, in particular, because of the non-linear coupling between the current density and the pressure profile illustrated by the interplay between bootstrap current and pressure profiles (at the formation of an ITB, for example). Therefore adequate plasma control is required to maintain pressure and current profiles at their optimum shape in the operation of a steady regime.

Preliminary feedback control experiments of the current and of the pressure have been achieved separately in several devices. In Tore Supra, initial experiments have achieved the control of the internal inductance through the modulation of the parallel index of the LH wave ($n_\parallel$) [266]. Some attempts have also been made using a single parameter of the q-profile, i.e. the central q-value ($q(0)$). DIII-D experiments have shown that feedback control of the electron temperature at a single off-axis point, using either ECH or neutral beam power as the actuator, can be used to determine the flattop q-profile [267]. In JET, electron temperature profile in ITB discharges has also been controlled in real time using the maximum value of ρ^*_{Te} (see section 5.1) across the plasma radius. In this experiment, the neutron rate is feedback controlled by neutral beam injection in a second feedback loop. With this scheme, the resulting discharge shows already a significant improvement in the stationary behaviour with respect to similar discharges without feedback control [268], shown in figure 35.

There is in general no method to take into account non-linearities in the design of controllers except the use of the linear response theory around an equilibrium point. For real time q-profile control experiments with LHCD, NBI and ICRH powers as actuators, the method used at JET is to build a linear Laplace response model around the target state to be controlled [269]. The static transfer matrix can be determined

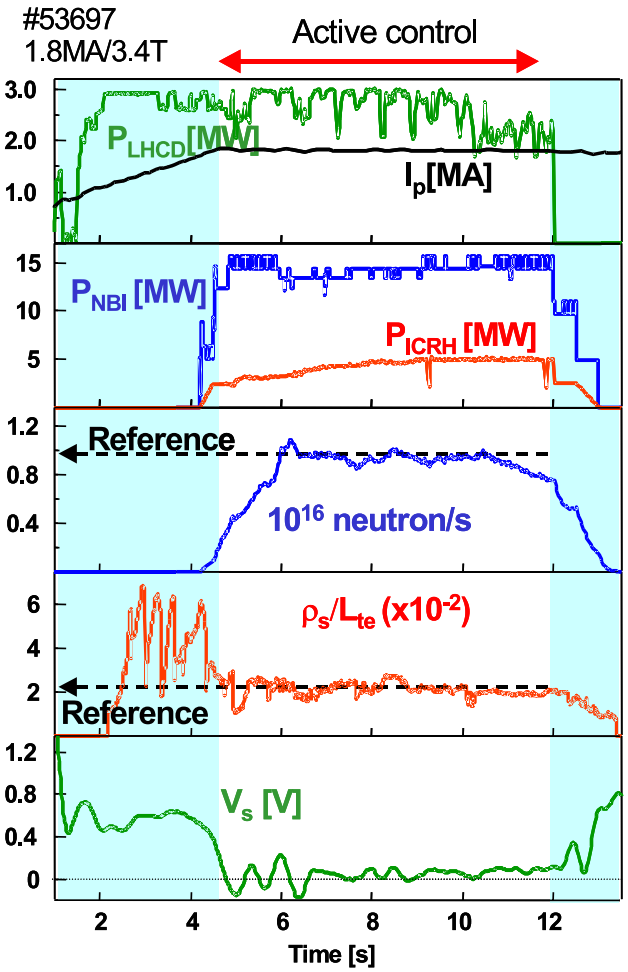

Figure 35. Active control of an internal transport barrier in JET using the feedback control of the ρ^*_{Te} criterion with ICRH and the feedback control of the neutron rate with the neutral beam power. Shown are LHCD power (P_{LHCD}) and plasma current (I_p), the neutral beam power (P_{NBI}) and ICRH power (P_{ICRH}), the D–D neutron rate with the reference value used, the value for ρ^*_{Te} with the reference value used and surface loop voltage (V_s).

experimentally using step or modulation experiments of the actuators. In this procedure each actuator is stepped up or down in three different pulses and the input power and output differences are measured in their steady state limit after about one resistive time. This experiment is repeated for all the actuators. The transfer matrix can also be found from a state space model of the plasma, which also linearly describes the plasma evolution around its reference state.

As a proof of principle, this procedure has been first applied to the control of a pre-defined q-profile of 5 points ($r/a = 0.2; 0.4; 0.5; 0.6; 0.8$) with one actuator only, namely the total LH power [270]. In this case, the accessible targets are of course reduced to one family of profiles, so the reference points have been chosen close to the family inferred from the singular value decomposition (SVD) analysis. The experiment is performed during an extended LHCD phase of 15 s similar to those used to pre-form the q-profile for the creation of an ITB ($I_p = 1.3$ MA, $B_T = 3$ T, $n = 2.5 \times 10^{19}$ m^{-3}). The transfer matrix of the controller is calculated from a simple LH power step experiment. This matrix in this case has a size of [5 × 1]. The q-profile reaches steady state and is maintained for about two resistive times. The LH-deposition profile calculated by the ray tracing code DELPHINE [117] included in CRONOS is consistent with the gains of the control matrix; the maximum in the calculated power deposition for LHCD is at $r/a = 0.5$, the maximum in gain for the experimentally determined control matrix is also at mid-radius. With this technique, reversed shear q-profiles are also accessible and have also been achieved in steady state conditions by changing the reference value of the q-profile [240, 270].

After this first encouraging result, this model-based technique has been applied to the q-profile control during the high power heating phase of the plasma pulses, using three actuators (i.e. LHCD, NBI and ICRH) [269]. This time, the steady state plasma response is determined from one reference discharge and three dedicated step down experiments (one for each actuator). The controller transfer matrix is in this case a [5 × 3] matrix. Figure 36(*a*) shows the resulting feedback waveforms together with the demand produced by the controller and the time trace of q at $r/a = 0.4$. Figure 36(*b*) illustrates the evolution of the q-profile during the controlled phase (from 7 to 13 s). Between 7 and 11 s, the value for q inside $r/a = 0.5$ falls sharply and then rises after 11 s towards the reference points as the actuators start to act on the current density diffusion. This demonstrates that the selected gains were adequate and the technique effective on a time scale that approaches the current diffusion time scale. The non-inductive current components generated by the three actuators at 11 s have been calculated by the JETTO code. The radial deposition of these non-inductive currents (mostly LHCD at mid-radius and NBCD in the plasma core) indicates that two independent combinations of the actuators acting in two complementary plasma regions effectively control the q-profile. This is consistent with the results from the SVD analysis of the transfer matrix indicating that the accessible q-profile targets are basically restricted to a two-parameter profile family, the third component having little influence. This successful experiment represents a step forward in view of a future application combining the q and pressure profile as an input in the controller.

During the recent high power experimental campaign in JET, experiments have been conducted achieving for the first time the simultaneous control of the current density and electron temperature profiles in ITB plasmas. The distributed-parameter version of the algorithm was implemented using three actuators (LHCD, NBI and ICRH), and eight output parameters. The profiles are projected upon five cubic-spline basis functions for the inverse safety factor, $\iota(r)$, and three piecewise-linear functions for the normalized electron temperature gradient profile, $\rho^*_{Te}(r)$. Real-time control was applied during 7 s in a discharge at 3 T/1.7 MA, and allowed different target q-profiles—from monotonic to reversed shear ones—to be reached while simultaneously controlling the profile of the electron temperature gradient. As shown in [269, 271], the controller was designed to minimize, in the integral least square sense, the distance between the target $\iota = 1/q$ and ρ^*_{Te} profiles and their respective real-time measurements (figure 37). The requested power has also been achieved and stayed within the operational limits of the plant. The response of the controller has also been simulated

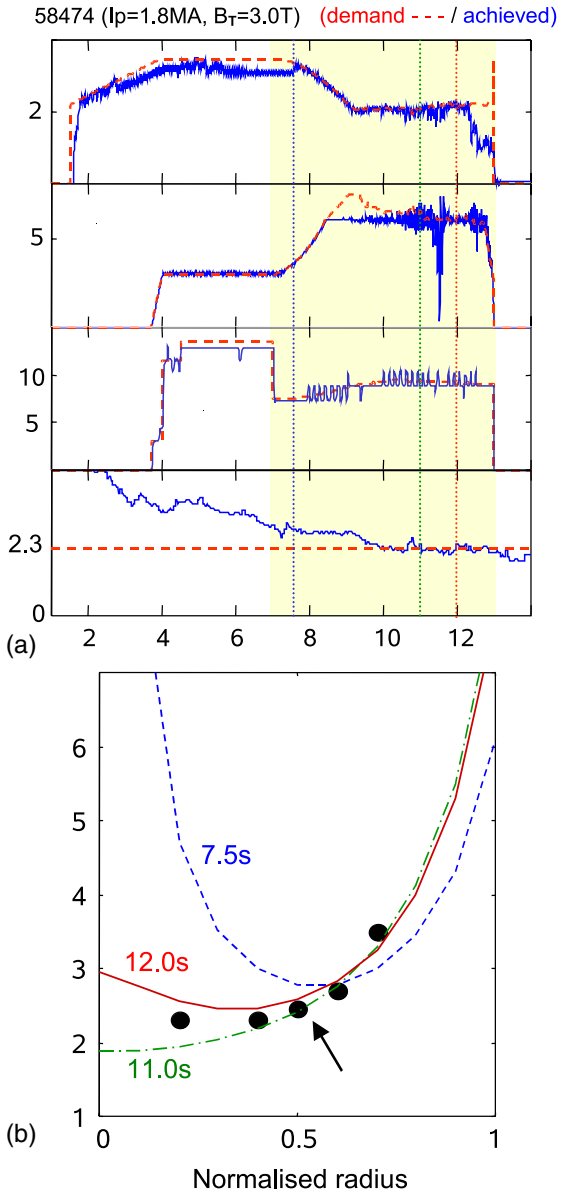

Figure 36. (*a*) Real time control of the q-profile in JET with three actuators (LHCD, ICRH, NBI). The powers demanded by the controller (dashed lines) are compared with the delivered power from the heating systems in the three top graphs. The q evolution at $r/a = 0.4$ (bottom trace) reaches its reference value at 10 s and keeps around it for about 3 s. (*b*) The q-profile evolution in JET at 7.5, 11 and 12 s during the control phase of pulse 58474. The filled circles indicate the reference values. The q-profile reaches the references at 12 s after about one resistive time.

over longer time scales using the JETTO transport code. Comparisons with the actual experiments are qualitatively satisfactory [272].

5.4. Integrated control of a burning steady state scenario

Although various control issues for steady state scenarios are now tackled successfully by experiments today, it should be emphasized that the route to a fully controlled and integrated ITER-relevant scenario still requires a sustained research effort. From of this overview, several challenging issues can be identified for future experiments.

As mentioned in section 5.1, current and pressure profiles require active control in a dynamic way. From its initial phase to maximum performance, steady state scenario control requires the use of several strategies for controlling the profiles. Actuators will also change and be different whether the discharge is in the low or high β_N phase. Therefore, the maximum demands on these actuators need to be known and preferably minimized in the objective of reducing the cost of the device. Since steady state ITER scenarios are still under development, it is still uncertain which margins are needed. Continuous efforts in modelling control experiments should also contribute to the definition of actuator margins. Furthermore, the different and sometimes concurrent controls for the production of a steady state scenario need to be integrated and compatible. For instance, current profile control together with shape control, RWM control (an example is given in figure 38) and ITB control need to be demonstrated simultaneously to validate the operation procedure of a steady state scenario with high bootstrap fraction. Similarly, for the hybrid scenario, the simultaneous control of the q-profile above unity together with ELM control (figure 39), pressure control close to wall limit and NTM control must be demonstrated.

In addition, in a steady state reactor plasma, burn control will certainly become an important component of fusion research. Theoretical analyses have already attempted to simulate the ignition access and the operation of an ignited plasma [273] to determine the ignition boundary of a steady state fusion reactor. The simulation demonstrates the fusion power regulation by feedback control of the fuelling and auxiliary heating power.

Real time experiments have been carried out in JET to simulate the dynamics of a self-heated tokamak plasma [274]. The principle of the experiment is to use the additional heating systems to simulate alpha-particle heating under real time control. In this scheme, a component of the heating may be varied in direct response to plasma measurements (such as DD reaction rate); this represents the 'self-heating' effect. Another component plays the role of auxiliary heating and may either be simply pre-programmed or controlled in a feedback loop to achieve a given plasma performance. Depending on the scaling of the simulated alpha heating power, the ratio of 'self-heating' to 'auxiliary heating' determines the effective fusion amplification factor Q. This experiment demonstrated that the occurrence of the H-mode transition mainly determined the evolution of the simulated alpha power and Q. Applying feedback acting on the auxiliary heating component (ICRH) successfully controlled the simulated alpha power.

6. Simulation of ITER steady state and hybrid scenarios

6.1. Introduction

Simulation of tokamak scenarios requires a high level of physics models integration. In the particular case of advanced tokamak scenarios, such simulations involve the link between the plasma current profile and the heat and particle transport as a key element and thus require developing at least time-dependent simulations of several coupled plasma profiles, self-consistently with the magnetic equilibrium evolution.

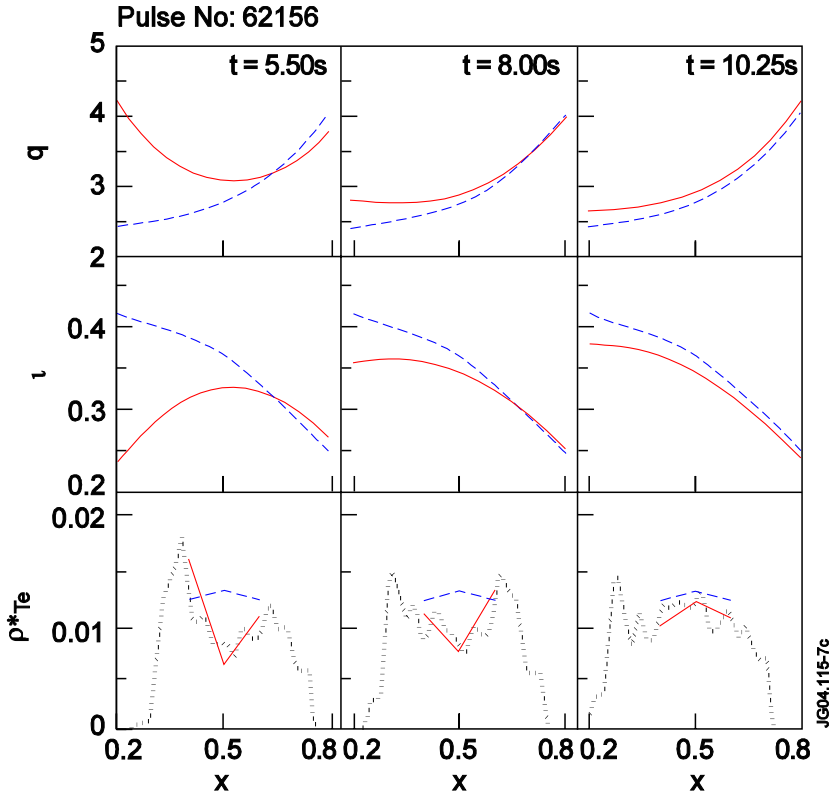

Figure 37. Measured (solid red) and target profiles (dashed blue) for q and ρ^*_{Te} after projection on a set of basis functions for pulse 62527 in JET. The controller manages to get the profiles close to the target in about 6 s.

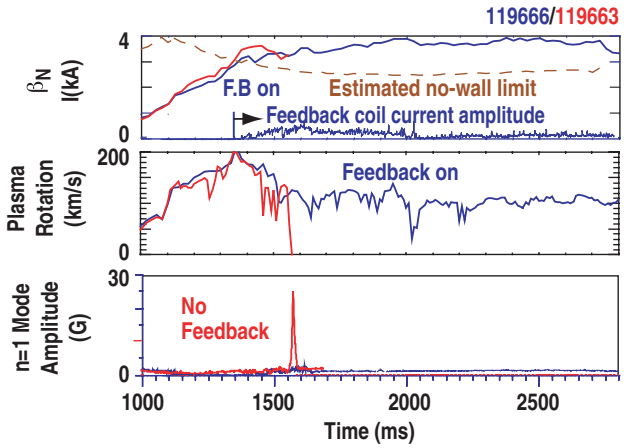

Figure 38. Active wall mode stabilization using 12 internal coils in $n = 1$ symmetry for operation above the no-wall limit in DIII-D for about 200 growth time. Two discharges are given: 119666 (with feedback on) in blue and 119663 in red (no feedback). Shown are the normalized beta (β_{N}), coil current amplitude, the plasma rotation speed and the amplitude of the $n = 1$ mode activity.

The typical duration of such simulations must reach at least several current diffusion times or even longer when erosion processes on targets and first wall are addressed. However, the characteristic time step of the simulation is in the order of the energy confinement time, or much less when MHD stability issues are examined. Note that the latter is often the case as such scenarios are devoted to high beta operation of tokamaks, as close as possible to the limits. Many recent modelling initiatives now address such challenging predictive simulations for ITER steady state and/or hybrid scenarios. However, the present understanding of heat and particle transport still does not allow such simulations to be fully based on first principles. They thus need detailed comparisons with existing advanced tokamak experiments from which a certain level of ad-hoc models or assumptions are derived. In addition the simulations contain a significant level of prescribed profile behaviours: for instance the plasma current and temperature profiles are predicted in simulations where the density profile is assumed, or vice-versa. This particular modelling activity is presently not in a position to provide definitive quantitative conclusions about advanced modes of ITER operation, and in particular any definite conclusions on the adequacy with the ITER heating and current drive (H&CD) sources. However, many recent results, as reported in this paper, show a significant progress in both directions of interpretative simulations of existing advanced tokamak discharges and of predictive simulations of ITER steady state and hybrid scenarios, and thus an increase of the level of understanding and confidence in our predictive capability.

In this section a general presentation of the main simulation codes will be given, with emphasis on the current profile simulation tools (section 6.2). The main discussion on transport issues is given in chapter 2 of this issue [17]. Benchmarking of these codes on existing experiments is then briefly presented (6.3). Simulations of the achievable current profile for ITER steady state (SS) scenarios will be presented (section 6.4) followed by conclusions on the present status of steady state scenario simulation (in section 6.5).

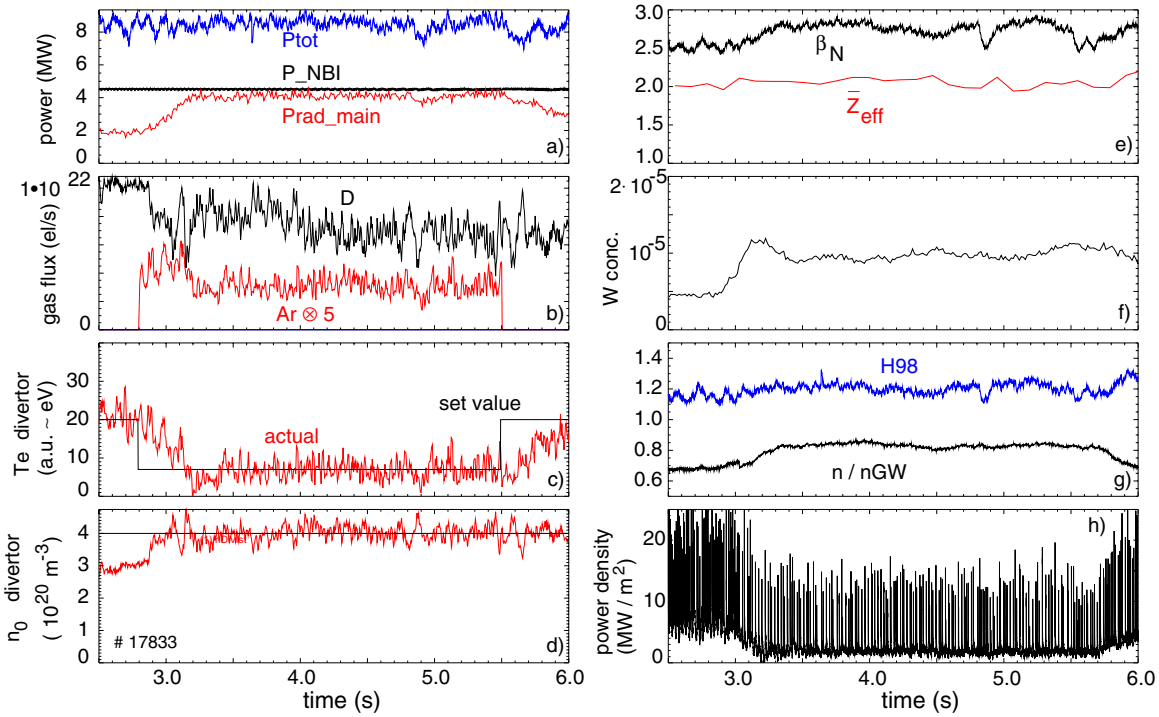

Figure 39. Integrated exhaust scenario controlling radiative power, inter-ELM power and particle removal rate in AXDEX Upgrade [343]. (*a*) The total input power ($P_{\rm tot}$), neutral beam power (P_NBI) and radiation from the main chamber (Prad_main). (*b*) The deuterium gas flux (D) and Argon gas flux (Ar). (*c*) The measured divertor temperature (red) with the reference value for control (black). (*d*) The neutral pressure in the divertor (n_0,div). (*e*) The normalized beta ($\beta_{\rm N}$) and effective charge ($Z_{\rm eff}$). (*f*) The measured central tungsten concentration (W). (*g*) The energy confinement scaling factor $H_{98}(y, 2)$ and the line averaged electron density normalized to the Greenwald density (n/nGW). (*h*) The measured peak power density on the outer divertor target plate from thermography.

6.2. General description of numerical tools and common issues

Simulation codes generally privileges modularity and flexibility in order to accommodate future development of physics input on various aspects: for example for transport, heating and current drive modules. Interactivity is also an important aspect of steady state simulation as many of the scenarios simulated are exploratory. This is already used in some codes (ASTRA, Corsica).

Automated system for transport analysis (ASTRA) [275] is a flexible programming system capable of creating numerical codes for predictive or interpretative transport modelling, for stability analysis or for processing experimental data. The option of running ASTRA interactively enables to control and assess the scenario during the run without pre-programming. The ASTRA system has a modular structure and comprises an extensive library of modules describing different physical processes and data treatment. The possibility of the variation of the problem description level even in every single run independently on the discharge phase is extremely convenient in the case of the integrated modelling of the steady state scenario with multiple time scales for different processes. For example for the major part of transport calculations the extremely fast 3-momentum equilibrium solver can be used [276]. During the simulations of the SS scenario at the phase where the MHD limits are approached the fine details in scale lengths of the profiles can become important for stability analysis. In this phase of simulations the equilibrium solver is switched to more time consuming arbitrary shape solver [277] and transport calculations are temporarily interrupted for MHD stability analysis by stand-alone code KINX2000 [278]. The NBI solver [279] is also switched from the time-dependent Fokker–Planck solver to the analytical SS option after the relaxation of the fast NBI particles distribution. To reduce further the computational time we use also so called ITER simulators: modules that reflect the dynamics and parametric dependences obtained with comprehensive modules in the range of expected ITER parameters. Such simulators for ITER are used, for example, for ECCD simulation (ECZV based on ORGAY code [89] parameterisation for ITER) and boundary conditions and neutral particle sources (B2EIT based on B2-Eirene [280] calculations).

CRONOS [238] is a diffusion equation solver that computes the temperature (ion and electron), density (any species) and plasma parallel electric field profiles, self-consistently with the 2D fixed-boundary equilibrium (any shape) and the external heat, particle, and current drive sources. Non-diagonal terms in the transport matrix can be included on demand. A fully modular architecture allows plugging in any ad hoc or first principle model of heat or particle transport, including internal links with plasma current or plasma rotation profiles, any source term or any feedback control loop. CRONOS is also coupled to an MHD stability package, and runs the neoclassical NCLASS module [281]. In parallel, it contains a complete zero D package, used as help for decision and/or benchmark of the full simulations. The code is coupled with widely used first principles transport models, like GLF23 [282] and the Weiland model [283]. Among the

recent developments on CRONOS for ITER, one can underline the numerical optimization of the NBI package (SINBAD) for high energy injected ions, or the development of a Monte-Carlo module (SPOT, [284]) able to better compute the orbit effects on the fast ions and alpha-particle behaviour and (later) their interactions with injected waves.

ONETWO [285] is a 1.5D transport code for electron and ion temperatures, densities (of any species), toroidal rotation velocity and poloidal magnetic field, solving self-consistently with the fixed-boundary equilibrium (of any shape) and the external heat, particle, toroidal momentum and current sources. The code is used both as an analysis as well as a predictive tool supporting the experimental and theoretical studies. As an analysis code, it is equipped with a comprehensive set of heating and current drive source models. The unshielded neutral beam current can be modelled in two ways, using either NFREYA [286] with an analytical Fokker–Planck model [287] or NUBEAM with a Monte Carlo slowing down model [288]. The RF current drive models primarily rely on the ray tracing codes TORAY-GA [102] for ECCD and CURRAY for FWCD [289] and LHCD [290]. The transport models used in the code include first principle transport models as well as experimental and empirical models. Recently the theory-based GLF23 model [282] has had success in modelling experimental data with externally calculated sources and sinks in the XPTOR code [291]. The latest GLF23 model has been incorporated in ONETWO, and benchmarked with the XPTOR code. A computational advance recently incorporated in this code is the use of globally convergent non-linear solution methods, based on a combination of steepest descent and modified Newton methods. The method is applied both to the time-dependent and time-independent (steady state) version of the finite difference form of the coupled set of transport equations. The time independent version is of particular value for modelling the steady state behaviour of current driven plasmas due to the long parallel electric field equilibration time.

Corsica [292] is an axisymmetric 2D-equilibrium plus 1D-transport predictive simulation and analysis code. Current profile evolution is obtained from flux diffusion self-consistently with equilibrium and transport using Ohm's law and models for thermal and particle transport coefficients, and heating, fuelling and current drive sources. The equilibrium is converged at each time step simultaneously with transport and sources using time stepping that is specifiable in the range from centred to fully implicit. The code has built-in modules for stability analysis including vertical stability, simulated experimental diagnostics and poloidal-field-coil (PF) diagnostics (e.g. current and superconductor limits). It is equipped with a friendly user interface for highly flexible run-time problem specification. A variety of equilibrium solution methods are available including free- and fixed-boundary using direct or inverse solution techniques. This free-boundary solver (previously known as TEQ) was extensively used during the ITER CDA and EDA [293]. In the free-boundary mode, solutions are fully coupled to the external circuits with the coil configurations. This allows operation [294] in the free-boundary mode using Ohm's law either in conjunction with shape controllers or with passive or prescribed PF coil currents. Alternatively, shape control can be varied using a sequence of pre-defined boundaries with the resulting self-consistent PF coil currents calculated.

Corsica has a variety of energy, particle and angular momentum transport modules including GLF23 [294], IFS/PPPL [295], RLW [296], Coppi–Tang L-mode [297] and various models based on confinement time scaling-laws, with the Weiland model [283] a planned addition. Users can construct customized transport models using these ingredients, or define their own model using any of the code profiles and diagnostics (e.g. MHD stability). For neutral beam (NB) fuelling, heating and current drive, Corsica uses a Monte Carlo deposition technique [298] with an exact orbit calculation for the weights. Electron cyclotron heating (ECH) and current drive (ECCD) are obtained from the TORAY-GA [90, 299] ray tracing code. Currently, ICH is modelled by analytic profile shapes that can also be used for adding arbitrary heating and current drive models. The bootstrap current is obtained from a neoclassical model with NCLASS [281] generally used, but Hirshmann–Sigmar [300] and Chang–Hinton [301] are also available. Corsica has internal stability packages for assessing linear $n = 0$ MHD and ballooning stability and is also coupled to the DCON [302] ideal MHD stability code that can be run under program control or interactively. To study the effects of fluctuations, Corsica includes various sawtooth models and a hyper-resistive term (fourth-order) [303] in Ohm's law and hyper-resistive models for current diffusion processes. Corsica is a modular code allowing for easy implementation of additional transport modules: heating, fuelling and current drive sources and simulated plasma diagnostics for modelling experimental measurements. Corsica allows users to save the simulation state at arbitrary times and supports full restart capability from these saved conditions.

TASK [304] has been developed for predictive simulation of tokamak plasmas including modelling of various heating and current drive schemes. It is composed of several modules and common libraries. The transport module TASK/TR solves diffusive transport equations for the density, toroidal momentum and temperature of any species and the poloidal magnetic field. The available turbulent transport model includes the CDBM model [305], the IFS/PPPL model [295], the GLF23 package [282] and the Weiland model [306]. Neoclassical transport is described by the NCLASS package [281], Sauter's model [307, 308] or simpler models. The transport module is coupled with a fixed-boundary equilibrium module TASK/EQ including the effect of toroidal plasma rotation. TASK/WM is a 3D full wave analysis module to describe ICRF heating and fast wave current drive. A ray tracing and beam tracing module TASK/WR describes the ECCD and LHCD. These two wave modules are coupled with a 3D bounce-averaged Fokker–Planck module TASK/FP that represents the time evolution of the velocity distribution function of electrons and ions. The deformed distribution function can be used as an input of the wave dispersion module TASK/DP that evaluates various models of plasma dielectric tensor for the wave modules. The interface with experimental profile data, such as the ITPA profile database, and most of the data exchange interface between modules are included in TASK/PL. The transport simulation with the CDBM transport model reproduces the formation of ITB and current hole in JT-60U discharges through the reduction of transport for lower magnetic shear and larger Shafranov shift [309].

TOPICS (Tokamak Prediction and Interpretation Code System) [310] is an integrated code system for the predictive

simulation and interpretation of the experimental data. The base part of TOPICS is a 1.5D transport code for electron and ion temperatures, densities of any species and poloidal magnetic field, self-consistently solved with the fixed, or free, boundary equilibrium of any shape including the external heat, particle, momentum and current sources. Available turbulent transport models include the CDBM model [305], the GLF23 model [282] and the MMM95 model [311]. The neoclassical transport and bootstrap current are obtained from the matrix inversion model [5] or NCLASS model [281]. For NB fuelling, heating and current drive, TOPICS internally uses a 1D or 2D Fokker–Planck code and is also coupled with an orbit-following Monte Carlo (OFMC) code [312]. ECH and ECCD are calculated with a ray tracing method, solving the relativistic Fokker–Planck equation [313]. TOPICS is coupled with a linear ideal finite-n MHD stability code, ERATO-J or MARG2D [314], that can be run interactively. TOPICS calculates the time evolution of the NTM magnetic island width by solving the modified Rutherford equation consistently with plasma profiles and can take into account the confinement degradation due to the NTM islands [315]. For the simulation of current hole plasmas, a model of the current limit in the current hole region on the basis of the axisymmetric tri-magnetic-island (ATMI) equilibrium is applied to the MHD equilibrium calculation [310].

TRANSP is a 1.5D transport code [298, 316] for multiple plasma species, fast ion species and magnetic fields. It inputs a specified, time-evolving general toroidally-symmetric boundary and uses a variety of Grad–Shafranov solvers to calculate the time-evolving flux surfaces. It uses a Monte Carlo beam and fusion ion package (NUBEAM, [298]) to solve for the NBI deposition, current drive and phase-space distributions. Several ICRH packages (SPRUCE [317] and TORIC [318]) calculate fast wave heating. TORAY-GA [82] is used for electron cyclotron heating and current drive. The LSC code [319] models LHCD. Although TRANSP was developed mainly as a plasma analysis code, it has a variety of predictive models built in, such as GLF23 [291], IFF-PPPL [295] and RLW [296]. TRANSP solves flux conservation equations for flux surface averaged 1D transport for energy, particles, current density and momentum. Alternatively, the current density can be constrained by equilibrium reconstructions from EFIT [248] including motional Stark effect (MSE) measurements. TRANSP has been used for calculating parameters of interest in H-mode plasmas in ITER-EDA [320] and in ITER-FEAT [321].

The tokamak simulation code (TSC) [322] was developed for predictive time-dependent transport simulations. This code solves the axisymmetric 2D MHD-Maxwell's equations on a rectangular grid in (R, Z) space. 1D flux surface averaged transport equations are solved for energy, particles and current density utilizing pre-defined transport coefficients (from theoretical models or experimental data). The plasma is free-boundary so that surrounding conducting structures and poloidal field coils are included, allowing feedback systems to be incorporated. The code also has numerous peripheral physics models for bootstrap current, sawtooth evolution, ripple losses, etc.

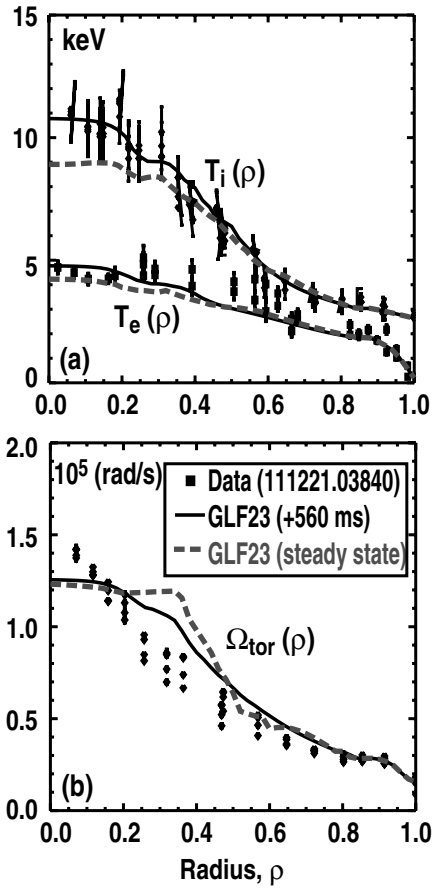

Figure 40. Theory-based (GLF23) model predictions and experimental measurements of profiles of (*a*) electron and ion temperature and (*b*) angular rotation velocity for the previously reported ≈90% non inductive AT discharge in DIII-D. Solid curves are predicted profiles with time-dependent calculation at 0.56 s after starting with the initial experimental profiles, and dashed curves are steady state calculations including the poloidal magnetic field equation.

6.3. Benchmarking on existing experiments

CRONOS is presently operating on the Tore Supra, JET, FTU and ITPA databases and contains the full geometry of projects such as ITER and SST1. The experimental basis for such a development is the interpretative simulation of the steady state advanced mode of operation of JET, relying on a plasma current profile pre-shaping phase mixing plasma current ramp-up and LHCD to reach the steady state q-profile target as soon as possible in the discharge.

The retuned GLF23 model [291] has been validated by comparing the simulations with the recent DIII-D experiments aiming at fully non-inductive operation at high beta. Successful validation is exemplified by GLF23 modelling in ONETWO for the evolution towards a stationary state of a DIII-D discharge with a 90% non-inductive fraction [111]. The T_e, T_i and toroidal momentum equations are solved with a self-consistent source and sink calculations by time stepping from initial profiles over several confinement times. Density profile is fixed using the experimentally measured profile at one time. figure 40 shows the resulting profiles that are in good agreement with experimental profiles. Stationary state performance with

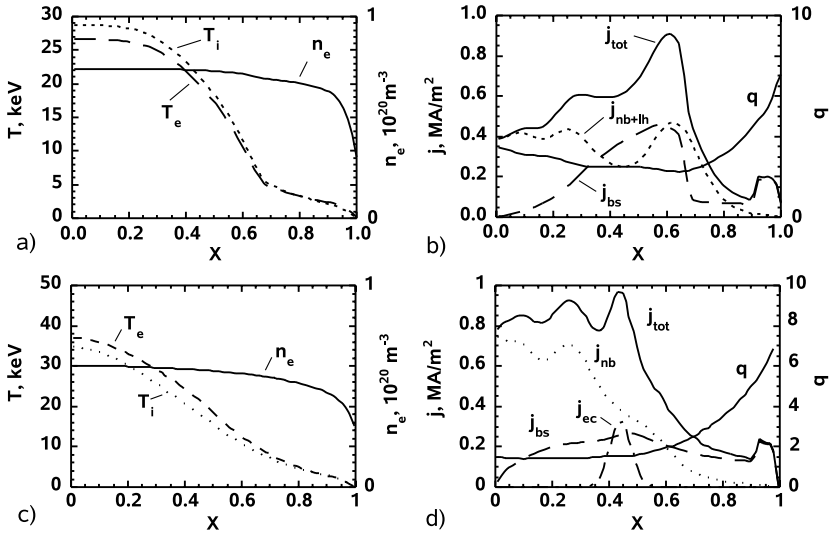

Figure 41. ITER reference scenario-4 Type-I (*a,b*) and Type-II (*c,d*) from ASTRA simulation. (*a*) Electron density profile (n_e), electron temperature profile (T_e) and ion temperature profile (T_i), (*b*) the q-profile, the total current density profile (j_{tot}), the bootstrap current density (j_{bs}) and the combined current density profile from neutral beam injection and LHCD (j_{nb+lh}), (*c*) electron density profile (n_e), electron temperature profile (T_e) and ion temperature profile (T_i) and (*d*) the q-profile, the total current density profile (j_{tot}), the bootstrap current density (j_{bs}) and the combined current density profile from neutral beam injection and LHCD (j_{nb+lh}).

the Ohmic current completely relaxed is calculated by the globally convergent modified Newton method. Simulation shows a small drop in the central safety factor due to the fully penetrated Ohmic current with little change in other profiles.

Corsica has been used to model a variety of DIII-D discharges including ELMy H-mode, strong negative central shear (NCS), quiescent double barrier (QDB) and QH-mode discharges. The current profile control of internal transport barriers (ITB) approaching steady state conditions was explored for the NCS and QDB conditions. The NCS simulations included feedback modelling of the EC antenna aiming to control the q-profile with ECCD[14] [323, 324].

Systematic comparison of the results of TASK with 55 shots of L- and H-modes in the ITPA database was carried out with the CDBM, GLF23 and Weiland models [325]. The ITB formation on JT-60U was also reproduced with the CDBM transport model including the effect of $E \times B$ rotation shear [304].

TOPICS is presently used on JT-60U for interpretation of experimental data and development of physical models. The NTM model on the basis of the modified Rutherford equation was validated by comparing calculated time evolutions of magnetic island width with those measured in experiments [326]. Profiles and their time evolutions in current hole plasmas with the box-type ITB observed in experiments were reproduced by applying the current hole model and by using a transport model which assumes that the anomalous transport is sharply reduced to the neoclassical level in the reversed magnetic shear region [327].

6.4. Main results from simulations for ITER

One of the goals of the ITER is a demonstration of an operation with fully non-inductive current drive (CD) with fusion gain $Q > 5$ and duration of at least 3 000 s [38]. Such a scenario is referred to as a reference scenario-4 ($I_p = 9$ MA, $Q = 5$) and is widely used as a common scenario for ITER simulation.

In the absence of a reliable transport model, the goal addressed by ASTRA simulations was to study the operational space where steady state (SS) operation is possible. The SS studies should address the following aspects.

- The requirements on the energy confinement time which could provide fully non-inductive current drive with $Q > 5$ should be identified after consideration of the capability of current drive and heating facilities designed for ITER.
- The power loss limit to the divertor [280] should be estimated to make sure that the peak heat flux, helium exhaust rates and Z_{eff} at the separatrix are within an acceptable level.
- Stability against the ideal MHD and resistive wall modes (RWM) should be analysed and the feasibility of controlling the RWM should be checked [328].
- Evolution of the plasma current profile should be checked to make sure that the plasma current profile relaxes to a steady state within 3 000 s with the current drive tools available.

Time evolutions of plasma density, current and temperature are simulated with ITER heating and current drive tools in a predictive manner with particle sources and boundary conditions consistent with B2-Eirine calculations. Plasma density and energy confinement time are considered as key variables to characterize SS operation with $Q > 5$. Two types of SS scenarios with plasma current $I_p = 9$ MA were simulated with the ASTRA code (figure 41). In the Type-I SS scenario [328], the minimum safety factor q_{min} was kept higher than 2 (figure 41(*b*)) to avoid possible excitation of NTMs, preventing possible degradation of energy confinement. Typical density (n_e) and temperature (T_e, T_i) profiles with a transport barrier in the reversed magnetic shear zone are presented in figure 41(*a*). The safety factor profile control is carried out by a variation of the off-axis LHCD power (~30 MW) in addition to the

[14] US Snowmass Summer Study, http://web.gat.com/snowmass (July 8–19, 2002)

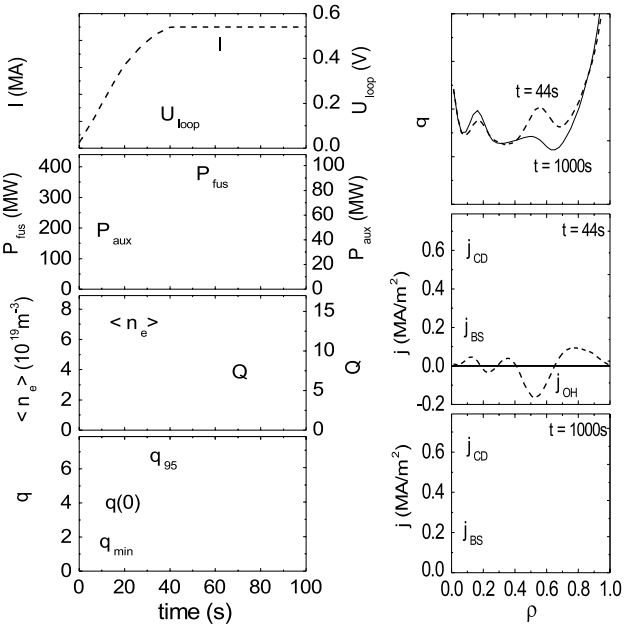

Figure 42. Fast current profile relaxation in the ITER reference scenario-4 Type-I. (From ASTRA simulation). Shown on the left are the plasma current evolution (I), the surface loop voltage ($U_{\rm loop}$), the auxiliary power ($P_{\rm aux}$) and fusion power ($P_{\rm fus}$), the line averaged electron density ($\langle n_{\rm e}\rangle$) and fusion gain (Q), values for q_{95}, $q(0)$ and minimum q ($q_{\rm min}$). On the right are shown the q-profile at $t = 44$ s and $t = 1000$ s. The current density profile from the current drive sources ($J_{\rm CD}$), the bootstrap current ($J_{\rm BS}$) and the ohmic transformer ($j_{\rm OH}$) at $t = 44$ s and $t = 1000$ s.

tangential NB injection (1 MeV 2D-beams with total power $P_{\rm NB} = 34$ MW). $H_{98}(y, 2) = 1.3$–1.5 is required to provide the SS operation. Such an operational point is above the ideal MHD no wall limit and requires active RWM control [329]. The stable operational space shrinks with an increase of pressure peaking [328].

To extend the operational space, alternative SS operational scenarios (Type-II) are proposed for ITER [328, 330] (figure 41(*c*) and (*d*)). If $H_{98}(y, 2)$ can be increased to ∼1.5–1.7, the required non-inductive current can be achieved with the help of tangential NB injection ($P_{\rm NB} = 33$ MW) and ECCD ($P_{\rm EC} = 20$ MW), which are planned to be installed for current drive and NTM suppression at the initial phase of ITER operation. In both types of scenarios, the bootstrap current fraction is $f_{\rm BS} \sim 0.5$. In the Type-II scenario, total current density profile ($j_{\rm tot}$) is more peaked. As a result, the internal inductance $l_{\rm i}(3)$ [331] increases from ∼0.6 to ∼0.8, expanding the MHD stable operational space.

An example of the SS scenario Type-I in ITER with a fast ramping up of the plasma current (I), heating and current drive power ($P_{\rm aux}$) and fusion power ($P_{\rm fus}$) simulated with the ASTRA code [332] are presented in figure 42. No feedback control is applied. The early phase of the discharge (left column) is designed in a way to obtain, early in the discharge, a $q(\rho)$ profile close to the steady state value. In the right column, $q(\rho)$ profiles at $t = 44$ s and $t = 1\,000$ s are shown along with radial profiles of the Ohmic current density ($j_{\rm OH}$), bootstrap current density ($j_{\rm BS}$) and current density ($j_{\rm CD}$) produced by neutral beam injection (at $\rho \sim 0.05$ and ∼0.2) and lower hybrid waves (at $\rho \sim 0.65$).

The CRONOS suite is presently used to investigate the complete time sequence from the X-point formation to the steady state and the relative role played by the various heating and current drive sources, including bootstrap current, alpha particles and the possible use of off-axis LHCD or ECCD. The work performed with CRONOS for ITER at this time focuses on the following questions. (i) What is the pre-shaping capability of the ITER current profile during such a phase ($\mathrm{d}I_{\rm p}/\mathrm{d}t \leqslant 0.2\,\mathrm{MA\,s^{-1}}$, $P_{\rm NNBI} \leqslant 33$ MW, $P_{\rm ICRH} \leqslant 20$ MW, $P_{\rm LHCD} \leqslant 20$ MW, the role of ECRH being not yet investigated)? (ii) Can we reach a fully non-inductive situation at $I_{\rm p} = 9$ MA, $Q = 5$, $\langle n_{\rm e}\rangle = 6.5 \times 10^{19}\,\mathrm{m^{-3}}$, using (or not using) the LHCD power during the plasma current plateau phase? (iii) Under which conditions can such a discharge become stationary? Such issues, on ITER more than anywhere else, are obviously linked with the detailed role of a dominant fraction of bootstrap current and the alignment of the plasma current and pressure profiles. The zero-D simulations confirm that a fully non-inductive situation is accessible for such parameters, provided that an energy confinement enhancement takes place at the typical level of 1.4–1.5 times the IPB98(y, 2) scaling expression [1] prediction and that the internal inductance does not fall below 0.75–0.8 (because of MHD limits). The diffusion coefficients used in the simulation are proportional to the inverse of the temperature gradient length and are renormalized at each time step according to the global energy confinement scaling laws (L- or H-mode, depending on the position with respect to the threshold scaling). On top of this basic confinement regime, the ITB is accessed and controlled by a local reduction of the heat conductivities at a location determined mainly by the local curvature of the magnetic field lines. Consistently with the conclusions of experiments at JET [272], the control parameter for a reduction in transport is chosen to be a linear combination of (i) the magnetic shear and (ii) the rotation-shearing rate normalized to the instability growth rate. In the region(s) where this 'actual shear' is locally lower than a critical value (chosen to be 0.05 in the simulations presented here), the heat transport is reduced back to its neoclassical value.

Similarly to JET, the present mechanism is powerful enough to insure ITER transits easily into an ITB regime during a current ramp-up phase, provided that the current ramp-up rate is on its high value side (∼0.15–0.2 $\mathrm{MA\,s^{-1}}$) as shown in figure 43. The superimposition of central ICRH (2nd harmonic T) and/or N-NBI helps slowing down the Ohmic current penetration retaining the reversed shear situation at least all along the current ramp phase. Further addition of off-axis current drive at the typical expected level (provided for instance by 20 MW of LHCD, which basically peaks at mid-radius under such conditions, with the expected current drive efficiency of $2.4 \times 10^{19}\,\mathrm{A\,W^{-1}\,m^{-2}}$) is a powerful supplementary asset in this pre-shaping phase, which helps in particular to drive the discharge along stable MHD paths (real time feedback loops are nevertheless to be developed here). Let us remind that N-NBI provides a significant level of current drive to the discharge, included in the simulations, but with a broad deposition profile and no location control parameter. ICCD effects are presently not considered. The typical resulting behaviour of the ITER discharge is the expected transition from an L to an H + ITB mode at about 5–6 MA

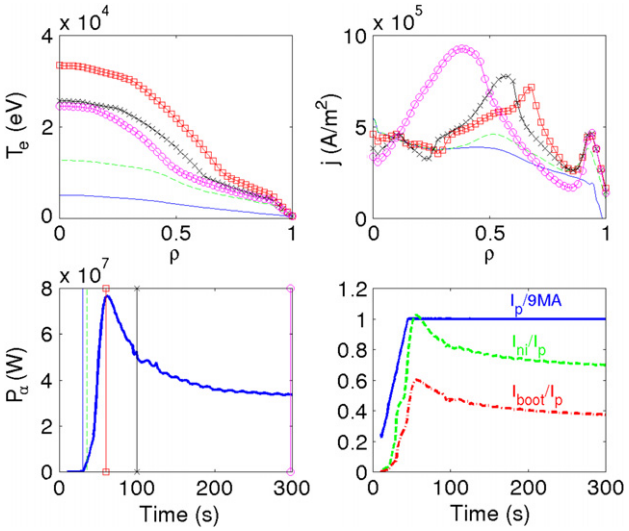

Figure 43. Summary of a CRONOS simulation of the first 300 s of an ITER type 4 scenario ($dI_p/dt = 0.2$ MA s^{-1}, $P_{NNBI} = 33$ MW, $P_{ICRH} = 20$ MW, $P_{LHCD} = 20$ MW, $I_p = 9$ MA, $\langle n_e \rangle = 6.5 \times 10^{19}$ m^{-3}). Top left: electron temperature profiles at $t = 30$ s (just before L–H transition, solid blue line), $t = 35$ s (just after L–H transition, dashed green line), $t = 60$ s (maximum performance with broadest ITB, red squares), $t = 100$ s (black crosses) and $t = 300$ s (purple circles). Top right: plasma current density profiles (same time slices as top left). Bottom left: alpha particle power (the additional injected power is 73 MW). Bottom right: plasma current, non inductive current fraction and bootstrap current fraction.

under heat transport conditions sufficient enough to insure the production of alpha particles up to levels of 40–80 MW, i.e. to reach Q of the order of 5 and a fully non-inductive situation constituted of $f_{BS} \sim 0.6$, $f_{LHCD} \sim 0.2$ and $f_{NBCD} \sim 0.2$, consistent with zero-D predictions. The bootstrap current profile is essentially constituted of the edge pedestal pressure that can be considered as stationary for such a simulation and a large peak at the ITB level, around mid-radius. This peak is almost fully driven by the temperature gradient, as the density profile is assumed extremely flat in the plasma core, and tends to lie slightly inside the ITB region. The resulting effect, directly deduced from the assumption on the link between the ITB and the minimum shear region, is a slow shrinkage of both the ITB and the minimum shear region, despite the velocity shear correction found not strong enough in the present simulations. This severe misalignment of the pressure and current profiles brings the discharge back to stationary but much lower Q-values around 2 and non-inductive current fractions around $f_{NBCD} \sim 0.6$–0.7 after 1–2 current diffusion times (i.e. 200–400 s). To counteract this ITB shrinking, one must drive (additionally) an off-axis current peak in the positive magnetic shear region, with current density sufficient enough to balance the bootstrap effect. This requires a very narrow current drive profile, with a width of the order of 10% in normalized radius in the simulation. Note that this is at the low limit of the present simulations of LHCD (ray tracing+Fokker–Planck) for ITER. This preliminary results nevertheless draw two conclusions: (i) it is hard to believe under such assumptions that a very high bootstrap current fraction ($f_{BS} \sim 0.8$–0.9) discharge is a good candidate for a stationary situation, in the case of ITBs combined with a flat density profile, and (ii) with the present input powers, one should favour the off-axis current drive schemes that provide the narrowest peaked profiles and the highest current drive efficiencies. More work is now underway in the optimization, refining the alpha particle simulations in particular to better predict their pressure and bootstrap profiles when taking into account finite Larmor radius effects. CRONOS is also now in a position to include predictive simulations on density profiles, consistently with the latest theoretical developments and experimental observations on anomalous pinch effects for instance. If such anomalous particle pinches occur in ITER, which is still an open question, the resulting peaking of the density profile may strongly influence the dynamics of the current profile. ECCD models and the latest developments around LHCD modelling will also be included in the simulations. Finally, 'real time' feedback loops will be tested to force the discharge along either pre-defined paths or accordingly to self-optimization rules.

The transport code ONETWO is applied to simulation of ITER steady state scenario with the heating and current drive capabilities available in the initial operation phase (33 MW of 1 MeV negative ion based NBI; 20 MW of ICRF at 56 MHz; and 20 MW of the midplane launched EC). The objective of this ITER simulation is to obtain an existence proof of a steady state solution for a 100% non-inductive operation with fusion gain (Q) > 5 and bootstrap current fraction (f_{BS}) > 0.6 using a first principle model with a self-consistent source and sink calculations. The present work focuses on the experimentally validated GLF23 transport model that can predict a steady state solution of fully non-inductive operation using the Day-1 hardware capabilities. (we will not be addressing questions such as dynamic access to the regime or optimized alignment of bootstrap current and current drive in this stage.) While plasma density profiles are prescribed (as shown in figure 44(*b*)), the electron and ion temperature and toroidal rotation velocity profiles are evolved with boundary conditions imposed at $\rho = 0.9$. $n_{He}/n_e = 4\%$ and some carbon impurity is assumed, resulting in $Z_{eff} = 1.2$ in the core region ($\rho < 0.4$) to $Z_{eff} = 2$ near the plasma edge. The MHD equilibrium used in the simulation is taken from a DIII-D like AT equilibrium used in previous studies [333]. Since the core temperature depends strongly on the edge temperature due to the stiff transport model, scans of an assumed edge temperature value are used to determine the required edge temperature for achieving the goal of the steady state scenario (100% non-inductive current fraction with $f_{BS} > 0.6$). The results of the simulations (figure 45) [334] indicated that the projected performance can be met with T ($\rho = 0.9$) of 7 keV with some uncertainties of bootstrap models (NCLASS [281] or Sauter model [307,308]). Note that with a typical temperature pedestal width ~5% in ρ space, the required temperature at the top of the edge pedestal would be lower than these values. The radial profiles of the simulation for the 100% non-inductive fraction are shown in figure 44, and the corresponding parameters are listed in table 2 [335]. The parallel electric field is fully penetrated and the Ohmic current is (within the perceived accuracy of our modelling) essentially zero. These parameters correspond to the zeroD operation space of fusion performance figure of merit, $\beta_N H_{89}/q_{95}^2 = 0.27$ with $f_{BS} > 0.5$.

Primarily for reasons of efficiency, the present modelling of the steady state scenarios is performed in two phases. In

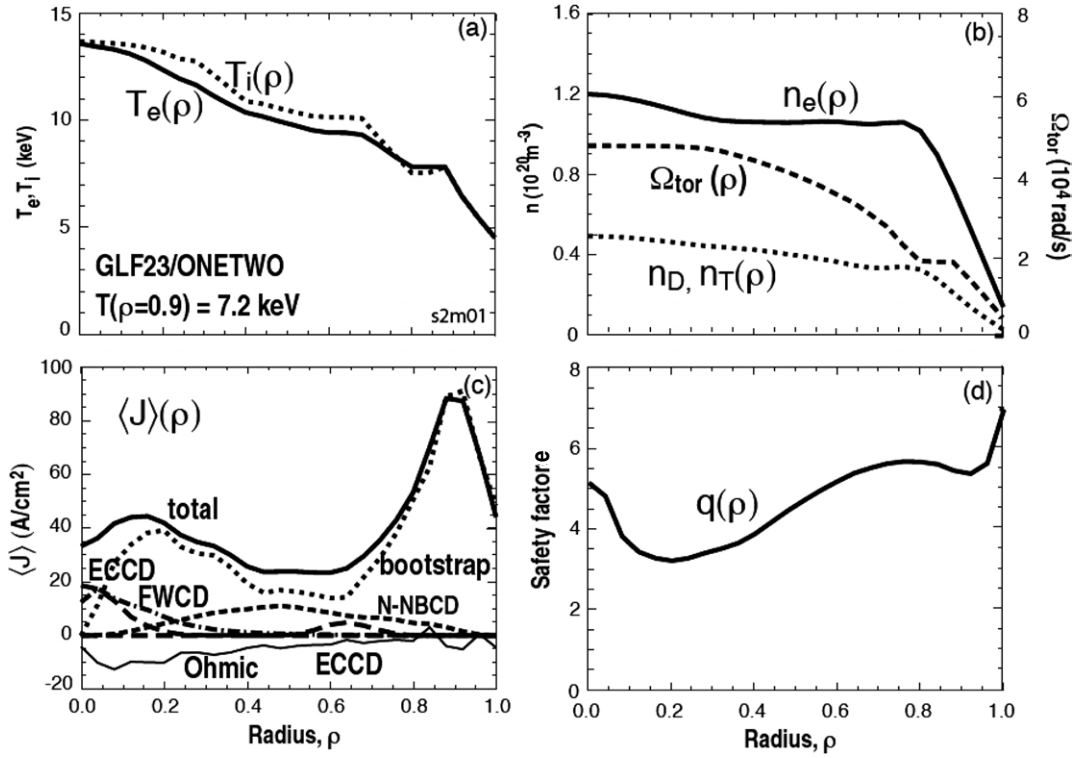

Figure 44. Predictive modelling of ITER steady state scenario using the GLF23 transport model: (*a*) predicted electron and ion temperature profiles, (*b*) assumed electron, deuterium and tritium profiles, predicted toroidal angular rotation velocity, (*c*) current components and (*d*) safety factor profile.

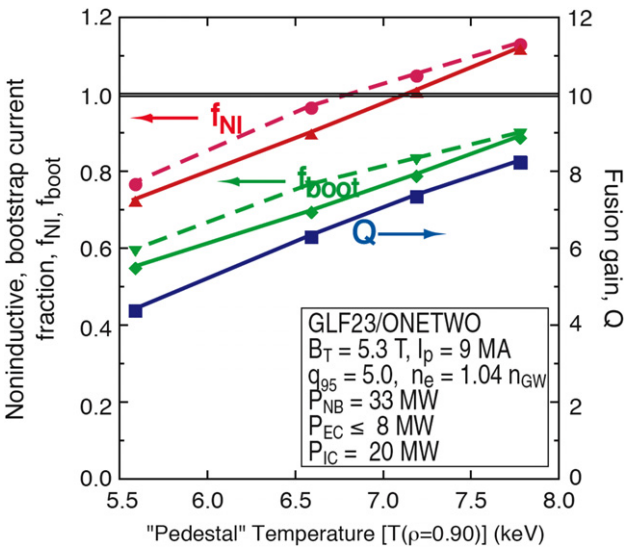

Figure 45. Variation of fusion gain Q, non-inductive current fraction $f_{\rm NI}$ and bootstrap current fraction $f_{\rm BS}$ with edge temperature at $\rho = 0.90$ computed using GLF23 transport model. The bootstrap current is based on NCLASS (——) and Sauter (- - - -) models.

the first time-evolved phase of the calculation, the electron and ion temperatures and toroidal rotation are brought into a state of near equilibrium with all current drive sources included. However, the current evolution is not in a near steady state condition at the end of the first phase since the toroidal electric field relaxes much more slowly than the remaining profiles. In the second phase, the time evolution in the diffusion

Table 2. Parameters for the simulation with the 100% non-inductive fraction ($T(\rho = 0.9) = 7.2$ keV, NCLASS bootstrap model).

$P_{\rm NB}$ (MW)	33	$f_{\rm BS}$	0.78
$P_{\rm FW}$ (MW)	20	$f_{\rm NBCD}$	0.18
$P_{\rm EC}$ (MW)	20	$f_{\rm FWCD}$	0.03
$B_{\rm T}$ (T)	5.3	$f_{\rm ECCD}$	0.03
$I_{\rm p}$ (MA)	9.0	$f_{\rm NI}$	1.02
q_{95}	5.2	Q	7.3
$n_{\rm e}(10^{20}\ {\rm m}^{-3})$	0.92	$\beta_{\rm T}$ (%)	2.7
$n_{\rm e}/n_{\rm G}$	1.04	$\beta_{\rm N}$	2.9
$T_{\rm e}(0)$ (keV)	16.9	H_{89}	2.6
$T_i(0)$ (keV)	19.8	$\beta_{\rm N} H_{89}/q_{95}^2$	0.27

equations is turned off resulting in a steady state solution for the current density while holding all other profiles at the final values determined in the first phase. If a satisfactory time independent solution cannot be found simultaneously for all profiles, the first phase is used as an initial starting guess in the iterative process that is required to solve the coupled non-linear equations in the second phase. The first phase is almost always required when GLF23 is used. Otherwise, starting from some plausible initial profiles does not lead to a converged steady state solution.

During the above processes, the MHD equilibrium is fixed for the cases shown in figures 41 and 42, and table 2 and only updated at the end of phase 2. Thus the MHD derived metrics that appear as coefficients in the diffusion equations are time independent in both the first and second phases of the evolution. In a subsequent run, the MHD equilibrium is re-determined using the pressure and current density profiles

obtained in phase 2 from a previous calculation. It is found that the effect of this handling of the MHD equilibrium results in small changes in the current density and q-profile near the magnetic axis, due to changes in the volume enclosed by a given flux surface. More recent runs for longer times with the MHD equilibrium calculated throughout confirm that the final solution changes very little. Note, however, that all our MHD equilibrium calculations are based on fixed- (as opposed to free-) boundary computations. Hence issues of coil currents, etc that might be required to maintain such an equilibrium are not addressed. The present modelling still has the following caveats.

(1) The edge temperature used in the above modelling is the edge temperature required for generating the $Q = 5$ ITER steady state scenario using the specific theory-based model as discussed above [334]. As such it is not based on any edge physics model. Therefore the validity of the edge temperature needs to be investigated. The temperature fixed at $\rho = 0.9$ seems high (of ~7.2 keV), but the value of $\beta_{\mathrm{ped}} = 1.2\%$ at $n_{\mathrm{e}} = 6 \times 10^{19}\,\mathrm{m}^{-3}$ appears to be below the maximum stable β_{ped} for the peeling–ballooning mode [336].
(2) The density profile used in the present modelling originates from the one used in an earlier ITER simulation study as a density profile similar to DIII-D AT discharge. The density profile is fixed. Consequently, these results may change when the density is also dynamically modelled. It is our plan to include the density equation with GLF23 model.
(3) The steady state in the modelling disregards the dynamic accessibility issues and hence the steady state determined may in fact not be achieved. Particularly with stiff, strongly non-linear confinement models such as GLF23, there are added risks that bifurcations that might occur in a fully time-evolved calculation are not seen.

Future optimization is in progress (lower density regime and better alignment of CDs). Some important AT physics issues that have to be addressed include consistency of pedestal temperature, divertor heat load issues and stability issues, in particular, RWM and error field effects.

ITER scenarios currently simulated by Corsica include steady state discharges with internal transport barriers. Generally, these simulations use heating and current drive sources to evolve the equilibrium and current drive consistent with a GLF23-based thermal transport model. Due to limited benchmarked models for particle fuelling, particle transport, except for alpha particles, is generally not turned on and the electron density temporal variations and profiles are prescribed. Alpha-particle build-up, however, is determined from a production rate equation with its particle diffusivity proportional to the electron thermal conductivity to simulate alpha particle profile dilution effects. Self-consistent, first principle pedestal predictions and barrier formation are still an issue due to limitations in the edge transport models. ITER ITB discharge evolution is simulated by ramping down to a 12 MA discharge while forcing barrier formation at 120 s into the discharge [38]. Scenario discharges with $Q > 10$ and $P_{\mathrm{fusion}} \sim 250$ MW are achieved using neutral beam heating and current drive. In these simulations, the barrier is forced to form by reducing transport coefficients at some desired radial location, typically chosen to be near q_{min}. These simulations were primarily completed to explore plasma diagnostic issues associated with ITB scenarios. In addition, current interests for scenario modelling include the formation of various q-profiles using the heating and current drive sources early in the discharge during ramp-up to generate self-consistent discharge scenarios with $q > 1$ (no sawteeth). Simulation of advanced scenarios with ITBs demands the use of additional physics capabilities within the transport models, e.g. shear rotation effects and angular momentum transport, so as to form edge and core barriers using these experimentally relevant parameters. New Corsica capabilities for operation with a plasma control system (a PCS) [324] are also currently under development. This work builds on previous efforts with Corsica in evaluating various ITER controllers. It will provide the capability for studying a variety of feedback control issues needed to sustain advanced tokamak scenarios in ITER.

The TASK code was applied to the simulation of the ITER steady state scenario. At present the temperatures of electron, D, T and He, the stored energy of energetic beam ions and alpha particles and the current density are solved, while the density profile is fixed. With the CDBM transport model, current ramp up and off-axis current drive lead to reversed magnetic shear configuration and ITB formation. Time evolution of the current profile is sensitive to the initial current profile and the edge temperature. It takes a very long time for the current profile in the high temperature central region to change, and the high edge temperature prevents the current profile from penetrating into the plasma. With careful adjustment of the timing and location of heating and current drive, $Q > 5$ operations with zero loop voltage are achieved, though the induced current still exists in the central region. Optimization of the time sequence of the heating and current drive requires a validated transport model a reliable edge plasma model and self-consistent heating and current drive modelling. Further development of the TASK code in these directions is underway.

The TOPICS code was applied to the ITER steady state simulation of weakly and strongly reversed magnetic shear (RS) plasmas with ITB by using a transport model validated in JT-60U strongly-RS (current hole) plasmas with the box-type ITB [327]. The profiles of fuelling and heating of NB and EC were prescribed for simplicity and driven currents were calculated using their respective current drive efficiencies. Operations with $Q > 5$ were achieved in simulations of both weakly- and strongly-RS plasmas. The estimated values of Q, β_{N} and the bootstrap current fraction in the strongly-RS plasma were higher than those in the weakly-RS plasma. The MHD stability analysis is required especially for the strongly-RS plasma. Further optimization of q-profile and current drive position is necessary not only for the performance improvement but also for the reduction of time to obtain the steady state. The model improvement, such as $E \times B$ shear stabilization especially for the weakly-RS plasma, heating and current drive, is underway.

The TOPICS code was also applied to predict the ECCD power necessary for the NTM stabilization in ITER [326,337]. The NTM model was validated by comparison with JT-60U experiments. The EC wave with a frequency of 170 GHz is launched from a position of an upper launcher. ECCD power

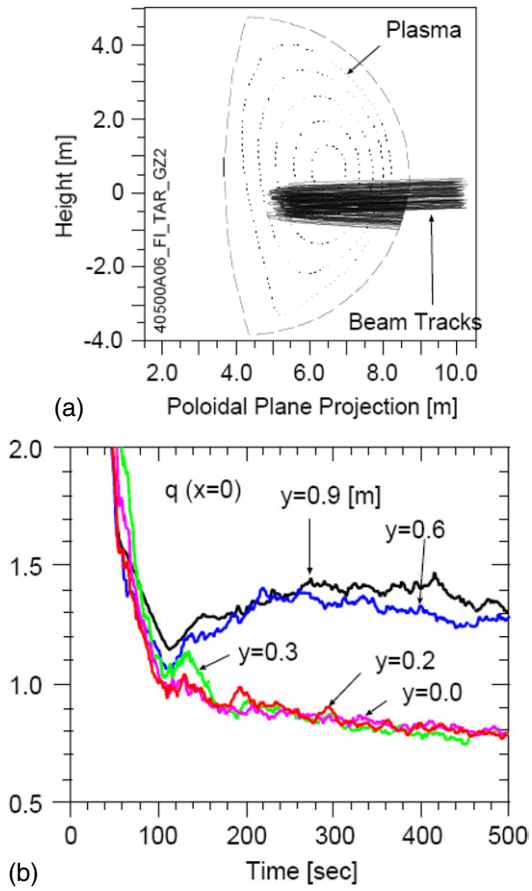

Figure 46. TRANSP/TCS simulations of variations to the aiming of negative based neutral beam injection in ITER at different angles into an ITER hybrid plasma. (*a*) Horizontal view of neutral trajectories aimed at $y = 0.9$ [m] below the plasma axis at the point on the trajectory of the minimum major radius. (*b*) Time evolution of the $q(0)$ for various y showing that off-axis aiming can generate sufficient current drive to maintain q greater than unity.

necessary for the simultaneous stabilization of both $m/n = 3/2$ and $2/1$ modes was evaluated to be 30 MW. The necessary ECCD power could be reduced to 12 MW when optimizing both toroidal and poloidal injection angles of ECCD to halve the EC current width. In the present analysis, the error of the estimated ECCD power requirements to stabilize the NTM is about 20% (due to experimental uncertainties of the experiments today). Hence, more precise estimations of the parameters require more experiments in JT-60U in the future.

Recently TRANSP and TSC are being used in combination to utilize their particular strengths to provide improved predictions for ITER. The boundary-evolving and predictive capabilities of TSC are used to develop the full time evolution of an ITER discharge, and TRANSP is used for correcting the heating and current drive profiles with more sophisticated source models and for computing fast ion parameters such as grad(β_α). Results for ITER hybrid plasmas have been published [338] and have been submitted to the ITPA profile database. For example the effects of applying the ITER NBI system at various different injection angles into a hybrid plasma has been simulated and the results shown in figure 46.

6.5. Conclusions

Since the early developments (initiated by the ITER physics team) on the capability to achieve the anticipated current profile required for steady state scenarios on ITER, a large worldwide effort is now being undertaken with codes at a different degree of sophistication. So far, all present simulations are done for the ITER steady state scenario: $I_p = 9$ MA fully non-inductively driven, $Q = 5$. Due to the variety of transport models used and also the various hypotheses made on the heating and current drive systems considered for ITER, a real benchmarking of the results is not really yet available. Nevertheless, some conclusions can already be drawn. It appears that the production of deeply reversed current profiles is hardly feasible. However, production of weakly reversed current profile appears feasible, with the full heating and current drive techniques foreseen for ITER. Sensitivity studies on the available power are not yet done. This is particularly important if part of the available power for heating and current drive is needed for control purposes.

In all cases, an effective off-axis current drive technique in the outer part of the plasma is needed. This is provided either by using LHCD or by allowing the pedestal to reach a high value of the bootstrap current. In addition, the plasmas selected for ITER are at a relatively low density with a high electron temperature to optimize the current drive efficiency (NBCD, ECCD in particular). Compatibility between edge and divertor in these conditions remains to be assessed. The capability of the heating and current drive systems foreseen in ITER to maintain the required current profile configuration in steady state is not yet fully assessed, partly due to the difficulty the codes have in following the plasma parameters from the very start (during the current ramp-up phase) up to the very long time required to assess the current profile evolution. Numerical techniques are developed to answer this problem.

7. Summary

Steady state and hybrid scenarios have been defined through their respective objectives. While the reference ELMy H-mode scenario for ITER aims at producing a fusion gain of $Q = 10$ for 400 s at a plasma current of $I_p = 15$ MA corresponding to q_{95} of 3.0 ($B_T = 5.3$ T), the steady state scenario aims at producing discharges where the current is driven fully non-inductively with $Q = 5$ at $I_p = 9$ MA ($q_{95} \sim 5$). In the hybrid scenario, plasma current is driven with a combination of inductive and non-inductive currents at a current (12–14 MA) lower than the reference H-mode scenario but higher than steady state scenarios. The hybrid scenario is intended to provide operation with a long burn time (>1 000 s), high fluence/shot and $Q > 5$ with a high reliability for engineering tests. To achieve these goals, only a moderate assumption on confinement and beta ($H_{98}(y, 2) \sim 1$ and $\beta_N \sim 2$) are required. An 'advanced hybrid' scenario is a hybrid scenario aiming at producing high fusion yield and features a higher beta limit with an optimized current profile, a lower current and a lower loop voltage, which would allow operating with a high fusion gain for a long pulse duration. Projections of present experiments to an ITER advanced hybrid scenario give performance up to $Q = 10$ for 3 000 s at $I_p = 12$ MA at

$q_{95} \sim 4$. Such a regime would achieve large fusion fluence. In the long run, these scenarios will provide a route to steady state operation. A dimensionless parameter $\beta_N H/q_{95}^2$ that contains the key physics scaling is considered to be the figure of merit for evaluating both scenarios. This figure of merit ranges typically from ∼0.25 (steady state) to 0.4 (conventional H-mode) and can be $\geqslant$0.4 for the 'hybrid' scenarios. The advanced hybrid scenarios are often simply called hybrid scenarios.

Plasma current profiles allow us to classify scenarios for ITER, although several physics phenomena are involved, often interlinked, and should be taken into account. In the reference H-mode scenario for ITER, the plasma current is fully diffused and the q-profile is monotonic with positive magnetic shear and $q(0) < 1$. Configurations with moderate or weak reversed shear have permitted the development of plasmas whose characteristics are close to the one required for steady state scenarios: fully non-inductive current, high confinement and high bootstrap fraction. They are also characterized by the development of internal transport barriers when proper conditions are met. More recently, the development of magnetic configurations with a wide volume of low magnetic shear and a central value of q close to 1 have resulted in stationary discharges with improved confinement and high values of normalized beta. They are also characterized by a low level of MHD activity. These discharges extrapolate to the performance needed for the 'hybrid' scenarios foreseen for ITER and are called 'hybrid scenarios', although other configurations might be found that fulfil the hybrid mission in ITER.

The experimental development of steady state scenarios is challenging as they do require operation at the limit of the hardware capability of a given machine (high power for the maximum time duration, in particular for realistic q_{95}). Several discharges in many tokamaks (JET, JT-60U, DIII-D and ASDEX Upgrade) are now considered to be reasonable candidates for the development of steady state discharges for ITER. Plasma with improved confinement, high β_N, zero, or close to zero, loop voltage and a bootstrap current fraction higher than $f_{BS} = 0.5$ have been maintained for as long as the additional heating power was applied, with the following main characteristics.

- Operation with wide ITBs with strong temperature gradients permits the achievement of high confinement plasmas. However, beta is somewhat limited and impurity accumulation can occur. Also fuelling ITBs will need some development.
- Recent development of operation with weaker ITBs seems to alleviate these problems, although at the expense of a lower improved confinement.
- Plasma configurations with very strong reversed shear, which lead to the development of 'current hole' configurations where the plasma current does not penetrate the plasma centre, do not seem at present to be candidates for steady state scenario on ITER due to a possible lower beta limit and, moreover, due to poor confinement of energetic particles and the development of collective modes (chapter 5, this issue [22]). Further developments in future might answer these points.

The development of hybrid scenarios on several tokamaks, allowing steady operation at higher beta limits than those for the reference ELMy H-mode, has been quite remarkable in recent years. Steady values of $\beta_N H_{89}/q_{95}^2 \geqslant 0.4$, corresponding to $Q \sim 10$ in ITER, have been achieved in several experiments for many energy confinement times ($>10\,\tau_E$). However, some issues remain to be studied.

- It is important to understand the current profile evolution and the need for active control.
- It is also important to assess further the operational space for high beta operation and for ITER-relevant ρ^* and ν^*.

The heating and current drive actuators foreseen for ITER are well developed. The main features of NBCD at 0.5 MeV, i.e. in the range foreseen for ITER, have been found in agreement with theoretical predictions. EC waves are widely used both for heating and for current profile control. For an off-axis current drive location up to mid-radius, there is a very good agreement between experimental results and numerical simulation. A large code benchmarking effort is in progress for a very off-axis current drive (for NTM control). Substantial steps forward have been made on the LHCD coupling in steady state scenarios as well as on code benchmarking, giving a reasonable confidence for LHCD application on ITER. ICRH has a very large variety of applications in present tokamaks. Here also, substantial progress has been made in coupling the RF power in ELMy discharges and numerical simulation of ICRF heating schemes.

Thanks to a better understanding and modelling of heating and current drive actuators and the development of real time information on key parameters such as the current profile and the strength of the ITB, sophisticated algorithms have been used for the active control of the experimental steady state and hybrid scenarios. One of the main remaining issues is the development of scenarios, or of algorithms, resulting in the lowest possible demand on control in terms of additional power.

Since the early developments on the capability to achieve the anticipated current profile required for steady state scenarios on ITER, a large worldwide effort is now being undertaken with numerical codes. Most of these codes have been benchmarked on steady state discharges described in this chapter. Producing and sustaining deeply reversed current profiles is hardly feasible with the heating and current drive techniques presently foreseen for ITER. However, creating and maintaining weakly, or moderately, reversed current profile appears feasible, with the full heating and current drive power. Sensitivity studies on the available power are not yet done. In all the cases, an effective off-axis current drive technique in the outer part of the plasma is needed. This is provided either by using LHCD or by allowing the pedestal to reach quite high values of the bootstrap current.

Important issues remain, and need to be addressed in the near future: (i) simulation of the complete discharge evolution from the very start, just after plasma initiation, to the steady state conditions to assess the current profile evolution and (ii) to achieve fully integrated scenarios, i.e. scenarios compatible with the divertor of a burning physics device. In particular, steady state scenarios privilege operation at a relatively low density and high electron temperature to optimize the current

drive efficiencies. Generally, steady state and hybrid scenarios that can be considered for ITER have made impressive progress since the IPB: the domain is in full progress and new scenarios allowing the remaining issues to be progressively alleviated are being proposed. Operating a tokamak reactor at fully steady state or in a quasi steady state remains a challenging but realistic prospective.

References

[1] ITER Physics Basis 1999 *Nucl. Fusion* **39** 2175
[2] Kamada Y. *et al* 1994 *Nucl. Fusion* **34** 1605
[3] Söldner F.X. *et al* 1999 *Nucl. Fusion* **39** 407
[4] Kamada Y. *et al* 1999 *Nucl. Fusion* **39** 1845
[5] Kikuchi M. *et al* 1990 *Nucl. Fusion* **30** 343
[6] Greenwald M. *et al* 1988 *Nucl. Fusion* **28** 2199
[7] Fujita T. *et al* 2001 *Phys. Rev. Lett.* **87** 085001
[8] Crisanti F. *et al* 2002 *Phys. Rev. Lett.* **88** 145004
[9] Litaudon X. *et al* 2002 *Plasma Phys. Control. Fusion* **44** 1057
[10] Ide S. *et al* 2000 *Nucl. Fusion* **40** 445
[11] Greenfield C.M. *et al* 2003 *Phys. Plasmas* **11** 2616
[12] Sips A.C.C. *et al* 2002 *Plasma Phys. Control. Fusion* **44** A151
[13] Wade M.R. *et al* 2003 *Nucl. Fusion* **43** 634
[14] Sips A.C.C. *et al* 2003 *30th EPS Conf. (St Petersburg, 2003)* O-1.3A
[15] Hender T.C. *et al* 2007 Progress in the ITER Physics Basis *Nucl. Fusion* **47** S128–S202
[16] Mikkelsen D.R. 1989 *Phys. Fluids* B **1** 333
[17] Doyle E.J. *et al* 2007 Progress in the ITER Physics Basis *Nucl. Fusion* **47** S18–S127
[18] Luce T.C. *et al* 2005 *Fusion Sci. Technol.* **48** 1212
[19] Kamada Y. *et al* 2001 *Nucl. Fusion* **41** 1311
[20] Garofalo A.M. *et al* 2002 *Phys. Plasmas* **9** 1997
[21] Politzer P.A. *et al* 2005 *Nucl. Fusion* **45** 417
[22] Fasoli A. *et al* 2007 Progress in ITER Physics Basis *Nucl. Fusion* **47** S264–S284
[23] Sips A.C.C. *et al* 2002 *Plasma Phys. Control. Fusion* **44** B69
[24] Luce T.C. *et al* 2004 *Phys. Plasmas* **11** 2627
[25] Joffrin E. *et al* 2002 *Plasma Phys. Control. Fusion* **44** 1203
[26] Isayama A. *et al* 2003 *Nucl. Fusion* **43** 1272
[27] Luce T.C. *et al* 2003 *Nucl. Fusion* **43** 321
[28] Ide S. *et al* 2002 *Plasma Phys. Control. Fusion* **44** L63
[29] Murakami M. *et al* 2003 *Phys. Rev. Lett.* **90** 255001
[30] Isayama A. *et al* 2001 *Nucl. Fusion* **41** 761
[31] Oikawa T. *et al* 2001 *Nucl. Fusion* **41** 1575
[32] Sakamoto Y. *et al* 2005 *Nucl. Fusion* **45** 574
[33] Tani K. *et al* 1992 *J. Comput. Phys.* **98** 332
[34] Politzer P.A. *et al* 2003 *30th EPS Conf. (St Petersburg, 2003)* P4-048
[35] Shiraiwa S. *et al* 2004 *Phys. Rev. Lett.* **92** 035001
[36] Sauter O. *et al* 2002 *29th EPS Conf. (Montreux, 2002)* P2-087
[37] Takenaga H. *et al* 2003 *Nucl. Fusion* **43** 1235
[38] Shimomura Y. *et al* 2001 *Plasma Phys. Control. Fusion* **43** A385
[39] Luce T.C. *et al* 2003 *30th EPS Conf. (St Petersburg, 2003)* P4.042
[40] Suzuki T. *et al* 2004 *Nucl. Fusion* **44** 699
[41] Wolf R.C. 1999 *Plasma Phys. Control. Fusion* **83** B93
[42] Wade M.R. *et al* 2002 *29th EPS Conf. (Montreux, 2002)* O2.08
[43] Sips A.C.C. *et al* 2003 *Fusion Sci. Technol.* **44** 605
[44] Luce T.C. *et al* 2001 *Nucl. Fusion* **41** 1585
[45] Peeters A.G. *et al* 2002 *Nucl. Fusion* **42** 1376
[46] Gormezano C. *et al* 2004 *Plasma Phys. Control. Fusion* **46** B435
[47] Fukuda T. *et al* 2001 *28th EPS Conf. (Funchal, 2001)* P4.004
[48] Fujita T. *et al* 2003 *30th EPS Conf. (St Petersburg, 2003)* P2.131
[49] Litaudon X. *et al* 2004 *Plasma Phys. Control. Fusion* **46** A19
[50] Sips A.C.C. *et al* 2005 *Plasma Phys. Control. Fusion* **47** A19
[51] Inoue T. *et al* 2005 *Nucl. Fusion* **45** 790
[52] Grisham L.R. *et al* 2001 *Nucl. Fusion* **41** 597
[53] Umeda N. *et al* 2003 *Nucl. Fusion* **43** 522
[54] Kaneko O. *et al* 2003 *Nucl. Fusion* **43** 692
[55] Janev R.K. *et al* 1989 *Nucl. Fusion* **29** 2125
[56] Nemoto M. *et al* 1997 *J. Plasma Fusion Res.* **73** 1374
[57] Suzuki S. *et al* 1998 *Plasma Phys. Control. Fusion* **40** 2097
[58] Oikawa T. and the JT-60 Team 2000 *Nucl. Fusion* **40** 435
[59] Forest C.B. *et al* 1994 *Phys. Rev. Lett.* **73** 2444
[60] Oikawa T. *et al* 2004 *JAERI Res.* 2003-028
[61] Shinohara K. *et al* 2001 *Nucl. Fusion* **41** 603
[62] Ishikawa M. *et al* 2005 *Nucl. Fusion* **45** 1474
[63] Forest C.B. *et al* 1997 *Phys. Rev. Lett.* **79** 427
[64] Carolipio E.M. *et al* 2002 *Nucl. Fusion* **42** 853
[65] Petty C.C. *et al* 1999 *Bull. Am. Phys. Soc.* **44** 127
[66] Hobirk J. *et al* 2003 *30th EPS Conf. (St Petersburg, 2003)* O-4.1B
[67] Erckmann V. *et al* 1994 *Plasma Phys. Conrol. Fusion* **36** 1869
[68] Lloyd B. *et al* 1998 *Plasma Phys. Control. Fusion* **40** A119
[69] Luce T.C. *et al* 2002 *IEEE Trans. Plasma Sci.* **30** 734
[70] Prater R. *et al* 2004 *Phys. Plasmas* **11** 2349
[71] Cirant S. 2005 *3rd IAEA Technical Meeting on ECRH Physics and Technology in ITER (Como, 2005) J. Phys.: Conf. Ser.* **25** 1
[72] Prater R. *et al* 1997 *10th Joint Workshop on ECE and ECH (Ameland, 1997)* p 531
[73] Leuterer F. *et al* 1999 *Fusion Eng. Des.* **53** 485
[74] Lohr J. *et al* 2003 *Conf. on RF Power in Plasmas (Moran, USA, 2003)* p 335
[75] Cirant S. *et al* 1995 *9th Joint Workshop on ECE and ECH (Borrego Springs, 1995)* p 105
[76] Ikeda Y. *et al* 2002 *12th Joint Workshop on ECE and ECH (Aix-en-Provence, 2002)* p 475
[77] Shevchenko V. *et al* 2003 *Conf. on RF Power in Plasmas (Moran, USA, 2003)* p 359
[78] T-10 TEAM and Kislov D.A. *et al* 2001 *Nucl. Fusion* **41** 1473
[79] Tran M.Q. *et al* 1997 *10th Joint Workshop on ECE and ECH (Ameland, 1997)* p 305
[80] Westerhof E. *et al* 2002 *Nucl. Fusion* **42** 1324
[81] Darbos C. *et al* 2002 *12th Joint Workshop on ECE and ECH (Aix-en-Provence, 2002)* p 487
[82] Kritz A.H. *et al* 1982 *3rd Int. Symp. on Heating in Toroidal Plasmas (Grenoble, 1982)* p 707
[83] Matsuda K. 1989 *IEEE Tran. Plasma Sci.* **17** 6
[84] O'Brien M.R. *et al* 1992 *IAEA Technical Committee Meeting on Advances in Simulation and Modelling of Thermonuclear Plasmas (Montreal, 1992)* p 527
[85] Poli E. *et al* 1999 *Phys. Plasmas* **6** 5
[86] Poli E. *et al* 1999 *Fusion Eng. Des.* **53** 9
[87] Cirant S. *et al* 1995 *J. Plasma Phys.* **53** 345
[88] Nowak S. *et al* 1996 *Phys. Plasmas* **3** 4140
[89] Zvonkov A.V. *et al* 1998 *Plasma Phys. Rep.* **24** 389
[90] Cohen R.H. *et al* 1987 *Phys. Fluids* **30** 2442
[91] Westerhof E. *et al* 1995 *9th Joint Workshop on ECE and ECH (Borrego Springs, 1995)* p 3
[92] Harvey R.W. *et al* 1992 *IAEA Technical Committee Meeting on Advances in Simulation and Modelling of Thermonuclear Plasmas (Montreal, 1992)* p 498
[93] Giruzzi G. 1988 *Phys. Fluids* **31** 3305
[94] Giruzzi G. *et al* 1992 *Nucl. Fusion* **32** 1011
[95] Luce T.C. *et al* 1999 *Phys. Rev. Lett.* **83** 4550
[96] Petty C.C. *et al* 2002 *Nucl. Fusion* **42** 1366
[97] Sauter O. *et al* 2000 *Phys. Rev. Lett.* **84** 3322
[98] Suzuki T. *et al* 2002 *Plasma Phys. Control. Fusion* **44** 1
[99] Petty C.C *et al* 2001 *Plasma. Phys. Control. Fusion* **43** 1747
[100] Suzuki T. *et al* 2004 *J. Plasma Fusion Res.* **80** 511
[101] Farina D. 2003 *IFP-CNR Internal Report* FP 03/5 http://www.ifp.cnr.it/publications/2003/FP03-05.pdf
[102] Lin-Liu Y.R. *et al* 2003 *Phys. Plasmas* **10** 4064

[103] Pietrzyk Z.A. *et al* 2001 *Phys. Rev. Lett.* **86** 1530
[104] Henderson M.A. *et al* 2003 *Phys. Plasmas* **10** 796
[105] Angioni C. *et al* 2003 *Nucl. Fusion* **43** 455
[106] Goodman T.P. *et al* 2002 *Proc. 19th Int. Conf. (Lyon, 2002)* (Vienna: IAEA) CD-ROM EX/P5-11 and http://www.iaea.org/programmes/ripc/physics/fec2002/html/fec2002.htm
[107] Prater R. *et al* 2003 *Nucl. Fusion* **43** 1128
[108] Zohm H. *et al* 2003 *Nucl. Fusion* **43** 1570
[109] Petty C.C. *et al* 2004 *Nucl. Fusion* **44** 243
[110] Günter S. *et al* 2003 *Nucl. Fusion* **43** 161
[111] Murakami M. *et al* 2003 *Phys. Plasmas* **10** 1691
[112] Ikeda Y. *et al* 2002 *Nucl. Fusion* **42** 375
[113] Ide S. *et al* 2004 *Nucl. Fusion* **44** 87
[114] Fisch N.J. 1987 *Rev. Mod. Phys.* **59** 175
[115] Bonoli P.T. *et al* 2003 *Conf. on RF Power in Plasmas (Moran,USA, 2003)* p 24
[116] Barbato E. *et al* 2005 *Plasma Phys. Control. Fusion* **47** 2075
[117] Imbeaux F. and Peysson Y. 2005 *Plasma Phys. Control. Fusion* **47** 2041
[118] Granucci G. *et al* 2004 *Fusion Sci. Technol.* **45** 387
[119] Peysson Y. *et al* 1999 *Conf. on RF Power in Plasmas (Annapolis, USA, 1999)* p 183
[120] Zushi H. *et al* 2005 *Nucl. Fusion* **45** S142
[121] Tuccillo A.A. *et al* 2003 *Bulletin Am. Phys. Soc.* **48** 7
[122] Gormezano C. 1997 *48th Scottish Universities Summer School in Physics (St Andrews)* ed R.A. Cairns and A.D.R. Phelps (SUSSP Publications/IOP: Edinburgh/London) p 275
[123] Jacquinot J. 2005 *Nucl. Fusion* **45** S118
[124] Ekedahl A. *et al* 2003 *Conf. on RF Power in Plasmas (Moran, USA, 2003)* p 227
[125] Granucci G. *et al 30th EPS Conf. (St Petersburg, 2003)* P-1.191
[126] Bibet Ph. *et al* 1994 *Report* Eur-CEA-FC-1520 Cadarache, France
[127] Pericoli-Ridolfini V. *et al* 2004 *Plasma Phys. Control. Fusion* **46** 349
[128] Barbato E. *et al* 1991 *Nucl. Fusion* **31** 673
[129] Mckenzie J.S. *et al* 1991 *Comput. Phys. Commun.* **66** 194
[130] BernabeI S. *et al* 1997 *Phys. Plasmas* **4** 125
[131] Shoucri M. *et al* 1994 *Comput. Phys. Commun.* **82** 287
[132] Naito O. *et al* 2002 *Phys. Rev. Lett.* **89** 065001
[133] Devoto R.S. *et al* 1992 *Nucl. Fusion* **32** 773
[134] Peysson Y. *et al* 2000 *Plasma Phys. Control. Fusion* **42** B87
[135] Barbato E. *et al* 1990 *Phys. Fluids* B **2** 2687
[136] Bartiromo R. *et al* 1993 *Nucl. Fusion* **33** 1483
[137] Bonoli P.T. *et al* 1988 *Nucl. Fusion* **28** 991
[138] Fuchs V. *et al* 1989 *Nucl. Fusion* **29** 1479
[139] Cairns R.A. *et al* 1995 *Nucl. Fusion* **35** 1413
[140] Baranov Yu.F. *et al* 1996 *Nucl. Fusion* **36** 1031
[141] Valovic M. *et al* 2000 *Nucl. Fusion* **40** 1569
[142] Challis C.D. *et al* 2001 *Plasma Phys. Control. Fusion* **43** 861
[143] Saoutic B. *et al* 2002 *Proc. 19th Int. Conf. on Fusion Energy (Lyon, 2002)* (Vienna: IAEA) CD-ROM PD/T-3 and http://www.iaea.org/programmes/ripc/physics/fec2002/html/fec2002.htm
[144] Pericoli-Ridolfini V. *et al* 2003 *Nucl. Fusion* **43** 469
[145] Start D.F.H. *et al* 1999 *Nucl. Fusion* **39** 321
[146] Phillips C.K. *et al* 1999 *Conf. on RF Power in Plasmas (Annapolis, USA, 1999)* p 69
[147] Rimini F.G. *et al* 1999 *Nucl. Fusion* **39** 1591
[148] Mantsinen M.J. *et al* 2001 *Conf. on RF Power in Plasmas (Oxnard, USA, 2001)* p 59
[149] Mantsinen M.J. *et al* 2003 *Conf. on RF Power in Plasmas (Moran, USA, 2003)* p 138
[150] Van Eester D. *et al* 2002 *Nucl. Fusion* **42** 310
[151] Mayoral M.L. *et al* 2004 *Phys. Plasmas* **11** 2607
[152] Nelson-Melby E. *et al* 2003 *Phys. Rev. Lett.* **90** 155004
[153] Mantsinen M.J. *et al* 2002 *Phys. Rev. Lett.* **89** 115004
[154] Testa D. *et al* 2000 *Nucl. Fusion* **40** 975
[155] Lee W.D. *et al* 2003 *Plasma Phys. Control. Fusion* **45** 1465
[156] Lin Y. *et al* 2003 *Plasma Phys. Control. Fusion* **45** 1013
[157] Petrov Y. *et al* 2000 *Phys. Plasmas* **7** 911
[158] Jaeger E.F. *et al* 2002 *Phys. Plasmas* **9** 1873
[159] Hedin J. *et al* 2002 *Nucl. Fusion* **42** 527
[160] Jaeger E.F. *et al* 2003 *Phys. Rev. Lett.* **90** 195001
[161] Dumont R.J. *et al* 2003 *Conf. on RF Power in Plasmas (Moran, USA, 2003)* p 439
[162] Wright J.C. *et al* 2005 *Nucl. Fusion* **45** 1411
[163] Vdovin V.L. 2004 Study of IC heating and current drive in the steady state ITER Scenario 4 *Kurchatov Institute ITER Physics Design Group Report December 2004, Plasma Physics Task to Kurchatov Institute* (ITA 19-05) N 19 TD 02 FR (for ITER JCT)
[164] Eriksson L.-G. *et al* 2004 *Phys. Rev. Lett.* **92** 235001
[165] Wukitch S.J. *et al* 2003 *Conf. on RF Power in Plasmas (Oxnard, USA, 2003)* p 4
[166] Bobkov V. *et al* 2003 *J. Nucl. Mater.* **313–316** 956
[167] Bobkov V. *et al* 2005 *J. Nucl. Mater.* **337–339** 776
[168] Lamalle P.U. *et al* 2001 *Conf. on RF Power in Plasmas (Oxnard, USA, 2001)* p 118
[169] Hartmann D.A. *et al* 2001 *Conf. on RF Power in Plasmas (Oxnard, USA, 2001)* p 130
[170] Colas L. *et al* 2001 *Conf. on RF Power in Plasmas (Oxnard, USA, 2001)* p 134
[171] D'ippolito D.A. *et al* 2001 *Conf. on RF Power in Plasmas (Oxnard, USA, 2001)* p 114
[172] D'ippolito D.A. *et al* 2002 *Nucl. Fusion* **42** 1357
[173] Parisot A. *et al* 2003 *Conf. on RF Power in Plasmas (Wyoming, USA, 2003)* p 158
[174] Vdovin V.L. *et al 28th EPS Conf. (Funchal, 2001)* P-3.74
[175] Swain D. *et al* 2004 ITER ICRF antenna loading with new limiter and plasma *Internal ITER JCT-Garching Report*
[176] Lyssoivan A. *et al* 2001 *Conf. on RF Power in Plasmas (Oxnard, USA, 2001)* p 146
[177] Lyssoivan A. *et al* 2005 *J. Nucl. Mater.* **337–339** 456
[178] Xie J.K. *et al* 2001 *J. Nucl. Mater.* **290–293** 1155
[179] Gormezano C. 2003 *20th IEEE SOFE San Diego (October, 2003)* Plenary4-2
[180] Eriksson L.-G. *et al* 2001 *Nucl. Fusion* **41** 91
[181] Stix T.H. 1975 *Nucl. Fusion* **15** 737
[182] Bonoli P.T. *et al* 2000 *Phys. Plasmas* **7** 1886
[183] Nguyen F. *et al* 2002 *29th EPS Conf. (Montreux, 2002)* P-1.045
[184] Van Eester D. *et al* 2003 *Conf. on RF Power in Plasmas (Moran, USA, 2003)* p 66
[185] Mantsinen M.J. *et al* 2004 *Nucl. Fusion* **44** 33
[186] Lin Y. *et al* 2004 *Phys. Plasmas* **11** 2466
[187] Mutoh T. *et al* 2004 Achievement of the world record in the long-pulse experiment for high-temperature plasma sustainment using the Large Helical Device uniquely developed in Japan *NIFS Press Report*
[188] Mutoh T. *et al* 2002 *NIFS-741: Proc. 19th Int. Conf. on Fusion Energy (Lyon, 2002)* (Vienna: IAEA) CD-ROM EX/P2-19 and http://www.iaea.org/programmes/ripc/physics/fec2002/html/fec2002.htm
[189] Phillips C.K. *et al* 1995 *Conf. on RF Power in Plasmas (Palm Springs, USA, 1995)* p 289
[190] Perkins F.W. 1977 *Nucl. Fusion* **17** 1197
[191] Gambier D.J. and Samain A. 1985 *Nucl. Fusion* **25** 283
[192] Vdovin V.L. *et al* 1976 *Proc. 3rd Int. Meeting on Theoretical and Experimental Aspects of Heating of Toroidal Plasma (Grenoble, 1976)* vol II, p 349
[193] Ivanov N.V. *et al* 1977 *JETP Lett.* **24** 316
[194] Hosea J. *et al* 1979 *Phys. Rev. Lett.* **43** 1802
[195] Bergeaud V. *et al* 2001 *Phys. Plasmas* **8** 139
[196] Eriksson L.-G. *et al* 1998 *Phys. Rev. Lett.* **81** 11232
[197] Johnson T. *et al* 2001 *Conf. on RF Power in Plasmas (Oxnard, USA, 2001)* p 102
[198] Tuccillo A.A. *et al* 2001 *Conf. on RF Power in Plasmas (Oxnard, USA, 2001)* p 209

[199] Hellsten T. *et al* 2003 *Conf. on RF Power in Plasmas (Moran, USA, 2003)* p 197
[200] Gates D.A. *et al* 2002 *29th EPS Conf. (Montreux, 2002)* O2.09
[201] Eriksson L.-G. *et al* 1997 *Plasma Phys. Control. Fusion* **39** 27
[202] Rice J.E. *et al* 1998 *Nucl. Fusion* **38** 75
[203] Rice J.E. *et al* 1999 *Nucl. Fusion* **39** 1175
[204] Hoang G.T. *et al* 1999 *Nucl. Fusion* **40** 913
[205] Assas S. *et al* 2003 *30th EPS Conf. (St Petersburg, 2003)* P1.138
[206] Eriksson L.-G. *et al* 2003 *Conf. on RF Power in Plasmas (Moran, USA, 2003)* p 41
[207] Noterdaeme J.-M. *et al* 2003 *Nucl. Fusion* **43** 274
[208] Rice J.E. *et al* 2004 *Phys. Plasmas* **11** 2427
[209] Rogister A.L. *et al* 2002 *Nucl. Fusion* **42** 1144
[210] Chang C.S. *et al* 1999 *Phys. Plasmas* **6** 1969
[211] Perkins F.W. *et al* 2001 *Phys. Plasmas* **8** 2181
[212] Chan V.S. *et al* 2002 *Phys. Plasmas* **9** 501
[213] Eriksson L.-G. *et al* 2002 *Nucl. Fusion* **42** 959
[214] Shaing K.C. 2001 *Phys. Rev. Lett.* **86** 640
[215] Coppi B. 2002 *Nucl. Fusion* **42** 1
[216] Craddock C.G. *et al* 1991 *Phys. Rev. Lett.* **67** 1535
[217] Leblanc B.P. *et al* 1995 *Phys. Plasmas* **2** 741
[218] Leblanc B.P. *et al* 1999 *Phys. Rev. Lett.* **82** 331
[219] Cesario R. *et al* 1999 *Conf. on RF Power in Plasmas (Annapolis, USA, 1999)* p 100
[220] Riccardi C. *et al* 1999 *Plasma Phys. Control. Fusion* **41** B209
[221] Castaldo C. *et al* 2002 *Proc. 19th Int. Conf. on Fusion Energy (Lyon, 2002)* (Vienna: IAEA) CD-ROM PD/P-01 and http://www.iaea.org/programmes/ripc/physics/fec2002/html/fec2002.htm PD/P-01
[222] Phillips C.K. *et al* 2000 *Nucl. Fusion* **40** 461
[223] Myra J.R. *et al* 2004 *Phys. Plasmas* **11** 1786
[224] MonakhoV I. *et al* 2003 *Conf. on RF Power in Plasmas (Moran, USA, 2003)* p 146
[225] Colas L. *et al* 2003 *Conf. on RF Power in Plasmas (Moran, USA, 2003)* p 190
[226] Mikhailenko V.S. *et al* 2004 *Phys. Plasmas* **11** 3691
[227] Biewer T.M. *et al* 2004 *31st EPS Conf. (London, 2004)* P2.198
[228] Schilling A. *et al* 2003 *Conf. on RF Power in Plasmas (Moran, USA, 2003)* p 166
[229] Maggiora R. *et al* 2003 *Conf. on RF Power in Plasmas (Moran, USA, 2003)* p 134
[230] Lamalle P.U. *Conf. on RF Power in Plasmas (Moran USA, 2003)* p 122
[231] Lamalle P.U. *et al* 2003 *30th EPS Conf. (St Petersburg, 2003)* P-1.193
[232] Koch R. *et al* 2001 *Conf. on RF Power in Plasmas (Oxnard, USA, 2001)* p 126
[233] Pécoul S. *et al* 2000 *27th EPS Conf. (Budapest, 2000)* p 388
[234] Green B. 2003 *Plasma Phys. Control. Fusion* **45** 687
[235] Campbell D.J. 2001 *Phys. Plasmas* **8** 2041
[236] Lister J.B. *et al* 2000 *Nucl. Fusion* **40** 1167
[237] Genacchi G. and Taroni A. 1988 JETTO: a free boundary plasma transport code (basic version) *Rapporto* ENEA RT/TIB 1988(5)
[238] Basiuk V. *et al* 2003 *Nucl. Fusion* **43** 822
[239] Pereverzev G.V. 1992 *Nucl. Fusion* **32** 1023
[240] Joffrin E. *et al* 2003 *Plasma Phys. Control. Fusion* **45** A445
[241] Equipe Tore Supra 2000 *Nucl. Fusion* **40** 1047
[242] Oikawa T. and the JT-60 team 2000 *Nucl. Fusion* **40** 1125
[243] Allen S.L. and the DIII-D team 2001 *Nucl. Fusion* **41** 1341
[244] Heesterman P. *et al* 2003 *Rev. Sci. Instrum.* **74** 1783
[245] Alves D. *et al* 2003 *4th IAEA TM on Control, Data Acquisition, and Remote Participation for Fusion Research (San Diego, 2003)*
[246] Zerbini M. *et al* 2002 *12th joint Workshop on ECE and ECH (Aix-en-Provence, 2002)*
[247] Zabeo L. *et al* 2002 *Plasma Phys. Control. Fusion* **44** 2483
[248] Ferron J.R. *et al* 1998 *Nucl. Fusion* **38** 1055
[249] Bosak K. *et al* 2003 *30th EPS Conf. (St Petersburg, 2003)* P3.164
[250] Tresset G. *et al* 2002 *Nucl. Fusion* **42** 520
[251] Pochelon A. *et al* 2003 *Conf. on RF Power in Plasmas (Moran, USA, 2003)* p 297
[252] Rice J.E. *et al* 2003 *Nucl. Fusion* **43** 781
[253] Felton R. *et al* 2000 *IEEE Trans. Nucl. Sci.* **47** 174
[254] Gribov Y. *et al* 2007 Progress in the ITER Physics Basis *Nucl. Fusion* **47** S385–S403
[255] Neyatani Y. *et al* 1997 *Fusion Eng. Des.* **36** 429
[256] Huysmans G.T.A. *et al* 1999 *Nucl. Fusion* **39** 1489
[257] Fukuda T. *et al* 2002 *Fusion Sci. Technol.* **42** 357
[258] Wijnands T. *et al* 1996 *Nucl. Fusion* **36** 1201
[259] Van Houtte D. *et al* 2004 *Nucl. Fusion* **44** L11
[260] Messiaen A.M *et al* 1996 *Nucl. Fusion* **36** 39
[261] Tamai H. *et al* 1998 *Fusion Eng. Des.* **39** 163
[262] Dumortier P. *et al* 2003 *30th EPS Conf. (St Petersburg, 2003)* P1-91
[263] Jackson G.L. *et al* 1997 *J. Nucl. Matter* **241–243** 618
[264] Mertens V. *et al* 1997 *Fusion Technol.* **32** 459
[265] 1998 *Fuzzy Logic and Intelligent Technologies for Nuclear Science and Industry (3rd Int. Workshop (Antwerp, 1998))* (Antwerp)
[266] Wijnands T. *et al* 1997 *Nucl. Fusion* **37** 777
[267] Ferron J.R. *et al* 2006 *Nucl. Fusion* **10** 46 L13
[268] Mazon D. *et al* 2002 *Plasma Phys. Control Fusion* **44** 1087
[269] Moreau D. *et al* 2003 *Nucl. Fusion* **43** 870
[270] Mazon D. *et al* 2003 *Plasma Phys. Control Fusion* **45** L47
[271] Laborde L. *et al* A model-based technique for real time control of current and pressure profiles in the JET tokamak, *Eur. J. Control.* submitted
[272] Tala T. *et al* 2004 *Proc. 20th Int. Conf. on Fusion Energy (Vilamoura, 2004)* (Vienna: IAEA) CD-ROM TH/P2-9 and http://www-naweb.iaea.org/napc/physics/fec/fec2004/datasets/index.html
[273] Mitarai O. *et al* 1997 *Nucl. Fusion* **37** 1523
[274] Jones T.T.C. *et al* 2002 *28th EPS Conf. (Funchal, 2002)* P3.073
[275] Pereverzev G. and Yushmanov P.N. 2002 *IPP–Report* IPP 5/98
[276] Zakharov L.E. and Shafranov V.D. 1986 *Reviews of Plasma Physics* vol 11 ed M. Leontovitch (Consultants Bureau: New York) p 206
[277] Zakharov L.E. *et al* 1999 *Phys. Plasmas* **6** 4693
[278] Degtyarev L. *et al* 1997 *Comput. Phys. Commun.* **103** 10
[279] Polevoi A.R. *et al* 1997 *JAERI DATA*/Code 97-014
[280] Kukushkin A.S. and Pacher H.D. 2002 *Plasma Phys. Control. Fusion* **44** 931
[281] Houlberg W.A. *et al* 1997 *Phys. Plasmas* **4** 3230
[282] Waltz R.E. *et al* 1997 *Phys. Plasmas* **4** 2482
[283] Weiland J. 1992 *Report* CTH IEFT/PP-1992-17 Chalmers University of Technology, Goteborg, Sweden
[284] Schneider M. *et al* 2005 *Plasma Phys. Control. Fusion* **47** 2087
[285] St John H.E. *et al* 1995 *Proc. 15th Int. Conf. on Plasma Physics and Controlled Nuclear Fusion Research (Seville, Spain)* (Vienna: IAEA) p 603
[286] Lister G.G. *et al* 1976 *Proc. 3rd Symp. on Plasma Heating in Toroidal Devices (Varenna, 1974)* p 303
[287] Callen J.D. *et al* 1975 *Proc. 5th Int. Conf. on Plasma Physics and Controlled Nuclear Fusion Research 1974 (Tokyo, 1974)* (Vienna: IAEA) vol I p 645
[288] Pankin A. *et al* 2004 *Comput. Phys. Commun.* **159** 157
[289] Mau T.K. *et al* 1982 *EPS Topical Conf. on RF Heating (Brussels, 1982)* p 1181
[290] Mau T.K. *et al* 1993 *Conf. on RF Power in Plasmas (Boston, USA, 1993)* p 214
[291] Kinsey J.E. *et al* 2002 *Proc. 19th Int. Conf. on Fusion Energy (Lyon, 2002)* (Vienna: IAEA) CD-ROM TH/P1-09 and http://www.iaea.org/programmes/ripc/physics/fec2002/html/fec2002.htm

[292] Crotinger J.A. *et al* 1997 LLNL Report *UCRL-ID-126284*
[293] 1998 *ITER EDA Design Description Document* WBS 4.7 (Poloidal Field Control) sections 1.3.2, 2.6 and E 3.2.1
[294] Pearlstein L.D. *et al* 2001 *28th EPS Conf. (Funchal, 2001)* P5.034
[295] Kotschenreuther M. *et al* 1995 *Phys. Plasmas* **2** 6
[296] Rebut P.H. *et al* 1991 *Phys. Fluids* B **3** 2209
[297] Jardin S.C. *et al* 1993 *Nucl. Fusion* **33** 371
[298] Goldston R.J. *et al* 1981 *J. Comput. Phys.* **43** 61
[299] Lin-Liu Y.R. *et al* 1997 *Conf. on RF Power in Plasmas (Savanna, USA, 1997)* p 195
[300] Hirshman S.P. and Sigmar D.J. 1981 *Nucl. Fusion* **21** 1079
[301] Chang C.S. and Hinton F.L. 1982 *Phys. Fluids* **25** 1493
[302] Glasser A.H. 1995 LANL Report *LA-UR-95-528*
[303] Boozer A.H. 1986 *J. Plasma Phys.* **35** 133
[304] Fukuyama A. *et al* 2004 *Proc. 20th Int. Conf. on Fusion Energy (Vilamoura, 2004)* (Vienna: IAEA) CD-ROM TH/P2-3 and http://www-naweb.iaea.org/napc/physics/fec/fec2004/datasets/index.html
[305] Fukuyama A. *et al* 1995 *Plasma Phys. Control. Fusion* **37** 611
[306] Nordman H. and Weiland J. 1989 *Nucl. Fusion* **29** 251
[307] Sauter O. *et al* 1999 *Phys. Plasmas* **4** 2834
[308] Sauter O. *et al* 2002 *Phys. Plasmas* **9** 5140
[309] Honda M. and Fukuyama A. 2004 *J. Plasma Fusion Res. Ser.* **6** 160
[310] Shirai H. *et al* 2000 *Plasma Phys. Control. Fusion* **42** 1193
[311] Bateman G. *et al* 1998 *Phys. Plasmas* **5** 1793
[312] Tani K. *et al* 1981 *J. Phys. Soc. Japan* **50** 1726
[313] Hamamatsu K. *et al* 2000 *Plasma Phys. Control. Fusion* **42** 1309
[314] Tokuda S. *et al* 1999 *Phys. Plasmas* **6** 3012
[315] Hayashi N. *et al* 2002 *J. Plasma Fusion Res. Ser.* **5** 519
[316] Budny R.V. *et al* 1992 *Nucl. Fusion* **32** 429
[317] Evrard M. *et al* 1995 *Conf. on RF Power in Plasmas, 11th Topical Conf. (Palm Springs, 1995)* p 235
[318] Brambilla M.A 1996 Full wave code for ion cyclotron waves in toroidal plasmas *Report* IPP 5/66 Max-Planck-Institut für Plasmaphysik, Garching
[319] Ignat D.W. *et al* 1994 *Nucl. Fusion* **34** 837
[320] Budny R.V. *et al* 1996 *Phys. Plasmas* **3** 4583
[321] Budny R.V. 2002 *Nucl. Fusion* **42** 1383
[322] Jardin S.C. *et al* 1983 *J. Comput. Phys.* **66** 481
[323] Casper T.A. *et al* 2003 *Plasma Phys. Control. Fusion* **45** 1
[324] Casper T.A. *et al* 2003 *30th EPS Conf. (St Petersburg, 2003)* P3.207
[325] Honda M. and Fukuyama A. 2006 *Nucl. Fusion* **46** 580
[326] Hayashi N. *et al* 2004 *J. Plasma Fusion Res.* **80** 605
[327] Hayashi N. *et al* 2005 *Nucl. Fusion* **45** 933
[328] Polevoi A.R. *et al* 2002 *Proc. 19th Int. Conf. on Fusion Energy (Lyon, 2002)* (Vienna: IAEA) CD-ROM CT.P08 and http://www.iaea.org/programmes/ripc/physics/fec2002/html/fec2002.htm
[329] Liu Y. *et al* 2004 *Nucl. Fusion* **44** 232
[330] Polevoi A.R. *et al* 2005 *Nucl. Fusion* **45** 1451
[331] Ward D.J. *et al* 1993 *Nucl. Fusion* **33** 821
[332] Connor J.W. *et al* 2004 *Nucl. Fusion* **44** R1
[333] Lao L.L. *et al* 2003 *Nucl. Fusion* **43** 1023
[334] Murakami M. *et al* 2005 *Nucl. Fusion* **45** 1419
[335] Houlberg W.A. *et al* 2005 *Nucl. Fusion* **45** 1309
[336] Snyder P.B. *et al* 2004 *Nucl. Fusion* **44** 320
[337] Hayashi N. *et al* 2004 *Nucl. Fusion* **44** 477
[338] Kessel C.E., Budny R.V. and Indireshkumar K. 2005 Simulation and analysis of the hybrid operating mode in ITER *21st IEEE/NPSS Symp. on Fusion Energy (Knoxville, TN, USA, September, 2005)* IEEE catalog No. 05CH37764C
[339] Scott S.D. *et al* 1988 *Proc. 12th Int. Conf. on Plasma Physicsand Controlled Nuclear Fusion Research (Nice, 1988)* (Vienna: IAEA, 1989) vol 1, p 655
[340] Challis C.D. *et al* 1989 *Nucl. Fusion* **29** 563
[341] Prater R. *et al* 1993 *Plasma Phys. Control. Fusion* **35** A53
[342] Tala T. *et al* 2000 *Nucl. Fusion* **40** 1635
[343] Lang P.T. *et al* 2005 *Nucl. Fusion* **45** 502